The Application of Fluorescence Lifetime Imaging Microscopy to Quantitatively Map Mixing and Temperature in Microfluidic Systems

Emmelyn M. Graham

Degree of Doctor of Philosophy

The University of Edinburgh

2007

Abstract

The technique of Fluorescence Lifetime Imaging Microscopy (FLIM) has been employed to quantitatively and spatially map the fluid composition and temperature within microfluidic systems.

A molecular probe with a solvent-sensitive fluorescence lifetime has been exploited to investigate and map the diffusional mixing of fluid streams under laminar flow conditions within a microfluidic device. Using FLIM, the fluid composition is mapped with high quantification and spatial resolution to assess the extent of mixing. This technique was extended to quantitatively evaluate the mixing efficiency of a range of commercial microfluidic mixers employing various mixing strategies, including the use of obstacles fabricated within the channels.

A fluorescently labelled polymer has been investigated as a new probe for mapping temperature within microfluidic devices using FLIM. Time Correlated Single Photon Counting (TCSPC) measurements showed that the average fluorescence lifetime displayed by an aqueous solution of the polymer depended strongly on temperature, increasing from 3 ns to 13.5 ns between 23 and 38 ^{o}C. This effect was exploited using FLIM to provide high spatial resolution temperature mapping with sub-degree temperature resolution within microfluidic devices.

A temperature-sensitive, water-soluble derivative of the rhodamine B fluorophore, effective over a wide dynamic temperature range (25 to 91 ^{o}C) has been used to map the temperature distribution during the mixing of fluid streams of different temperatures within a microchannel. In addition, this probe was employed to quantify the fluid temperature in a prototype microfluidic system for DNA amplification.

FLIM has been demonstrated to provide a superior approach to the imaging within microfluidic systems over other commonly used techniques, such as fluorescence intensity and colourimetric imaging.

Declaration

I declare that the work presented in this thesis is my own unless stated by reference.

Signed:

Date:

Acknowledgements

Firstly, I would like to thank my Supervisor, Anita Jones. I could not have imagined having a better advisor and mentor for my PhD, and without her common-sense, knowledge, perceptiveness and encouragement I would never have completed the PhD.

Indeed after all the many years spent at Edinburgh, I've got quite a list of people who contributed in some way to this thesis, for which I would like to express a big THANKS. I am forever indebted to all those who helped me, with great patience, in COSMIC, that goes to Steven, Millington, Rob and Trish who were my COSMIC ‘A-Team’ for their many reconnaissance missions when things veered off track. Steven you were a superstar for all the FLIM help and everything else too.

Thanks go to the ladies, Dilek, Gaynor and Trish, who made it all so much more fun at work and beyond. Dave Towers for the PhD opportunity and PIV assistance. David Mendels for solving the modelling, to my relief. To all my colleagues for providing a stimulating and fun environment in which to learn and grow.

I cannot end without thanking my friends, on whose constant encouragement and support I have relied on throughout my time at university, through all the difficult times, and for all the emotional support. Julie for her humor, friendship and chats. Thanks to Fee who was so supportive and always there for me with encouragement to get me through. Cheers to Rachel for our common despairs, rants and endurance. Alice who was so supportive and helpful at the beginning of it all. To my brother Robert, for his support over the years. Lorna for being a wonderful flatmate and inspiration. People at work who put up with me over the last few months. Overall, its been quite a journey not just for the PhD, to those who helped me find a path through, Sandra and Menelas.

“It is not the position in which you stand,
but the direction in which you look.”

Table of Contents

Chapter 1

Introduction

Microfluidics has promised to revolutionise chemical analysis,[1;2] synthesis[3-5] and biotechnology,[6] by combining processes such as mixing, separation, reaction and detection in a single device. These systems function as "labs-on-a-chip"[7], otherwise know as micro total analysis systems (μ-TAS), creating a technology that can be low-cost, high-throughput, miniaturised, and automated. Over the past decade the number and range of microfluidic applications has exponentially grown and this is now an accepted technology, used both in newly developing areas of lab-on-a-chip analytical devices and the more established inkjet printing applications.[8] The steady uptake of microreactor technologies both within commercial and academic environments is exploiting the benefits of miniaturisation offered by flow chemistry over traditional batch methodologies. Microfluidics is now a global business due to benefits offered by miniaturisation and commercial uptake is expected to further increase.[9]

There are many advantages in reducing the size of diagnostic devices to the micrometer or even nanometer range, but in scaling down devices there are issues concerning transport processes, fluid mixing and temperature measurement, all of which are fundamental to control processes at the microscale.[10] Irrespective of which techniques are employed to create flow through microfluidic devices, it is crucial to obtain flow conditions which allow reagents to mix in a controlled and managed process, in which the temperature and composition variations with time are known and controlled as precisely as possible.[11;12] It is essential, therefore, that techniques capable of visualizing fluid composition and temperature with high quantification and spatial resolution are found. This will allow testing of prototype devices, and will provide essential experimental data to guide the development of theoretical and experimental models and validate computational simulations. Computational fluid dynamics models have proved useful in preliminary microfluidic designs, but a rigorous understanding of the fundamental principles of microfluidics would lead to the development of better models for complex microfluidic devices.[13]

Within this thesis a superior approach to the imaging of microfluidic systems using Fluorescence Lifetime Imaging Microscopy (FLIM) is described. Chapter 4 describes a system employed to quantitatively and spatially map fluid mixing within microfluidic systems. As an extension, the technique has been exploited to evaluate the mixing efficiency of various commercial microfluidic mixers in Chapter 5.

In addition to mixing, temperature measurements within microfluidic systems are essential for numerous applications, including controlling many chemical and biological interactions. Chapter 6 presents a novel polymer probe for high resolution temperature mapping offering sub-degree resolution. In addition, results are presented using a molecular probe with a temperature sensitivity extended over a wide, practical temperature range from room temperature to over 90 ^{o}C. This has been used to image the temperature distribution during mixing of fluids of different temperatures and for static fluid temperature measurements within devices designed to perform temperature-sensitive DNA amplification.

Chapter 2

Background Theory

The work presented in this thesis makes use of a number of theoretical principles. The main technique used throughout this study is time-resolved fluorescence spectroscopy which forms the basis of Fluorescence Lifetime Imaging Microscopy (FLIM). The fundamental photophysical theory which underpins the research presented in subsequent chapters will be outlined here to provide the understanding necessary to appreciate the results and their implications. A brief theoretical description of pressure-driven microfluidic flows will also be given, that will enable the reader to understand the essential features of the microfluidic systems studied.

2.1 *Absorption of light*

Molecules have discrete energy levels, which depend on the rotational, vibrational and electronic structure of the specific molecule. The ability of a molecule to absorb and emit radiation is dependent on these characteristic energy levels. The absorption by a molecule of a photon of light, with energy E, equal to the difference between energy states, can promote the transition of an electron from the ground electronic state to a vibrationally and electronically excited state. This is illustrated in Figure 2.1.

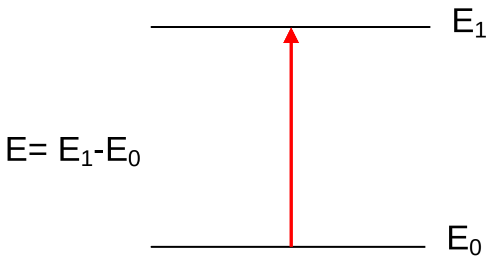

Figure 2.1: Absorption of radiation with energy E, resulting in an electronic transition of an electron from the ground state with energy E_0 to an excited state with energy E_1.

Electrons are described within a particular electronic state by their spin quantum number (m_s), with values m_s = +½ or -½. This can also be expressed by their orientation as spin-down or spin-up orientations, as depicted in Figure 2.2, with the direction of the arrows representing the values of +½ or -½. For a specified electronic state the total spin quantum number (S) is given by the vector addition of the individual spin quantum numbers. The spin multiplicity of an electronic state is defined as *2S+1*.

If a molecule has 2 electrons in its highest occupied molecular orbital, in the ground state these have opposing spins of +½ or -½., hence *S=0* and the multiplicity (2S+1) of this state is one. This is referred to as a singlet state (Figure 2.2a). In an excited state, the electrons will either remain opposing (Figure 2.2b) with *S=0* or can adopt parallel spins (Figure 2.2c) with *S=1* and a multiplicity of three, which is known as a triplet state. It should be noted that triplet states are not populated by absorption but by intersystem crossing from an excited singlet state, as explained in subsequent paragraphs.

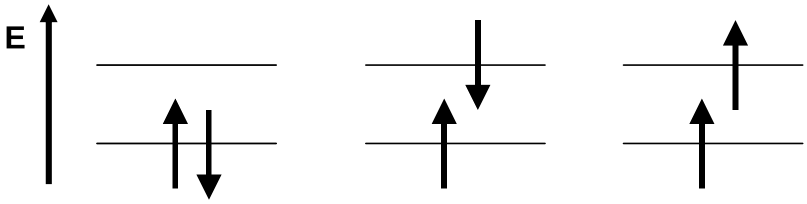

(a) Singlet ground state
S=0
Multiplicity (2S+1) =1

(b) Singlet excited state
S=0
Multiplicity (2S+1) =1

(c) Triplet excited state
S=1
Multiplicity (2S+1) =3

Figure 2.2: Pictorial representation of singlet and triplet states. The direction of the arrows represents the orientation for each electron as described by its spin quantum number (m_s) with values of +½ or -½.

2.2 Photoluminescence

Certain substances can emit light when they are excited by photons in the visible, near ultraviolet and x-ray region of the spectrum. This phenomenon is called photoluminescence and can be divided into two categories, namely fluorescence and phosphorescence. Fluorescence and phosphorescence transitions differ in terms of the accompanying change in spin state. The electronic transitions responsible for fluorescence do not involve a change in spin state. As a consequence, fluorescence is short-lived with luminescence ceasing within nanoseconds of excitation. In contrast, a change in electron spin (a formally forbidden process) accompanies phosphorescence emissions, which causes the radiation for a bulk sample to endure for a much longer time after termination of irradiation (milliseconds to seconds).

2.3 De-excitation

Any molecule in an excited state will return to the ground state, emitting the absorbed energy *via* a number of processes. The main mechanisms by which de-excitation can occur can be categorised into non-radiative and radiative decay processes.[14] These processes are illustrated schematically using a Jablonski diagram (Figure 2.3), which illustrates the energy levels for a typical photoluminescent molecule. If a molecule initially occupies the lowest vibrational energy level of its electronic ground state in a singlet state labelled S_o and then absorbs a photon of the correct energy, it can be excited to one of several vibrational energy levels in the first excited state, S_1, or to higher electronically excited singlet states (e.g. S_2). Relaxation to the ground state can occur by a number of mechanisms that are either radiationless in that no photons are emitted or involve the emission of a photon. In Figure 2.3, the straight vertical arrows represent fluorescence and phosphorescence, which involve the release of a photon of energy. The other deactivation steps as indicated by “wavy” arrows represent the radiationless processes, which compete with fluorescence. If deactivation by fluorescence is rapid with respect to the radiationless processes, then such emission will have a high probability and intense fluorescence will be observed.

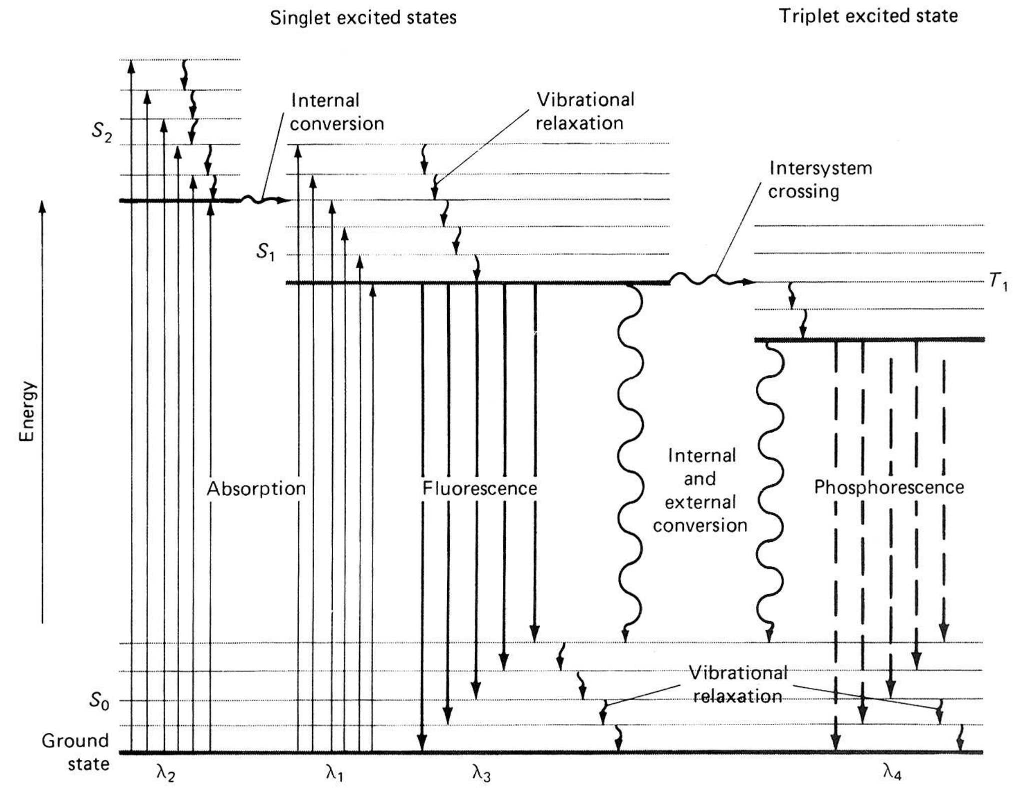

Figure 2.3: A Jablonski diagram or partial energy level diagram for a photoluminescent system showing pathways for the deactivation of an excited state.[15] The lowest vibrational energy level for each electronic state is indicated by the thicker line.

2.3.1 Non-radiative decay

2.3.1.1 Vibrational relaxation

Vibrational relaxation (VR) is a form of radiationless de-excitation in which a molecule in an excited vibrational energy level losses energy as it moves to a lower vibrational energy level in the same electronic state. Vibrational relaxation occurs by transferring the energy from the excited molecule to its surroundings, for example, to neighbouring solvent molecules. This relaxation method is extremely efficient and hence rapid, so that the average lifetime in an excited vibrational energy level is of the order of picoseconds or less. This period is significantly shorter than the average lifetime in an electronically excited state. As a result, molecules which are excited to different vibrational energy levels of the same excited electronic state quickly return to the lowest vibrational energy level of this excited state. Hence, for most solvated molecules, fluorescence only occurs from the lowest vibrational energy level of an excited state, i.e. from the levels which are thermally populated according to the Boltzmann distribution. This is normally true for fluorophores in a condensed phase (close proximity of solvent or coordinating molecules to the fluorophore) and is more commonly known as Kasha's rule. This states that fluorescence emission of a fluorophore is independent of the excitation wavelength provided it is in a condensed phase.

Figure 2.4 is helpful in explaining the significance of excitation and emission spectra to probe both the vibrational structure of the excited and ground states. Excitation spectra can show the variation in the emission intensity as a function of excitation wavelength and therefore contain information on the vibrational structure of the excited state, whereas emission spectra, which are obtained by monitoring the fluorescence emission intensity as a function of the emission wavelength, can provide information on the ground state vibrational levels.

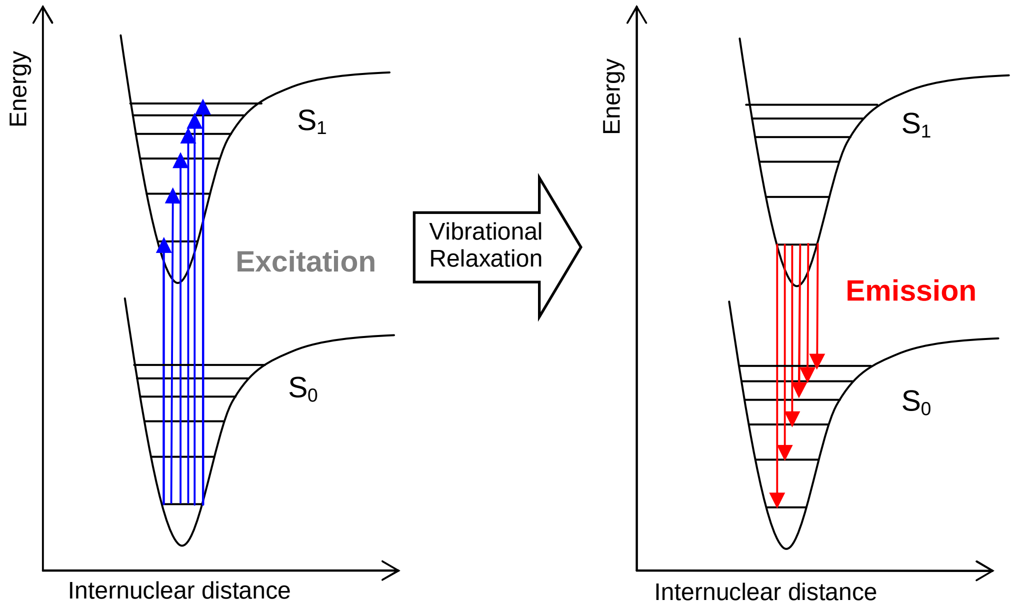

Figure 2.4: Schematic representation of transitions that occur during the excitation and emission events of a fluorophore. This also illustrates the consequence of the high efficiency of vibrational relaxation, resulting in emission from the ground vibronic level of the excited state.

2.3.1.2 Internal conversion and Intersystem crossing

Internal conversion (IC) is another form of radiationless relaxation in which a molecule in the ground vibrational level of an excited electronic state passes directly into a high vibrational energy level of a lower energy electronic state of the same spin multiplicity (Figure 2.5a). By a combination of internal conversion and vibrational relaxation, a molecule in an excited electronic state may return to the ground electronic state without emitting a photon.

Intersystem crossing (ISC) is a third form of radiationless relaxation in which a molecule in the ground vibrational energy level of an excited electronic state can pass into a high vibrational energy level of a lower energy electronic state with a different spin multiplicity (Figure 2.5b).

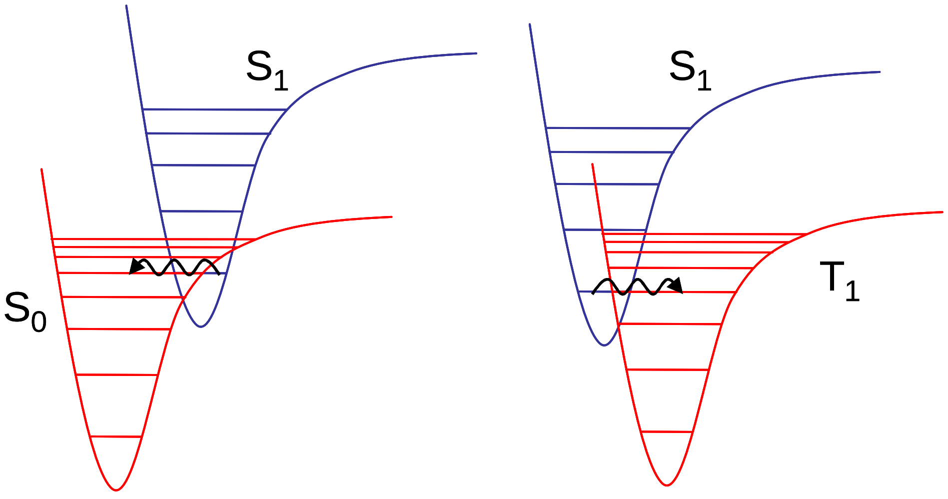

(a) Internal conversion **(b) Intersystem crossing**

Figure 2.5: Schematic representation of internal conversion **(a)** and intersystem crossing **(b)** between isoenergetic vibrational levels.

External conversion is a related form of radiationless relaxation in which excess energy can be transferred to a solvent molecule or another component in the sample matrix.

2.3.2 Radiative Decay

The relaxation of an electronically excited molecule by the emission of a photon of radiation is referred to as radiative decay. Radiative decay can occur by two processes namely fluorescence and phosphorescence. These processes are determined solely by the multiplicities of the states between which the transition occurs. Phosphorescence occurs between states of different multiplicities, for example, by emission of a photon of light relaxation from an excited triplet state to a singlet ground state (dashed vertical lines in Figure 2.3). Phosphorescence occurs when a molecule in the lowest vibrational energy level of an excited triplet electronic state relaxes to the ground state, following an intersystem crossing from an excited singlet state to a triple excited state (Figure 2.5b). Whereas fluorescence is a radiative transition between electronic states of the same spin multiplicity, for example, by emission of a photon of light to relaxation from an excited single state to a singlet ground state (solid vertical lines in Figure 2.3). Fluorescence decays rapidly after the excitation source is removed with the average lifetime of the molecule in the excited state typically picoseconds to nanoseconds. In comparison, phosphorescence may continue to emit light for some time after removing the excitation source, as the average lifetime is significantly longer, in the region of millisecond to seconds. This is due to the spin-forbidden nature of the transition between states of different multiplicities.

2.3.2.1 Fluorescence

Fluorescence occurs when a molecule in the lowest vibrational energy level of an excited electronic state returns to a lower energy electronic state by emitting a photon. Since molecules usually return to their ground state by the fastest mechanism, fluorescence is only observed if it is a more efficient means of relaxation than the combination of internal conversion and vibrational relaxation. These non-radiative processes compete with those that lead to radiative decay.

Fluorescence may return the molecule to any of the vibrational energy levels in the ground electronic state. Hence fluorescence occurs over a range of wavelengths. The change in energy for the fluorescence transition is generally less than that for absorption, the resulting fluorescence spectrum being shifted to a longer wavelength than its absorption spectrum (Figure 2.6). This is a consequence of the efficiency of vibrational relaxation to the lowest vibrational level in an excited state, and is called the Stokes shift. The Stokes shift is defined as the difference between the maximum of the first absorption band and the maximum of the fluorescence spectrum (Figure 2.6).

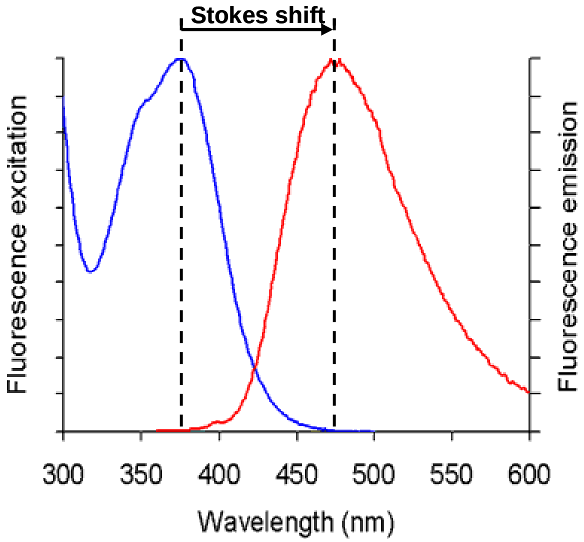

Figure 2.6: Diagram illustrating the Stokes shift observed between the excitation (blue spectra) and emission (red spectra) spectra.

2.4 *Fluorescence decay kinetics*

Excited state decay obeys a first order kinetics process, hence an excited fluorophore population, [M*], decays according to

$$-\frac{d[M^*]}{dt} = k_F[M^*] \qquad \text{Equation 2.1}$$

where the rate constant, k_F, is the sum of the rate constants for all the radiative and non-radiative decay processes ($k_F = k_R + \Sigma k_{NR}$), therefore $k_F = k_R + k_{IC} + k_{ISC} + k_{VR} + k_{quenching}$ +….. etc.[14;16] Following integration of Equation 2.1, an expression for the concentration of the excited state as a function of time is provided as

$$[M^*](t) = [M^*]_0 \exp(-k_F t) \qquad \text{Equation 2.2}$$

where $[M^*]_o$ is the initial concentration of M^* at t=0. The parameter monitored during fluorescence lifetime experiments is the fluorescence intensity, I, which is the rate of the emission of photons and is related to the excited state concentration by

$$I_F(t) = k_R [M^*](t) \qquad \text{Equation 2.3}$$

Substituting for $[M^*]$ from Equation 2.2 gives

$$I_F(t) = k_R [M^*]_0 \exp(-k_F t) \qquad \text{Equation 2.4}$$

Substituting for $[M^*]_0$ from $I_F(0)=k_R[M^*]_0$, where $I_F(0)$ is the intensity at the time of the initial excitation pulse, into Equation 2.4 gives

$$I_F(t) = I_F(0) \exp(-k_F t) \qquad \text{Equation 2.5}$$

Therefore the intensity decays exponentially after the initial excitation pulse. The fluorescence lifetime of the excited state, τ_F, can be represented as $\tau_F = (1/k_F)$. The fluorescence lifetime of a molecule is defined as the time taken for the excited state population to fall to 1/e of that initially excited. Equation 2.5 can then be rewritten as

$$I_F(t) = I_F(0) e^{\frac{-t}{\tau_f}} \qquad \text{Equation 2.6}$$

Equation 2.6 relates the measured parameter of intensity to the fluorescence lifetime and enables its calculation experimentally. Two methods have been employed in this thesis to determine the fluorescence lifetime, the first is Time Correlated Single Photon Counting (TCSPC) spectroscopy techniques and the second is Fluorescence Lifetime Imaging Microscopy (FLIM), which spatially resolves the fluorescence lifetime of a sample. These will be discussed in more detail in later sections.

2.5 Fluorescence quantum yield

The efficiency of fluorescence can be expressed by the fluorescence quantum yield, Φ_F, which is the fraction of excited molecules returning to the ground state by fluorescence (Equation 2.7).

$$\Phi_F = \frac{\text{number of photons emitted}}{\text{number of photons absorbed}}$$ Equation 2.7

The quantum yield can range from 1, when every molecule in an excited state undergoes fluorescence, to 0 when fluorescence does not occur. The fluorescence quantum yield, Φ_F, can be related to the fluorescence lifetime by

$$\Phi_F = \frac{k_R}{k_F} = k_R \tau_F$$ Equation 2.8

Therefore the fluorescence lifetime, τ_F, is a measure of the fluorescence quantum yield, Φ_F. The rate constant for the radiative decay processes, k_R, is essentially constant for a particular fluorophore as it is a consequence of the intrinsic electronic properties of the molecule. Therefore the fluorescence lifetime is sensitive to changes in the non-radiative decay pathways. A subsequent increase in non-radiative decay rates will reduce the fluorescence lifetime. These effects make the fluorescence lifetime extremely sensitive to the molecular environment surrounding the fluorophore. Indeed, it is this aspect which has been exploited within this thesis to probe microenvironmental changes such as solvent composition and fluid temperature to investigate and spatially map fluid mixing and temperature within microfluidic devices. Fluorescence techniques can be used to investigate numerous other parameters that affect the microenvironment surrounding a molecule, including viscosity, temperature, polarity, presence of quenchers, pH and pressure.[17]

2.6 Steady-state and time-resolved fluorescence

Generally fluorescence measurements are categorised into either steady-state or time-resolved measurements. Steady-state measurements are most commonly performed due to their simplicity and the use of inexpensive equipment, unlike that necessary for more complex time-resolved measurements. Steady-state measurements are performed through the continuous excitation of a sample, followed by recording an excitation or emission spectrum. Therefore, they represent an average of the time-resolved phenomena. The sample attains a steady state virtually instantaneously due to the nanosecond time scale of fluorescence. The fluorescence intensity decay of a sample, following a short pulse of excitation light, is measured using time-resolved techniques, typically performed on the nanosecond timescale.

2.7 Advantages of time-resolved measurements

The intensity of the fluorescence, I_F, is proportional to the amount of the radiation from the excitation source that is absorbed and the quantum yield for fluorescence. The intensity of fluorescence increases with an increase in quantum efficiency, incident power of the excitation source and concentration of the fluorescing species. However, as the fluorescence lifetime is an intrinsic property of the excited state of the fluorophore, the fluorescence lifetime is independent of the concentration of the fluorescing species and the incident power of the excitation source.[18] Therefore, the fluorescence lifetime is insensitive to fluctuations or variations in the excitation source and the optical path or optical aberrations. The use of fluorescence intensity to provide spatial quantification of samples is severely hampered by effects such as radiation scattering, optical aberrations, inhomogeneous excitation, photon path-length, collection efficiency and autofluorescence.[19] Therefore, fluorescence lifetime measurements can be a powerful means to provide quantification of samples due to inherent insensitivity to instrumental variations, photobleaching, autofluorescence and scattered light. Photobleaching, more commonly known as fading, is the photo-induced irreversible loss of a fluorophore's ability to exhibit fluorescence.

2.8 Fluorescence quenching

Fluorescence quenching is observed by a reduction in the fluorescence lifetime (or quantum yield) and is caused by an enhancement of the non-radiative pathways. Collisional quenching due to the presence of heavy atoms, for example bromide (Br^-) and iodide (I^-), is commonly observed as the ions increase the probability of intersystem crossings. This interaction is referred to as the external or internal heavy atom effect, depending if the atom is a substituent of the fluorophore (internal or intramolecular interaction) or an independent species (external or intermolecular interaction). Triplet emission following an intersystem crossing is extremely slow, hence the emission is usually quenched by other processes. Collisional quenching is described by the Stern-Volmer equation, given by

$$\frac{F_0}{F} = 1 + k_q \tau_0 [Q] \qquad \text{Equation 2.9}$$

where F_0 and F are the fluorescence intensities in the absence and presence of a quencher, respectively, k_q is the quenching constant, τ_0, is the lifetime of the fluorophore in the absence of the quencher and [Q] is the concentration of the quencher. Molecular oxygen is regarded as one of the best known collisional quenchers, which is considered to quench virtually all known fluorophores.[14;17]

2.9 Optical microscopy

Epifluorescence and confocal microscopy techniques have been employed within this thesis to produce images of fluids within microfluidic devices. Hence the theory behind the techniques is briefly explained to allow an appreciation of the results.

2.9.1 Epifluorescence microscope

Epifluorescence microscopy relies upon episcopic (reflected) illumination of the sample under investigation. In contrast, diascopic illumination depends on transmitted illumination. Figure 2.7 illustrates the mode of operation of an epifluorescence microscope. The incident excitation light and the detected fluorescence emission, both pass through the objective lens. The excitation beam is reflected by a dichroic mirror (beam splitter) into the objective. The dichroic mirror has a wavelength-dependent reflectivity, for example, a 430 nm dichroic filter reflects wavelengths shorter than 430 nm and transmits wavelengths longer than 430 nm. Hence it effectively separates the excitation light from the emitted fluorescence. Following excitation of the sample, the resulting fluorescence emitted is collected through the objective and transmitted through the dichroic mirror to the detector. Residual transmitted excitation light is excluded by a ‘barrier’ filter in front of the detector. This absorbs the excitation light and transmits the fluorescence. In addition, the filter can be selected to permit the desired wavelength range of the fluorescence emission transmitted to the detector. An excitation filter can also be used, however, this was not necessary in this study due to the use of laser excitation with a narrow bandwidth. The epifluorescence microscope allows the illumination or excitation of the full field of view of the objective and the detection of fluorescence from the full field of view.

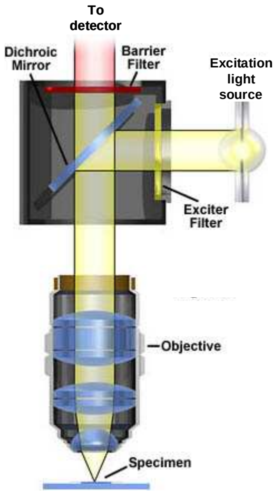

Figure 2.7: Diagram illustrating the mode of operation of a standard epifluorescence microscope. *Annotated image from Microscopy lecture course, University of Edinburgh.*

Using an epifluorescence microscope will expose the entire specimen within the field of view to excitation light. This results in the excitation of fluorescence throughout the depth of the sample. Therefore fluorescence will be collected from throughout the entire sample. The fluorescence collected from above and below the focal plane of the objective is superimposed into one image, which results in blurring of the image. However, this can be overcome with confocal fluorescence microscopy techniques described in the next section. The depth of field of an epifluorescence microscope is within the range of 2-3 µm.[17]

2.9.2 Confocal fluorescence microscopy

Confocal fluorescence microscopy exploits an effective but simple solution to remove the out-of-focus fluorescence, which blurs the information detected from the focal plane. The technique relies on the excitation of the specimen by a focused laser beam, in which the excitation intensity rapidly decreases with distance from the focal plane. Hence only confocal fluorescence is detected from the excitation plane and any fluorescence stimulated from above or below the plane of focus is rejected.

2.9.2.1 Confocal Laser Scanning Microscopy (CLSM)

Figure 2.8 illustrates the procedure and operation employed by a confocal laser scanning microscope. A focused laser spot is scanned across a sample in raster fashion to excite fluorescence. Confocal pinholes eliminate out-of-focus fluorescence from the photomultiplier tube detector. A fluorescence image is acquired point-by-point as the laser beam is scanned across the sample. Confocal techniques allow the optical sectioning of a sample to reconstruct a three dimensional representation of a sample.

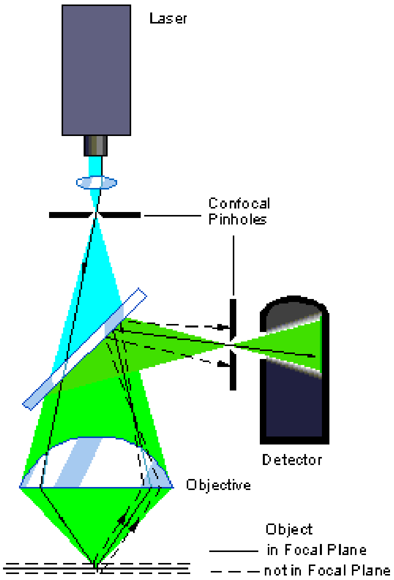

Figure 2.8: Diagram illustrating the operation and acquisition of confocal images to allow optical sectioning of samples and hence the construction of three dimensional images. *Image from Microscopy lecture course, University of Edinburgh.*

2.10 Microfluidics

The global strive towards the miniaturisation of a huge variety of systems down to micron scales was naturally extended to fluid systems. Although microfluidics appears has experienced enormous exploitation from the 1990s, it was actually developed in the 1960s as an analogous system to miniaturised electronic circuits, with the fluid flow analogous to the flux of electrons.[20] The fabrication techniques developed to produce microelectro-mechanical systems (MEMS) was exploited to fabricate microchannels and hence resulted in the increase in microfluidic technologies in the 1990s.

Microfluidics can be described in crude terms as miniaturised plumbing. It involves the handling and transport of minute volumes of fluids by gravity, pressure and electrokinetics through various machined manifolds with at least one dimension less than 1 mm. [1 nL = $(100\ \mu m)^3$]

Ink-jet printing technology is perhaps the most commonly known example of microfluidics. Figure 2.9 provides a perception of the dimensions and scale characteristics of a selection of typical microfluidic devices compared to other common objects.

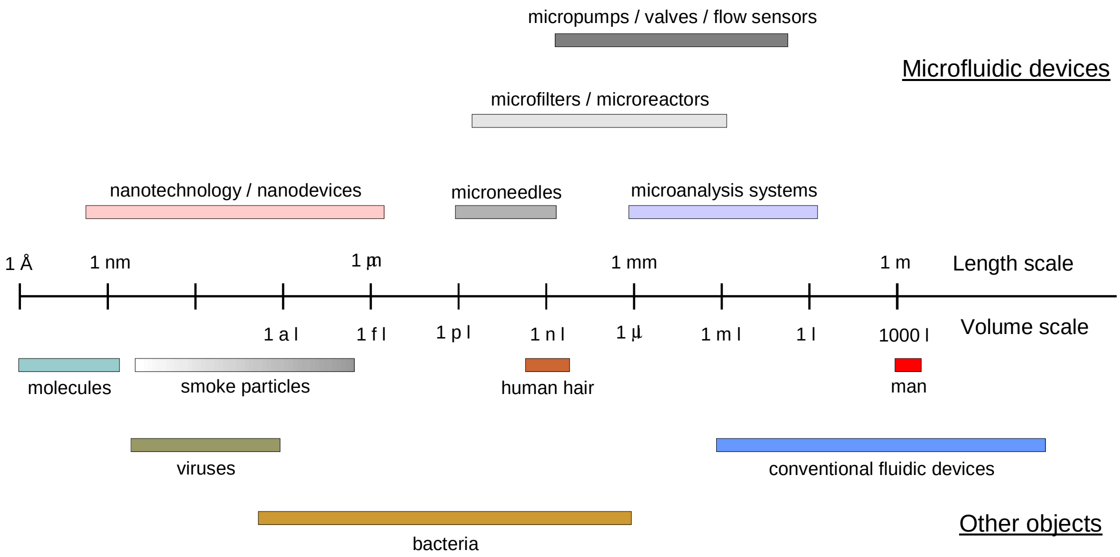

Figure 2.9: Size characteristics of microfluidic devices in comparison with common objects.[21]

Microfluidics is considered to differ from microelectronics as the fundamental physics of fluids actually changes when scaling from the macroscale to the microscale, unlike electronics.[20] Microfluidic systems are dominated by surface effects due to the large surface to volume ratio. Hence the necessity and strive to develop quantitative tools to explore and understand fluid interactions and phenomena at the microscale.

2.10.1 Hydrodynamics of pressure-driven flow

The fluid flow in microchannels is most often characterised using the Reynolds number (Re), which is defined by

$$\mathrm{Re} = \frac{\rho u l}{\eta} \qquad \text{Equation 2.10}$$

Where ρ is the fluid density, u is the mean velocity, η is the dynamic viscosity and l is the most relevant length scale. l is normally taken as the diameter of a channel, however, in the case of non-circular channels the hydrodynamic diameter, d_h, is used. This is defined by

$$d_h = \frac{4A}{P} \qquad \text{Equation 2.11}$$

where A is the cross-sectional area and P is the wetted perimeter of the cross-section. The Reynold's number is equivalent to the ratio of the inertial forces ($\rho.u$) to viscous forces (η/l) and is used to quantify the relative proportions of these important forces for any given flow conditions. It is therefore employed to define different flow regimes, for example, laminar and turbulent flows. For a straight circular pipe, the transition from laminar to turbulent flow occurs between Re of 2000 and 3000.[22] Microfluidic flows have low Re of typically less than 100, which can be viewed as equivalent to an increase in the apparent viscous (or friction) forces.[23;24] Microscopic flows are universally laminar, hence the flow is completely devoid of turbulence such that packets of fluid follow smooth streamlines. Therefore the mixing of material between fluid streams is purely by molecular diffusion. Molecular diffusion can act as an efficient and rapid mixing mechanism at extremely small dimensions.[12] However, even on the scale of many microchannels this mixing is relatively slow in comparison with the convection of the material through the channel. This effect is characterised by a large Péclet number, Pe, defined by

$$Pe = \frac{ul}{D} \qquad \text{Equation 2.12}$$

where D is the diffusion coefficient. Diffusive mixing can be considered as the random motion of a molecular species within a system to progress towards uniform conditions. For example, the diffusion of molecules causes a net movement of molecules from areas of higher concentration to areas of lower concentration until equilibrium is reached giving a homogenous solution. The phenomenon of the random translational motion of particles suspended in a fluid due to molecular collisions is referred to as Brownian motion. Brownian motion leads to the diffusion of particles in accordance with Fick's law, expressed as

$$J = -D\frac{dc}{dx} \qquad \text{Equation 2.13}$$

where c is the concentration, J is the flux and D is the diffusion coefficient. The displacement of a particle can be related to the diffusion coefficient by Einstein's equation of Brownian motion,[25] which states that

$$x = (2Dt)^{1/2} \qquad \text{Equation 2.14}$$

where x is the root-mean-square distance traversed by a molecule during the time interval t for a given diffusion coefficient. The diffusion coefficient, D, can be obtained from the Stokes-Einstein equation defined as

$$D = \frac{k_B T}{6\pi\eta r} \qquad \text{Equation 2.15}$$

where k_B is the Boltzmann's constant, T is the absolute temperature and r is the radius of spherical particles.

Pressure-driven flow is one of the most common methods to generate fluid transport through microchannels and is relatively easy to implement and is reproducible using positive displacement pumps, such as syringe pumps. One of the fundamental laws of fluid mechanics for macroscale pressure-driven laminar flow, is the no-slip boundary condition, which states that the fluid velocity matches the velocity of the solid boundary, i.e. the fluid velocity at the walls must be zero. This is generally accepted at the macroscopic level, but recently research has suggested that this condition is not always applicable at the micro- and nano-scale.[20;26;27]

Due to the no-slip condition, pressure driven flows in microchannels develop a parabolic velocity flow distribution, commonly referred to as Poiseuille flow. This results in a much higher velocity in the centre of the channel, with the layers of liquid close to the walls assumed to have zero velocity if the no-slip boundary condition holds true. Figure 2.10 illustrates the parabolic flow profile generated in a circular microchannel resulting from a pressure-driven flow.

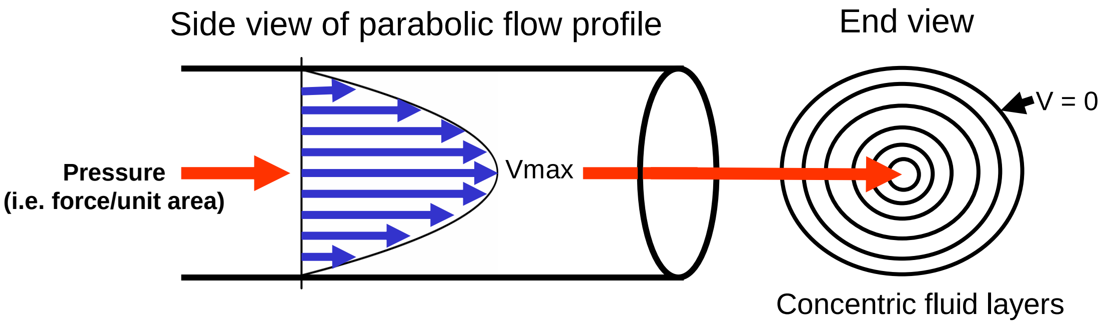

Figure 2.10: Diagram illustrating the parabolic velocity flow profile developed in a circular microchannel from a pressure-driven flow. V is the fluid velocity, where *Vmax* and *V = 0* represent the maximum and zero fluid velocity, respectfully.

The flow profile developed in a rectangular-shaped channel creates a more complex distribution of fluid velocities with different parabolic velocity gradients across one or both cross-sectional dimensions. Figure 2.11 displays a computer simulated flow profile generated through a rectangular-shaped microchannel.

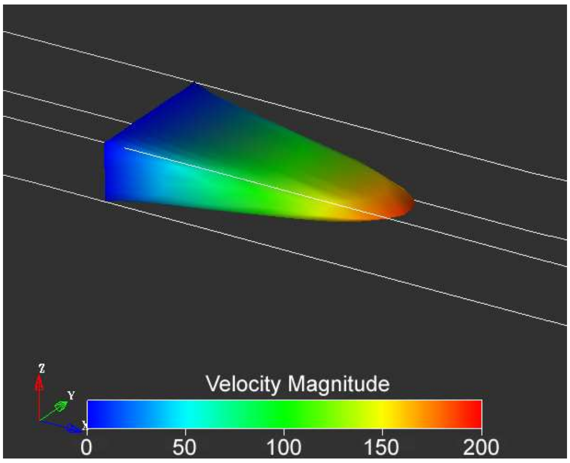

Figure 2.11: The velocity profile for a microchannel with aspect ratio 2:5 under conditions of pressure driven flow. The image was produced from computational fluid dynamics (CFD) simulation of the flow. *Image from Prof Paul Yager's website, University of Washington.*

This flow distribution results in all molecules in the channel experiencing a position-dependent distribution in residence time.[28] Hence, this allows fluids close to the wall increased time to diffuse, observed by the 'butterfly effect' where the mixing interface between two parallel fluid streams is significantly broadened at the top and bottom walls, i.e. the interface appears)(-shaped rather than I-shaped. Whereas, fluids positioned at the centre of the channel have a higher velocity, therefore effectively have significantly less time to diffuse and mix. The Péclet number is therefore useful to relate the convection of flow to that of the molecular diffusion.

Typically microchannels have characteristically large pressure drops to force fluids to flow through the channels. The pressure drop in a circular microchannel is given by

$$\Delta p = \frac{128\eta l Q}{\pi d_h^4} \qquad \text{Equation 2.16}$$

where Q is the volumetric flow rate. Microfabrication techniques typically produce microchannels with non-circular cross-sections, however, circular microchannels are generally useful as a point of reference. Circular channels can be produced from sealing two semi-circular cross-sectional channels. In non-circular microchannels the resistance to flow will be different to that of circular channels and can be accounted for with regard to pressure drop using a different friction factor related to the shape of the channel.[29] It should be noted that for laminar flow in macroscale channels the friction factor is independent of the wall roughness.[29]

Chapter 3

Experimental

The two main diagnostic techniques employed within this thesis to investigate fluid composition and temperature within microfluidic systems were Time Correlated Single Photon Counting (TCSPC) and Fluorescence Lifetime Imaging Microscopy (FLIM). A generic description of these techniques and the relevant theory is presented within this chapter. However, precise experimental details are described in the relevant chapters, including the preparation of the fluids and their storage. The time-resolved fluorescence measurements were performed using equipment maintained within the Collaborative Optical Spectroscopy, Micromanipulation and Imaging Centre (COSMIC) at the University of Edinburgh.

3.1 Excitation source

For this thesis the excitation source employed was a tuneable, femtosecond-pulsed Titanium:Sapphire (Ti:Sapphire) laser system (Coherent Mira 900-F), which was mode-locked. This was pumped by a continuous wave solid state laser using a Neodymium:Vanadate lasing medium (Coherent Verdi V-10). The pumping laser delivers visible light at 532 nm to a maximum power of 10 W. The Ti-Sapphire laser produces a pulsed fundamental beam, which is tuneable between 700 nm and 1000 nm. The pulses had widths of approximately 200 fs with a repetition rate of 76 MHz, hence one pulse approximately every 13 ns. A full explanation of the theory behind the Ti:Sapphire laser is beyond the scope of this thesis, but a brief explanation of the practical workings of the laser is applicable.

The excitation pulses produced by the Ti:Sapphire laser were not useful for time-resolved fluorescence experiments due to the high repetition rate and long wavelength range, however, the short pulse duration is ideal. The fluorophores employed within this thesis are directly excitable in the ultra-violet (250 – 400 nm) and visible (400 – 700 nm) regions of the spectrum, as is also true for most common fluorophores. The fluorescence emitted from several of the fluorophores used in this study, and many others in general, persists significantly longer than the 13 ns between Ti:sapphire laser pulses. Thus photons of fluorescence emitted from molecules excited by one pulse continue to arrive at the detector as those from a subsequent pulse start to arrive at the detector. Therefore it is impossible to correctly time the arrival of a photon at the detector relative to its excitation pulse. This renders the resulting decay curve meaningless.

To solve these limitations, firstly, the repetition rate of the laser is reduced by passing the pulses through a pulse picker (Coherent Model 9200). This effectively blocks the transmission of all pulses except one in every sixteen pulses. This one pulse was deflected towards the sample to excite fluorescence. Hence the repetition rate of the laser is reduced to a frequency of 4.75 MHz, which provides one pulse approximately every 210 ns allowing complete decay of the fluorescence intensity between pulses. The drawback is the considerably reduced average power of the laser beam. This is not a problem for TCSPC, which is a very sensitive technique and is not limited by the laser power, however, this increases the exposure time for the CCD camera detector used for FLIM.

Following the reduction of the repetition rate of laser pulses, the laser beam is directed into a harmonic generator (Coherent 5-050), which is employed to frequency double the light. This halves the wavelength of the light from the fundamental wavelength, typically set to provide maximum output power at 800 nm, to the second harmonic wavelength of 400 nm. Hence, enabling the excitation of the fluorophores used in this thesis. The exact excitation wavelengths are quoted in the relevant chapters. The average power of the second harmonic in general ranged from 5 mW to 8 mW, as measured using a meter (Field Master, Coherent).

3.2 Time Correlated Single Photon Counting (TCSPC)

Time correlated single photon counting (TCSPC) is the experimental technique employed to perform the time-resolved fluorescence spectroscopy used within this study to measure the fluorescence lifetimes of various fluorophores under defined conditions. Fluorescence lifetimes determined from TCSPC were used to construct calibration graphs correlating either fluid temperature or composition of fluid samples directly to the lifetimes. The calibration graphs were necessary to directly convert FLIM maps (spatially resolving the fluorescence lifetimes) to temperature or composition maps.

3.2.1 The principle of TCSPC

Following the excitation of a fluorophore with a short pulse of light, the first photon of fluorescence emitted is detected and the time interval between the excitation and detection of the photon is recorded. This procedure is continuously repeated to enable a complete distribution of individual photon arrival times at the detector. The fluorescence lifetime(s) of the fluorophore sample can then be calculated from this recorded fluorescence intensity decay. Figure 3.1 displays a generic experimental setup typically used for TCSPC techniques.

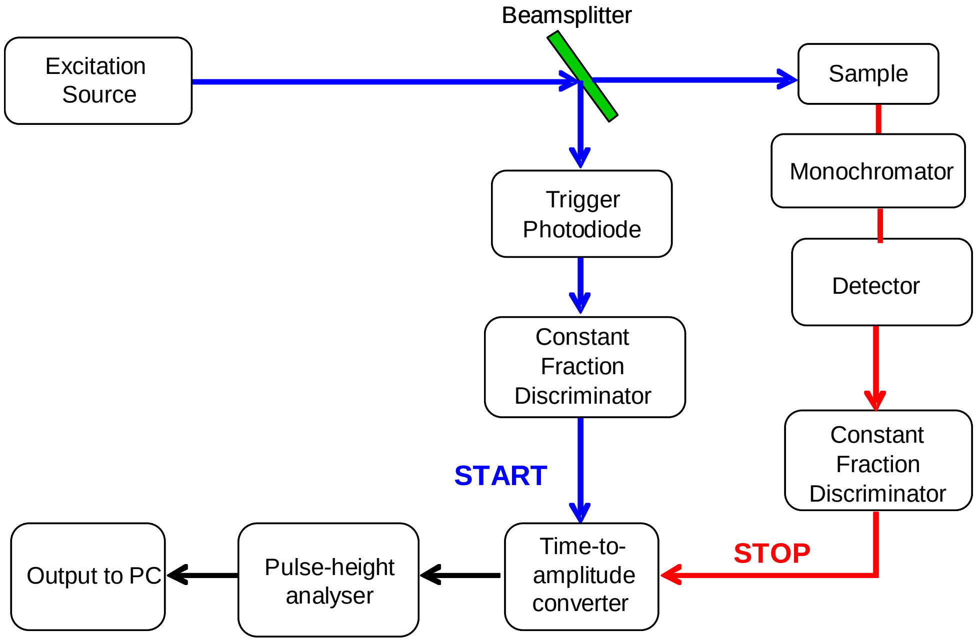

Figure 3.1: Diagram showing the generic setup necessary to perform TCSPC measurements with the individual components identified.

Each excitation pulse triggers an electronic ‘START’ pulse for the timing. This was achieved by extracting a fraction (~10%) of the excitation pulse using a beam splitter (Figure 3.1) and directing it to a fast photodiode to convert the optical signal to an electrical triggering pulse (the ‘START’ pulse). The electrical pulse then passes through a constant fraction discriminator to minimise variations in the trigger timings, to a device analogous to a stopwatch called the time-to-amplitude converter. The time-to-amplitude converter can be considered as a capacitor which begins charging when triggered by the ‘START’ pulse and stops when triggered again by a ‘STOP’ signal. The threshold differentiation for the START pulse was set at -300 mV, therefore, START pulses with a magnitude below the threshold did not trigger the time-to-amplitude converter. The amplitude of the pulse could be varied depending on the incident light intensity on the photodiode. Both the constant fraction discriminator and the time-to-amplitude converter are discussed in greater detail in subsequent sections.

The remainder of the excitation pulse, which is reflected by the beam splitter, is directed towards the sample and emission of photons by fluorescence is detected.

The TCSPC detector operates by converting the emitted photon energy into an electrical pulse. The ‘STOP’ pulse, produced by the first detected photon, passes through a constant fraction discriminator and then halts the voltage ramp at the time-to-amplitude converter. Then, the time-to-amplitude converter is discharged to allow the electrical signal to be quantified, as this is proportional to the time between the start and stop triggers. A pulse-height analyser converts the electrical signal into a digital signal. This is recorded as a single count on a histogram of fluorescence intensity against time. Typically hundreds of thousands of these counts are registered to display an exponential decay curve, which allows the calculation of the fluorescence lifetime of the fluorophore under defined conditions.

3.2.2 TCSPC Components

3.2.2.1 Microchannel plate

A microchannel plate (MCP) photomultipler tube was used to detect single photons and convert their energy into electrical signals. The MCP is a metal plate, containing channels with an internal diameter of between 6 μm and 25 μm, which is sandwiched between a photoanode and cathode. The function of the channels is to amplify an initial electronic signal following the impact of an arriving photon on the photocathode (Figure 3.2). The collision of the photon causes the emission of a photoelectron from the cathode, which is accelerated towards the anode by a potential difference across the MCP. During transit the photoelectron collides with the channel walls, which are lined with dynode material. The impact causes the emission of secondary electrons and subsequent repetition of this process leads to a logarithmic increase in the current of the channel. The initial current can typically be amplified 10000 times using this method to provide a measurable current at the anode.

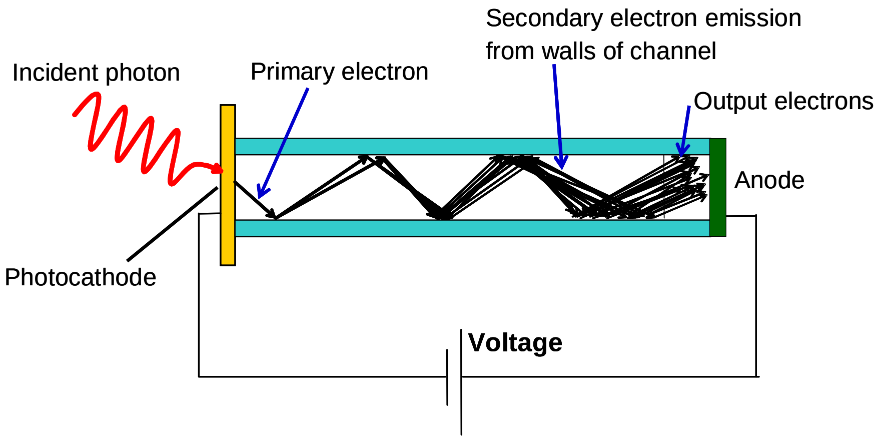

Figure 3.2: Diagram of the operating mechanism of an isolated channel from a microchannel plate photomultiplier tube.

In TCSPC, the time resolution of the system is heavily dependent on the variation in the time taken for electrons to pass through the detector. This transit time spread (TTS) increases the uncertainty in the photon arrival timing and occurs due to the numerous possible routes through the PMT channels providing a distribution of photon arrival times. Figure 3.2 pictorially illustrates this phenomenon, where the single incident photon produces a multitude of output electrons with different transit times. The microchannel plate employed for TCSPC has a transit time spread of 25ps.

3.2.2.2 Time-to-amplitude converter (TAC)

The time-to-amplitude converter (TAC) produces an electrical pulse whose amplitude is proportional to the time interval between the start and stop pulses. The start pulse triggers the TAC to begin accumulating charge, which continues until a stop signal is detected. The capacitor is then discharged and the amplitude of the electrical output pulse is related to the time lapsed. The TAC is then reset to commence a new cycle. During the discharge and resetting period no incoming signals can be detected. This is referred to as the ‘dead time’ of the TAC and is less than 150 ns in duration for the system used to record decays curves throughout this study.

If the count rate (rate at which photons are recorded) is too high, this can result in more than one pulse arriving at the TAC during a single cycle. This phenomenon called pulse pile-up can introduce errors into the timings of the photons as the first photon will be recorded. This results in a bias of the TAC to record shorter lifetimes. This problem can be avoided by ensuring that the count rate is considerably lower than one photon per excitation pulse. This makes sure that the probability of a second photon arriving in the same excitation cycle is extremely low. Therefore, a true representation of the exponential decay curve is recorded.

3.2.2.3 Constant Fraction Discrimination

The electronic pulse output signals from the photodiode (START trigger signal) and the photomultipler tube detector can vary in amplitude, which can affect the timing of the trigger signals detected by the time-to-amplitude converter. This effect is illustrated in Figure 3.3, which shows the time variation in detecting a pulse based on a threshold voltage level, for pulses of different amplitudes.

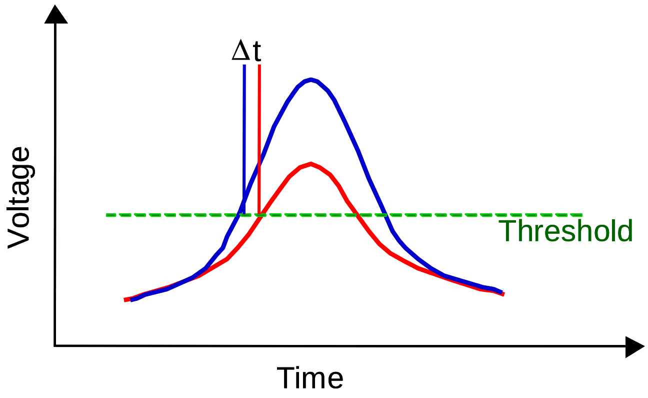

Figure 3.3: Illustration of timing varitation from employing leading edge discrimination techniques to detect pulses.

This form of pulse detection (leading edge discrimination) is dependent on the leading edge of the pulse reaching a threshold value to trigger the timing. Using leading edge discrimination results in the spread of timings hence increasing the timing uncertainty and broadens the instrument response function.

To overcome this timing uncertainty, the technique of constant fraction discrimination is employed. This technique, as illustrated in Figure 3.4, divides the incoming pulse, by a predetermined fraction usually 2/3 or 1/3, to create two pulses. The smaller fraction pulse is inverted, whilst the other is delayed by half the pulse width. The two pulses are then recombined to provide a profile with a potential that crosses zero at a point that is independent of the amplitude. This ensures the consistent timing of pulses for time-resolved experiments.

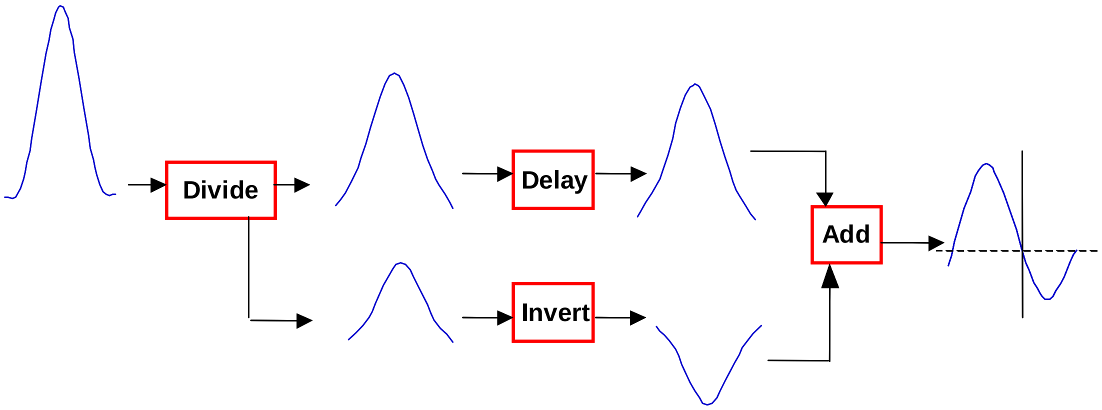

Figure 3.4: Schematic illustrating the technique of constant fraction discrimination.

3.2.3 Experimental Procedure

Both the constant faction discriminator and the time-to-amplitude converter are located on the Edinburgh Instruments TCC900 photon counting card and were controlled from the Edinburgh Instruments ‘F900’ software interface.

Inside the spectrometer sample chamber (FL920 series spectrometer, Edinburgh Instruments) the aqueous samples were contained within fused silica cuvettes mounted onto two orthogonal translation stages, which allowed the fine adjustment of the cuvette’s position relative to the incident excitation beam and the detector. The excitation light that passed through the sample, i.e. light that was not absorbed by the sample, was directed into a beam stop, also positioned within the sample chamber. The resulting fluorescence emission was collected at right angles to the excitation beam. The emission light passes through an adjustable aperture and lens to focus the light into the detector. The aperture is essential to limit the dispersion of the resulting emission and is fundamental in controlling the instrument response function. The diameter can be varied between 2 mm and 37 mm, and was employed to control the sample volume from which fluorescence was detected. In principle the wider the aperture, the larger the area of photons that are incident on the detector and hence the transit time spread through the microchannel plate was increased. This results in a wider instrument response function.

After the emission has past through the aperture, it was firstly focused through a lens, before progression through an emission polariser, then the entrance slit of a monochromator, then passage through the exit slit, before finally reaching the detector. The monochromator slits were set to permit a 10 nm bandpass of the emission light.

For the microchannel plate detector (Hammamtsu R3809-50) typically a STOP count rate of ~20 000 Hz was employed, this is the limit at which the detector can function without causing long term deterioration. The STOP count rate was controlled using neutral density filters in the excitation beam path before entering the sample chamber, in addition to varying the emission aperture.

Following any adjustments, including the emission aperture, slit widths, excitation beam height and direction, an instrument response function was collected. This is performed using a dilute solution of Ludox (Aldrich), a suspension of colloidal silica, to scatter the excitation light. Although the instrument response is collected using identical setting for collecting decays of samples, the STOP count rate was reduced using neutral density filters to ~2000 Hz. Typically the instrument response function had a full width at half maximum height (FWHM) of 70 ps. Fluorescence decay curves of samples were recorded into 4096 channels and accumulated to 10,000 counts in the peak channel on various time ranges as defined in the relevant chapters. In some circumstances the sample solutions scattered significant amounts of light, hence a long-pass filter (Schott) was employed to prevent scattered light reaching the detector. The recording of the decay curves was undertaken using the Edinburgh Instruments ‘F900’ software.

3.2.3.1 Fluorescence decay fitting procedure

The analysis of the lifetimes was undertaken using the Edinburgh Instruments ‘F900’ software. When required, global analysis of data sets was performed using Alango ‘FAST’ software. Individual decay curves were firstly fitted with a single exponential, followed by inspection of the residuals of the fit and observation of the magnitude of the reduced χ^2 parameter, these terms are fully explained in the subsequent Section 3.2.4. If these assessment criteria were deemed unacceptable, then additional exponential components were introduced into the theoretical decay. The TCSPC decays were fitted to correlate with the decay fitting parameters employed within the FLIM analysis, which involved tail fitting after the decay of the excitation source. Typically the fit was stopped at the end of the decay curve or when the photon counts were approaching five times the background value. The background count was fixed as a constant parameter in each fit and was assessed from the background count arriving before the rising edge of the instrument response function.

3.2.4 Data processing and analysis

3.2.4.1 Instrument response function (IRF)

The transit time spread (TTS) forms a major contribution to the Instrument Response Function (IRF) for TCSPC, which is defined as the response of the instrument to a delta pulse (infinitesimally short pulse) and in practice is measured as the response function (decay curve) of the excitation laser pulse. For TCSPC, the IRF is recorded by scattering some of the incident laser light from a non-fluorescent colloidal suspension into the detector. The full width at half maximum intensity (FWHM) of the IRF is mainly determined by the TTS, but is also affected by the collection optical geometry, the passage of light through the detection monochromator, discriminator settings etc. Figure 3.5 shows a typical IRF recorded by TCSPC, with a FWHM of 70 ps. The laser pulse typically has a FWHM of ~200 fs. The low intensity ‘afterpulses’ (note the logarithmic scale) are intrinsic to the MCP detector in the timing circuits.

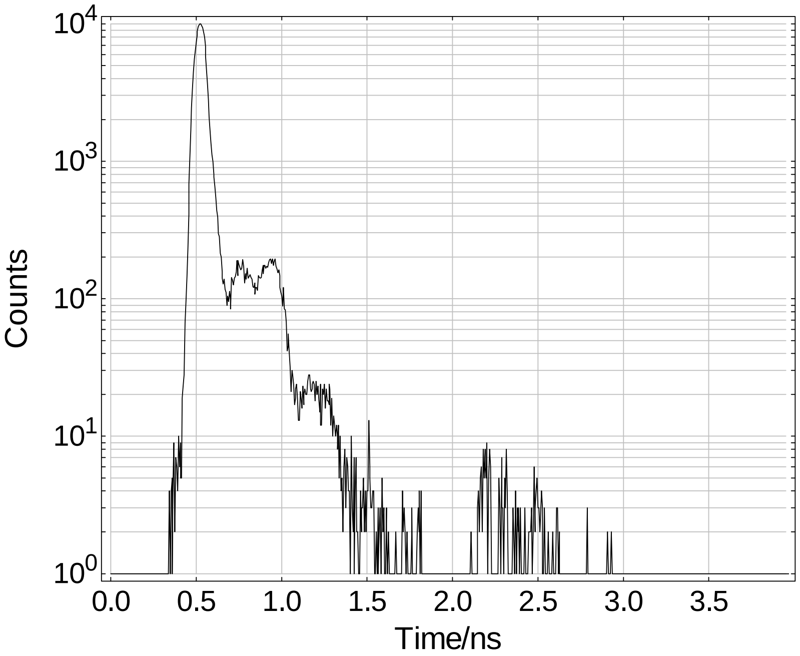

Figure 3.5: A typical instrument response function with a FWHM of 70 ps recorded by TCSPC. Note that the y-axis is shown on a logarithmic scale.

3.2.4.2 Analysis of TCSPC data

Figure 3.6 shows a single exponential decay curve (black) for a fluorescent probe, 1,8-anilinonaphthalene sulfonate (ANS), in pure methanol along with the corresponding IRF (red), as an example of the data obtained from a TCSPC experiment.

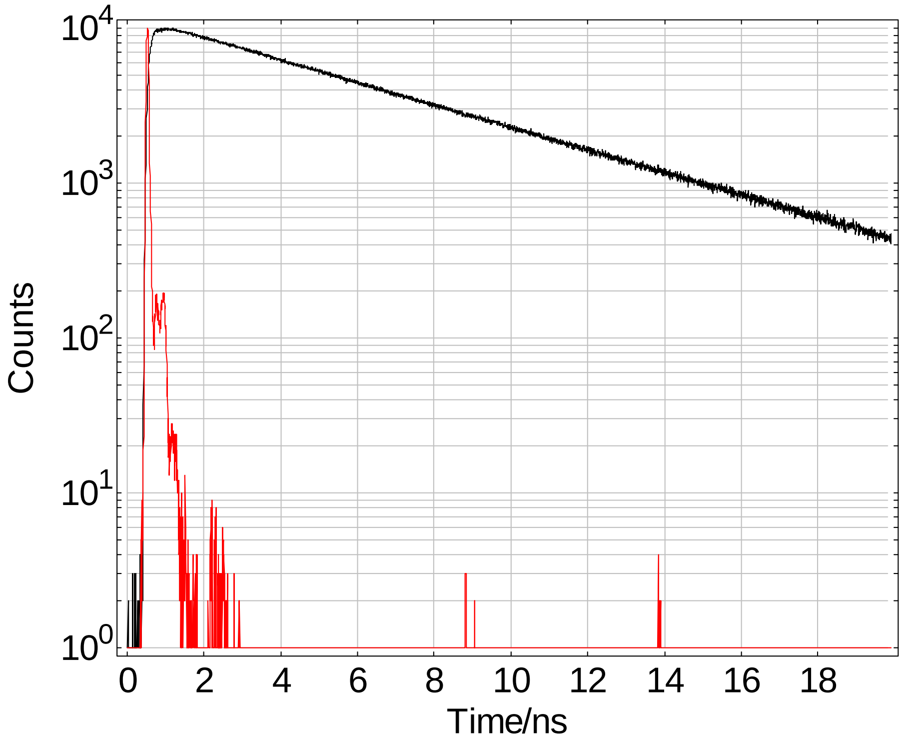

Figure 3.6: Example of data obtained from a typical TCSPC experiment. The exponential decay function is that of ANS in pure methanol (black profile) along with the corresponding IRF (red profile). The number of counts per channel is plotted on a logarithmic scale in order to illustrate the distribution more clearly.

The fluorescence decay curve is iteratively fitted to a multi-exponential decay function, as shown by Equation 3.1.

$$I(t) = \sum_{i=1}^{n} A_i \exp\left(\frac{-t}{\tau_i}\right) + B \qquad \text{Equation 3.1}$$

where τ_i is the fluorescence lifetime, A_i, the “A-factor”, is the fractional amplitude of the ith decay component, and B is the background. The A-factor indicates the fraction of the emitting molecules that has a particular lifetime, τ_i. ΣA_i is normalised to unity.

The fluorescence decay curves throughout this study were analysed by tail-fitting (i.e. without convolution with the instrument response function) to correlate with the fitting of the decay curves recorded by FLIM.

A value for τ is determined by minimising the weighted sum of squares of residuals between the fitted function and the experimental data. This is referred to as least squares fitting and is done by minimising Equation 3.2.

$$\chi_a^2 = \sum_{i=n_1}^{n_2} \left\{ \frac{\left[I_0(t_i) - Y(t_i)\right]^2}{I(t_i)} \right\}$$ Equation 3.2

where $I_0(t)$ is the background corrected intensity, Y(t) is the fitted function and I(t) is the uncorrected intensity, n_1 and n_2 are the first and last channels in the region of analysis respectively.

The quality of any given fit is judged from the value of the reduced chi-squared function, χ^2

$$\chi^2 = \frac{\chi_a^2}{n_2 - n_1 + 1 - p}$$ Equation 3.3

where p is the number of variable parameters in the fitting function. A χ^2 value of 1 indicates a perfect fit has been achieved. Values that deviate from this can be the results of either a poor fit or of ‘imperfect’ data. For the system used in this study a value for χ^2 of less than 1.2 typically describes a ‘good fit’.

The goodness of fit of a decay curve can be illustrated by a plot of weighted residuals. The weighted residual values, r(t), between experimental and fitted points are determined using Equation 3.4.

$$r(t_i) = \frac{I_0(t_i) - Y(t_i)}{\sqrt{I(t_i)}}$$ Equation 3.4

3.3 Fluorescence Lifetime Imaging Microscopy (FLIM)

Fluorescence lifetime imaging microscopy (FLIM) is the experimental technique employed within this thesis to spatially resolve the fluorescence lifetimes of fluids within microfluidic devices. Calibration graphs correlating either fluid temperature or composition of fluid samples directly to the lifetimes, as determined by TCSPC, were used to convert the fluorescence lifetime images into temperature or composition maps of the fluids within microfluidic systems.

3.3.1 The FLIM Detector

The FLIM detector consists of a time-gated image intensifier (PicoStar HR) connected to a peltier-cooled charge-coupled device (CCD) detector (Imager 12QE). Hence, this imaging system is commonly referred to as CCD FLIM due to the detector system and to distinguish it from single photon counting techniques to produce fluorescence lifetime images (time- and space-correlated single photon counting). However, throughout this thesis it will be referred as FLIM as no single photon counting techniques were employed to spatially resolve the fluorescence lifetimes of fluids. The image intensifier consists of a single microchannel plate (MCP), as previously described in Section 3.2.2.1, with typical channel diameters of 6-10 μm to amplify the signal generated from the detection of photons to a detectable electrical current. The intensifier is a vacuum tube with three main elements of a photocathode, a microchannel plate and a phosphor screen (Figure 3.7).

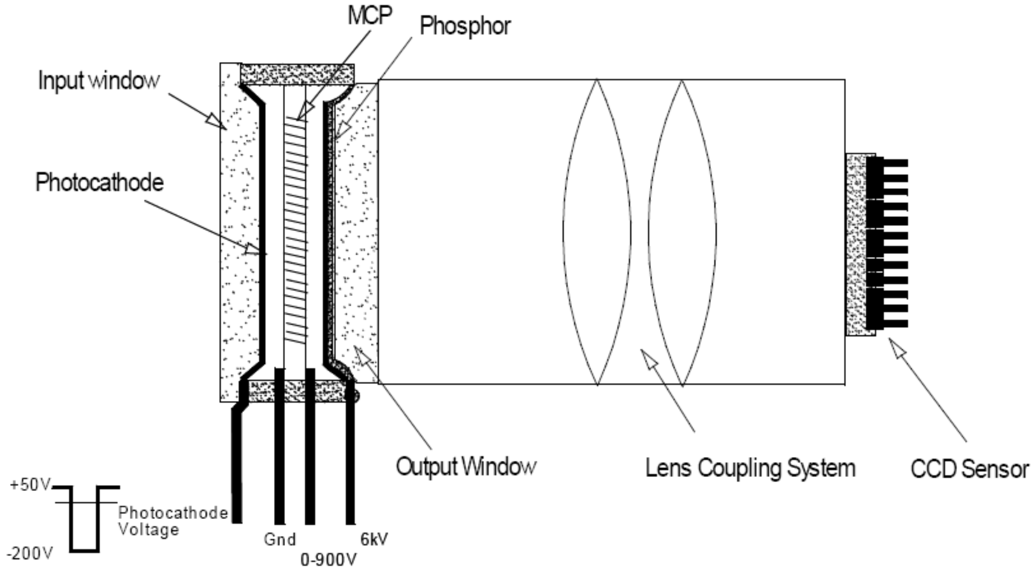

Figure 3.7: Diagram showing the main components of the time-gated intensified CCD camera employed for FLIM.[30]

The fluorescence emission is focused onto the photocathode, where the impinging photons cause the emission of electrons. A large negative voltage (-180 V) is applied to the cathode, which controls the temporal gate width and causes the electrons to be accelerated towards the MCP. The delay of the intensifier was controlled by a DEL150 picosecond delay module (Becker and Hickl) located in the control computer. The electron impact on the walls of the channels results in a cascade of secondary electrons to amplify the initial signal. The electrons are accelerated onto the phosphor layer by a high voltage resulting in the generation of “green” photons (in the green colour region), which are then imaged onto the CCD detector *via* the lens system. The CCD detector consists of a dense two dimensional array of photodiodes (pixels), which detects the photons emitted from the phosphor with the light energy converted to an electronic charge. Hence an optical input imaged onto the phosphor layer, acting as a luminescent screen, is converted into an electronic output image. The accumulated charge of each pixel is read and information transferred to the computer, taking on average 50 ms for each image.

3.3.2 Experimental Procedure

Fluorescence lifetime images were obtained using wide-field illumination of microfluidic devices and the collection of the resultant fluorescence in a short time window at a particular delay time after the laser pulse, using the gated intensified CCD camera. A series of images was acquired by varying the delay time between the detection window and the laser pulse, thereby sampling the entire fluorescence decay of the molecular probe (Figure 3.8). The data from each pixel was then fitted to an exponential decay, from which a lifetime map was produced of the spatial distribution of fluorescence lifetimes in a sample.

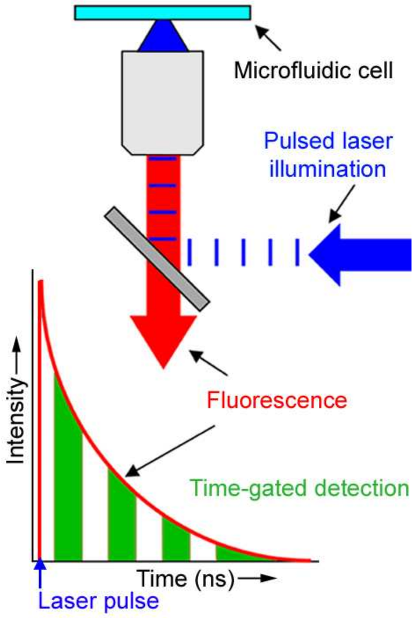

Figure 3.8: Schematic of fluorescence lifetime imaging microscopy, illustrating how the fluorescence decay is built up from the time-gated detection.

A schematic of the equipment used for the fluorescence lifetime imaging microscopy measurements is displayed in Figure 3.9.

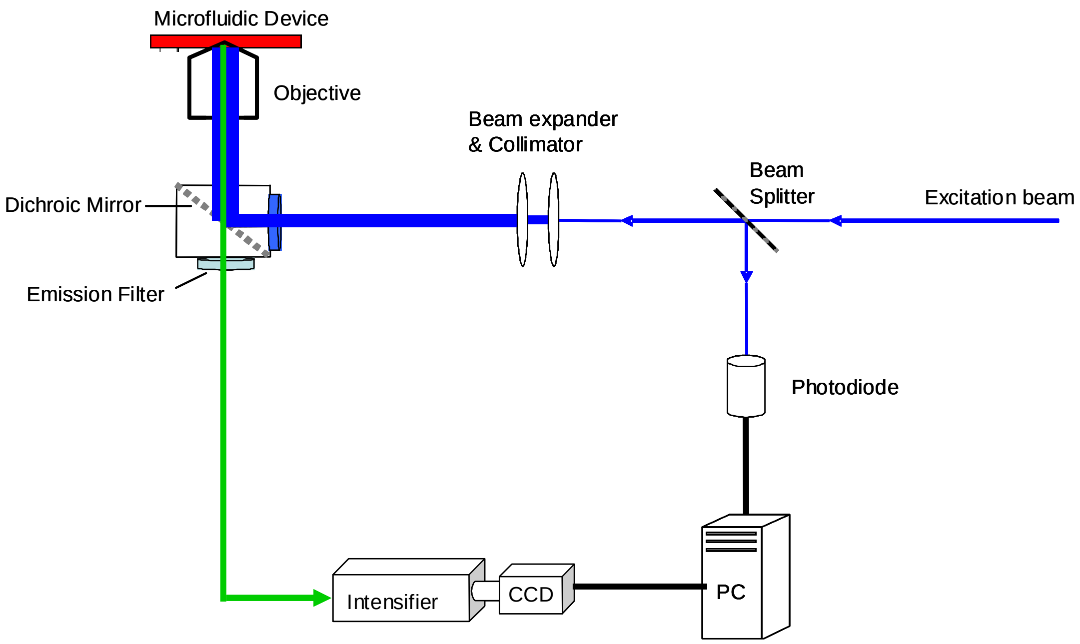

Figure 3.9: Schematic of the equipment used for FLIM to spatially map the fluorescence lifetimes of various aqueous solutions within a microfluidic device.

The excitation beam was split and one portion (~10%) was used to trigger a fast photodiode. The output from the photodiode was first passed through a constant fraction discriminator (CF4000, Ortec), and then used as the START trigger signal for the time-gated intensified CCD camera employed in the FLIM system. The threshold differentiation for the START pulse was set at -400 mV, therefore, START pulses with a magnitude below this threshold did not trigger the time-gated intensifier. The amplitude of the pulse could be varied depending on the incident light intensity on the photodiode. The remaining majority of the excitation beam was expanded, collimated and directed into a Nikon TE300 inverted microscope operating in an epifluorescence configuration. This excitation light was reflected from a dichroic filter (Nikon) mounted in a standard filter cube and focused onto the microfluidic device using a selection of Nikon objectives ranging from 4× to 100× magnification, as detail in the relevant chapters. The laser power incident on the microfluidic device was typically around 100 μW. The resultant fluorescence was collected through the same objective, passed through a barrier filter (Nikon) and imaged onto a Picostar HR-12QE gated intensified CCD camera system (LaVision GMBH, Berlin).

The experiments described within this thesis were conducted with either a 300 ps or 600 ps gate width, which was measured by detecting laser light reflected from a mirror (the minimum gate width for this camera is 200 ps). The intensifier gate was delayed relative to the START laser trigger signal using a DEL150 picosecond delay module (Becker and Hickl). The 12-bit CCD camera is a progressive scan interline sensor, with 1370 (H) by 1040 (V) pixels (pixel size is 6.45 μm × 6.45 μm).

Images were the average of 5 separate exposures employing 4 × 4 hardware binning. Each intensity image was the average of 5 separate exposures, the acquisition time of each was the sum of the CCD exposure time plus the 50-ms camera readout time. Details of the time range recorded over, the time increment step change for the gates, gate width, threshold counts, CCD exposure time and total acquisition time are presented in the relevant chapters.

The excitation intensity was adjusted to give a peak intensity of between 3000 and 4000 counts in the brightest image, which corresponds with the start of the fluorescence decay. The background signal of *ca.* 50 counts was subtracted from each image. The Picostar system and delay card were controlled, and the data was analysed, using DaVis 6.2 software running the Picostar DaVis module.

To ensure that the instrument response did not interfere with the fitting, an instrument response function (IRF) was recorded, as explained in more detail in the subsequent Section 3.3.3.1. From this it was established in which image the excitation source had decayed sufficiently to allow the fluorescence decay to be fitted from. It was thus established that the fluorescence decay could be fitted from 0.4 ns or 1 ns after the emission peak image without distortion by the instrument response. Therefore images after this time were analyzed, allowing a decay curve to be constructed for each pixel. Pixels with low counts in the first analyzed image (typically 700 counts) were removed at this stage. Each of these curves was then fitted to a single exponential decay. A lifetime map was produced by assigning a colour on a 16-bit pseudocolour scale to each of the fitted lifetimes, and these were displayed over a suitable range.

Although the FLIM software can only produce lifetime images from fitting the fluorescence decay to a single exponential, it allows the selection of a region of interest within an image and the ability to fit this data to multiple exponentials. This fitting was used in the present work to ensure accurate average lifetime values for the fluorescent polymer solution used for high resolution temperature measurement (Chapter 6).

The FLIM software allows the continuous observation of the gated intensity images, recorded to construct the FLIM image, which is crucial to ensure that no flow fluctuations or air bubbles perturbed the fluids within the microfluidic devices during the data acquisition.

3.3.3 Data processing and analysis

3.3.3.1 Instrument response function (IRF)

For FLIM the IRF is recorded by detecting excitation light reflected from a mirror, positioned on the microscope platform in the place of the microfluidic device under investigation. The emission filter is removed to record the IRF, however, the dichroic mirror remains in place to allow only a small fraction of the excitation light reflected off the mirror to be transmitted and recorded. The recording of an IRF is necessary to determine the gate width of the intensified detection system, as the default software settings are specific for an operating trigger frequency of 80 MHz. The operation of the detector with a trigger frequency of 4.75 MHz, as used in this study, results in a wider gate width. The gate width is set by a defined negative voltage applied to the photocathode and can be controlled through the software. Figure 3.10 shows a typical IRF record by FLIM, with a FWHM of 0.6 ns, defined by the temporal width of the detection gate.

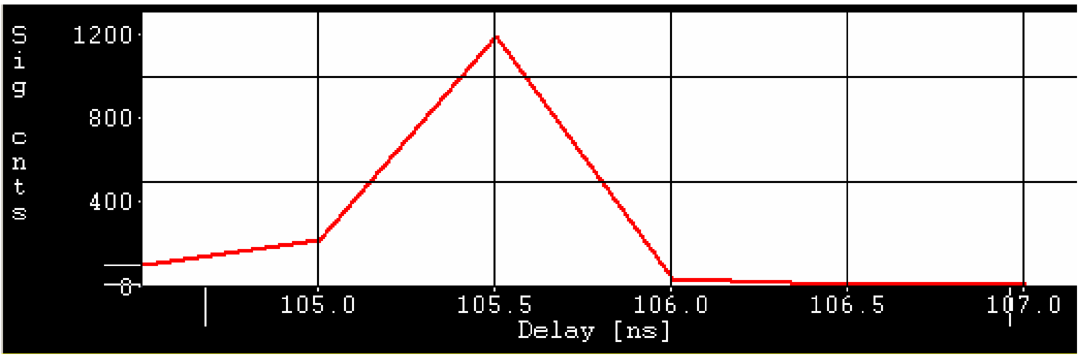

Figure 3.10: A typical instrument response function with a FWHM of 0.6 ns recorded by FLIM.

3.3.3.2 Fluorescence decay fitting procedure

The fluorescence decay curves recorded by FLIM and TCSPC were both analysed by tail-fitting from after the falling edge of the excitation pulse. The FLIM software is unable to deconvolute the fluorescence decay from the IRF, unlike the F900 software employed in the TCSPC data acquisition and analysis. Therefore the FLIM equipment is unable to determine fluorescence lifetimes with magnitudes significantly less than the width of the IRF, whereas with the TCSPC system lifetimes can be resolved down to ~20 ps.

3.3.3.3 Analysis of FLIM data

Figure 3.11 shows the fluorescence decay curve (blue profile) for ANS in pure methanol along with the fit of a single exponential theoretical decay as an example of the data and analysis obtained from a FLIM experiment.

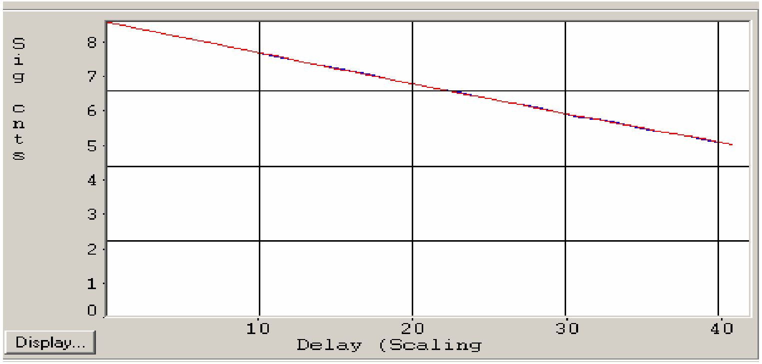

Figure 3.11: Example of data obtained from a typical FLIM experiment. The exponential decay function is that of ANS in pure methanol (blue profile) along with the corresponding single exponential fit overlaid (red profile). The red profile is overlaying the blue profile, hence obscuring it. The intensity per time gate is plotted on a logarithmic scale in order to illustrate the distribution more clearly.

The FLIM software will use the same method as F900 (minimising sum of squares) employed in the TCSPC analysis, although it does not produce output residuals. Typically fifty intensity images are recorded, from which single exponential decay functions are fitted per pixel to produce a FLIM image. Although the FLIM image is constructed from single exponential fits, regions of interest are selected to verify acceptable fits to a single or multi-exponential decay fits. The time-gated detection system has previously been extensively investigated and validated against a time- and space-correlated single photon counting detector attached to the microscope.[31;32] These studies concluded that the time-gated detection system produced accurate lifetime values for simple decays.

In some instances, the intensity decay data recorded by the FLIM system was exported and analysed using the TCSPC software (F900). Figure 3.12 shows the residuals from fitting data recorded by FLIM to illustrate the satisfactory fit, evident from the randomness of the residuals across the whole decay.

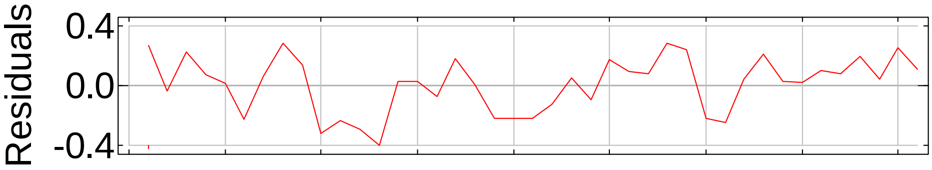

Figure 3.12: The residuals from fitting a single lifetime to the fluorescence decay for ANS in pure methanol. The fluorescence decay was recorded by FLIM and the analysis was performed using F900 software, primarily used for TCSPC data acquisition and analysis.

Chapter 4

Quantitative spatial mapping of mixing in microfluidic systems

4.1 Introduction

Many of the benefits of microfluidics arise from the reduction in size, but the miniaturisation results in a fundamental change in the flow characteristics of fluids at this scale. Turbulent flow predominates at the macroscale, while fluids flow in a laminar fashion at the microscale, without the random mixing that is characteristic of turbulence.[10] Turbulence can rapidly and effectively mix fluids at the macroscale. However, turbulence cannot be generated in microscale flows due to the small dimensions typically used.[33] The laminar flow conditions generated at the microscale mean that multiple fluid streams tend to flow in parallel through microchannels, mixing only by diffusion across their interfaces.[33;34] This diffusion-limited mixing is extremely inefficient and slow. Whilst laminar flow behaviour has been exploited to good effect in microanalytical systems, many emerging applications of microfluidic devices require rapid and efficient mixing.

Miniaturisation of the fluid handling of chemical and biological samples heralds many advantages. However, the ability to integrate all the components required for performing multiple tasks to replace a laboratory can be problematic.[35] Although there is considerable ongoing research and development of fully integrated miniaturised devices or micro-total-analysis-systems (µTAS), views have been expressed that more effort should be focused on individual operations or components to accomplish the goal of µTAS.[36] Miniaturising the mixing process is one such operation that has been identified. Indeed, the problem of microfluidic mixing has been described as a major bottleneck in the performance and development of microfluidic devices[35] and is widely acknowledged to be a significant problem.[9;35;37]

4.1.1 Importance of microfluidic mixing

The area of mixing has received much attention within the microfluidic research community over the past few years, due to the importance of achieving effective and efficient mixing at the microscale. For example, the majority of chemical assays require mixing of reagents and some assays even require multiple mixing steps.[8;33;36] Other applications where rapid mixing is important include drug delivery, biochemical analysis, sequencing or synthesis of nucleic acids, DNA analysis, protein folding, enzyme reactions, cell activation, and many other biological processes.[38;39] Active research into microfluidic mixing is also important for understanding fundamental transport processes that occur at the microscale.[8]

The importance of microfluidic mixing is widely acknowledged and generates extensive research efforts, as displayed by the numerous publications and patents on microfluidic micromixers over the past decade.[37] Already there have been several review articles published on micromixers alone.[8;40;41] This reflects the increasing rate of publication of the new mixer designs and the continued drive to conquer the miniaturisation of mixers able to rapidly mix fluids at the microscale.

4.1.2 Microfluidic mixing strategies

In microfluidic devices, the purpose of mixing is generally to bring together solute species from two (or more) flows. In the laminar flow regime, mixing occurs slowly by diffusion of solute (and solvent) molecules across the flow boundary. To achieve rapid mixing, laminar flow can be disrupted to give chaotic mixing, in which there is bulk transfer of fluid (solvent carrying solute) between the flows. However, fast mixing can be achieved in some designs by exploiting diffusion alone, for example, multi-lamination mixing arrangements. In some mixing designs the pay-off of more rapid mixing can result in increased back-pressure.

Micromixers are generally categorised into passive (static) or active devices.[37] Passive micromixing strategies do not require external energy but rely on diffusional mixing, using multilamination or flow-splitting techniques to reduce the mixing equilibration time.[36;37;41] To increase the mixing rate beyond that limited by diffusion, passive mixers that induce lateral transport of fluid between streams have been devised relying on chaotic advection techniques.[23;42] Active micromixers require external energy to generate a disturbance to chaotically intersperse fluid flows.[36] Table 4.1 displays a general classification scheme for common passive and active mixing strategies.

Passive	**Active**
Multi-lamination arrangements	Acoustically induced vibrations
Split-and-recombine concepts	Ultrasound
Chaotic advection	Periodical variation of pumping capacity
Droplet based	Thermal
Injection e.g. micro nozzles	Impellers
	Electrokinetic instabilities
	Pieoelectrically vibrating membrane
	Micro pumps or valves
	Magneto hydrodynamic action

Table 4.1: Classification scheme for micromixers.[8;41]

4.1.3 Characterisation techniques for determining mixing efficiency

As noted above, the number of publications and the commercial development of microfluidic mixers has grown rapidly over the past few years. In spite of the increasing attention paid to the mixing problem, many devices are still considered to be designed by trial-and-error methods.[9;42] The characterisation of micromixers continues to represent a challenge to evaluate designs and accurately quantify mixing efficiency.[8;36] There has been a variety of techniques used to evaluate micromixers, the common methods are reviewed within this chapter.

4.1.4 Flow and mixing visualization

Flow visualization techniques are one of the most common methods used to evaluate microfluidic mixing.[8;41] Optical techniques can be extremely useful and powerful in providing spatial and temporal information on conditions within microfluidic devices. Frequently fluorescence intensity imaging and transmitted light microscopy are used. These techniques are relatively cheap, easy to set up, and, in the case of fluorescence imaging, provide excellent contrast. Unfortunately, the ability of these intensity-based techniques to provide a quantitative picture of fluid composition in microfluidic systems is severely compromised by their sensitivity to variations in the optical path, instability of the light source, scattering, uncertainty in the dye concentration, and photobleaching effects.[18] It has been acknowledged that the mixing efficiency can be overestimated using a dilution mixing technique (fluid with dye, mixed with un-dyed fluid), as a result of the resolution of the imaging system.[33]

4.1.5 Fluorescence intensity imaging

Numerous publications have relied on fluorescence intensity imaging techniques to test micromixers, due to their versatility and ease of application.[4;23;27;33;35;36;42-51] This approach can be used to obtain two dimensional images using a standard epifluorescence microscope or three dimensional resolution using confocal imaging techniques to optically section through a microfluidic device. The spatial resolution of the technique can be combined with temporal resolution by the use of high-speed cameras to monitor flow and mixing in real-time, aptly suitable to evaluate dynamic mixing processes. A fluorescent tracer dye is usually added to one of the fluid streams entering the micromixer, commonly fluorescein is used as the fluorescent dye.[23;27;33;36;46;51] Several researchers have evaluated the performance of their micromixer designs using separate fluid streams of a commercial Ca^{2+} sensitive dye and $CaCl_2$ solution, which when mixed displayed an increase in fluorescence intensity.[4;35]

Sasaki *et al.* used solutions of fluorescein and rhodamine B (RhB) separately, to characterise microscale mixing induced by applying an AC voltage between electrodes fabricated onto a microchannel.[43] The fluorescence intensity images produced were reported to be difficult to interpret due to distortions and optical effects from the electrodes. The intensity images had to be 'corrected' to remove these optical effects. Two different fluorescent dyes were used to assess any electrolysis effects induced by the electric current, by comparing mixing results using an anionic dye molecule (fluorescein) and a cationic dye molecule (RhB). Both dyes yielded similar results. Applying an AC field to induce mixing can cause thermal heating effects,[43] the researchers were possibility unaware of the high temperature sensitivity of the fluorescence intensity of RhB, which would have compromised their results.[52] The temperature sensitivity of RhB is discussed in Chapter 6.

Johnson *et al.* also used RhB dye to investigate mixing within a novel micromixer designed for electroosmotic flow.[42] The authors openly acknowledge that Joule heating can be a significant problem in these systems and from their previous research had demonstrated temperature increases of 30 ^{o}C within such a micromixer. Again they have used a fluorophore (RhB) which is highly sensitive to temperature and is commonly used to measure temperatures within microfluidic devices. Due to this problem, their mixing characterisation technique using fluorescence intensity imaging with RhB could provide misleading results.

Although fluorescence intensity imaging is commonly used to analyse micromixers, the problems and limitations of the technique have been reported. One of the major limitations is the inability to acquire data close to channel walls due to optical aberrations.[27;51] This problem has in some cases resulted in the failure to validate Computational Fluid Dynamics (CFD) modelling close to the walls due to unreliable data. Burghelea *et al.* reported the rejection of data collected from an area within 10% of the channel diameter from the walls.[51] Strock *et al.* were forced to reject substantial amounts of image data used to validate their modelling simulations. They were limited to only the central 50% of their fluorescence images, due to variations in intensity caused by optical effects at channel walls.[23] The exclusion of substantial amounts of experiment data when validating modelling is of concern, as it can potentially to lead to false 'validated' simulation results. Yamaguchi *et al.* assigned inconsistencies between modelling simulations and fluorescence intensity imaging results to the high levels of noise and optical aberrations from the experimental imaging.[27]

Munson *et al.* were forced to perform a complex correction process to eliminate the effects of the non-uniformity of the excitation light and the collection efficiency, when using fluorescence intensity imaging to evaluate microscale mixing. This process was necessary to enable the intensity profiles collected from their micromixer to be compared.[36] Due to the complexity of this process, it was only carried out on single extracted profiles at selected regions of the images, rather than the entire intensity images, leading to a substantial loss in spatial resolution.

4.1.5.1 Fluorescence quenching

A fluorescence quenching interaction has been used by a few researchers to evaluate microscale mixing.[39;53] Masca *et al.* used the quenching of N-acetyl-L-tryptophanamide (NATA) fluorescence by sodium iodide (NaI). The reaction kinetics of the quenching reaction are much faster than the mixing process, hence its application for evaluating mixing processes.[39] Intensity images were recorded using a CCD camera, however, the images were summed to give a single value for each image rather than using the images to spatially resolve mixing. This may have been necessary due to the limited collection of light due to a poor optical set-up and thus limited the value of the data. Another disadvantage is the time consuming collection of background images recorded in the absence of NATA. This was required to enable baseline and normalisation of the quenching images, and was necessary for each data set at every flow rate and temperature used.

Bessoth *et al.* used the quenching of fluorescein solution by potassium iodide solution (KI) to evaluate the mixing efficiency of a multilamination micromixer.[53]

Single point measurements of fluorescence intensity within the mixer were obtained to quantitatively assess the mixing time. This led to a loss of spatial resolution of quantitative mixing. Qualitative information on the mixer was obtained through visual assessment by eye using fluid streams of fluorescein and rhodamine B.

4.1.5.2 Fluorescent beads

Fluorescent beads have been used by Sritharan *et al.* to trace the streamlines of fluids and visualise the mixing patterns introduced by the micromixer design. The beads were added to one of the inlets to the mixing device to enable the evaluation of micromixing generated by acoustic waves.[38] The addition of beads would be useful to probe mixing by applying micro-particle imaging velocimetry techniques to trace the particles and obtain quantitative information from the streamlines generated by the acoustic waves. The 1 µm diameter particles used in this study are considered by some researchers to be too large to faithfully follow the streamlines of the fluid accurately and have been suggested to disturb the flow at the microscale.[27;54]

4.1.6 Colourimetric imaging techniques

Another frequently used technique to characterise microfluidic mixing strategies is transmitted light microscopy using coloured dyes[10;55-57], pH indicators[45;57-60], and coloured reaction products[55].

The pH indicator phenolphthalein has been used by various researchers to evaluate various micromixer designs, from simple T-shaped mixers,[45] to ultrasonic induced mixing[61] and split-and-recombine designs[55]. Phenolphthalein solution is colourless and transparent below pH 8, however if the pH of the solution is increased above this pH, the solution changes colour to pinkish red.[57] When colourless fluid streams of phenolphthalein solution and sodium hydroxide solution (pH 13) are mixed, the interface between the streams turns red due to the increase in pH of the environment surrounding the phenolphthalein molecules on mixing. The intensity of the red colour has been used to indicate the level of mixing within devices. However, Yaralioglu *et al.* stated that using pH indicators to characterise mixing efficiency could only give an empirical evaluation of mixing performance due to major problems caused by the non-uniform reflection of light from surfaces (depending on material), which distorts the images recorded.

The pH-induced colour change of bromothymol blue (BTB) has been used to indicate the homogeneity of mixing and fluid distributions for a variety of micromixer designs.[59] An inlet fluid stream of green BTB solution at pH 7, was mixed with a fluid stream of a colourless solution at pH 8. When the solutions were fully mixed a blue colour was displayed.[59] Knockmann *et al.* performed this imaging technique in addition to the Villermaux/Dushman reaction (described later) to evaluate mixing.

Various coloured solutions of dyes ranging from rhodamine B dye (creates a pink solution),[10] black ink,[56] Congo Red dye,[56] blue 2,6-dichlorophenolindophenol (DCIP) dye [39] and other unidentified dyes[55;57] have been used to visualise microscale mixing using transmitted light microscopy. The coloured reaction product from the reaction of a transparent stream of a yellowish iron (Fe^{3+}) solution when mixed with a transparent rhodanide (SCN^-) solution to form a deep red complex, was used to quantify the mixing in a split-and-recombine mixer and for comparison with CFD simulations.[55]

Although the imaging of coloured dyes is relatively simple to perform, it is difficult to extract quantitative mixing data as the technique is insufficiently sensitive, provides a limited resolution and is detrimentally affected by light scattering problems.[61;62] Characterising mixing using coloured dyes can give false indication of fully mixed solutions, if layers of unmixed fluids are stratified horizontally rather than vertically in the flow.[57] The technique is suitable for rough evaluations, but cannot provide the quantitative information on mixing required to validate modelling simulations.[61]

4.1.7 Ultraviolet resonance Raman spectroscopy

Mixing efficiency has been evaluated using the band shifts and intensity changes which are characteristic of the protonation of the imidazole ring to imidazolium.[39] This reaction was induced by a rapid decrease in pH upon the addition of citric acid to an imidazole solution. The mixing efficiency was monitored by following the relative intensity changes of distinct bands due to imidazole and imidazolium. Spectra were obtained at different positions within the mixer by point-by-point measurements, hence providing limited spatial resolution. Other problems with the technique included scattered light from surfaces and the requirement of the fabrication of an expensive custom-made micromixer in fused silica. Visualisation of the mixing process using a blue dye was performed in addition. This however displayed misleading mixing results when compared to the Raman data. The visualisation technique showed full mixing was achieved, but this was not evident from the Raman data.

4.1.8 UV absorption

Variations of a parallel competitive reaction, called the Villermaux/Dushman reaction, in which the UV absorption of the by-product can be used to evaluate the mixing performance, has been used by various researchers.[59;62-64] A variation of this reaction was originally used for the characterisation of batch reactors to correlate between mixing quality and mixer design.[62] It has been adapted to use at the microscale to evaluate the mixing performance of new mixer designs.

Mixing quality is determined (i.e. good or bad mixing) using this iodine-iodate reaction (I_2-IO_3^-), in which solutions mixed by various micromixers are spectroscopically analysed to determine the concentrations of I_2 and I_3^-. From these concentrations the efficiency of the mixing process can be assessed. One inlet stream of diluted strong acid (e.g. HCl or H_2SO_4) is mixed with another inlet stream of buffer solution containing KI and KIO_3. The buffer solution contains a weak acid (e.g. H_3BO_3 or CH_3COOH) and strong base (e.g. NaOH or NaAc). Two reactions can occur, depending whether there is fast or slow mixing. The reactions are shown in the following scheme:

$H_2BO_3^- + H^+ \rightleftarrows H_3BO_3$ quasi-instantaneous (i)
$5I^- + IO_3^- + 6H^+ \rightleftarrows 3I_2 + 3H_2O$ very fast (ii)
$I_2 + I^- \rightleftarrows I_3^-$ quasi-instantaneous (iii)

Reaction (i) is the ultra fast neutralisation of the acid which masks the slower redox reaction (ii) of the formation of iodine. If the mixing of fluid streams is relatively slow, this results in the consumption of protons (H^+) by reaction (ii) and hence I_2 is formed. Therefore triiodide ions (I_3^-) as shown in reaction (iii) are formed, which have a strong UV absorption at 352 nm. The amount of light absorbed depends on the mixing performance of the reactant fluids, hence fast mixing results in a weak UV absorption.

The mixed fluid from the outlet of the mixers was sampled in a UV cell and measured with a spectrometer off-line. Currently it is impossible to perform *in situ* sampling or online monitoring. One disadvantage is the lack of discrimination of a good mixing process between homogeneous mixing or fast mixing or a combination of both.[59] Knockmann *et al.* performed additional optical imaging experiments with pH indicator dyes to reveal information on homogeneous flow conditions and any flow distributions.[59] Another drawback of the method is the possibility of surface modifications of channels due to oxidation and reduction.[62] The high concentrations of I^- and IO_3^- can result in detectable amounts of iodine generated by the slower reaction even after complete mixing. Therefore, the time delay between mixing and measuring is crucial and must be minimised.[62] The method can only provide a relative mixing efficiency which is not directly related to mixing time. For example, it can be used to compare between several mixing designs to investigate the best design for mixing, as it will yield results of good or bad mixing for mixing comparisons.[62]

Knockmann *et al.* acknowledged the problems with using this mixing characterisation reaction technique and concluded that significantly more research was required to verify it.

4.1.9 Modelling of microfluidic mixing

Computational modelling techniques can be useful in designing and developing microfluidic mixing systems, although it is important that the generated data is experimentally validated. This view is acknowledged by many researchers who have been developing microscale modelling techniques including finite element modelling, computational fluid dynamics (CFD) and lattice Boltzmann. The majority of papers published on modelling microfluidic mixing are supported by experimental data, albeit, in many cases, the resolution of the data can be poor and is inadequate to accurately verify the models. The poor resolution of some experimental data used can provide broad acceptance criteria which could potentially allow even severely flawed CFD results to be validated. Modelling can be an important tool to explore a vast range of fluid properties and device geometries, as generating experimental data can be expensive in time and resources.

Parameters such as mesh conditions (grid which divides the structure into a number of cells to solve the fluid composition in each), large range of fluid Reynolds numbers and the variability of other fluid properties, have induced computational restraints and imposed limitations on modelling resources accessible to some researchers.[33] Sometimes experimental data is unavailable or difficult to acquire for the full range of modelling data produced. Simplifications including modelling fluids with assumed similar viscosities, symmetrical flow profile, smooth walls, no-slip boundary conditions, constant flow velocity, no flow instabilities and a continuous medium are too readily adopted with modelling packages and the users thereof.[33] Under real experimental situations these assumptions can break down.[27] Some inconsistencies between CFD and experimental results have been assigned to fluid pulsations from the syringe pump, different hydrophilicities of walls for experimental and simulation, noise and optical aberrations from the experimental imaging.[27] Due to computational limitations some published simulations have been limited to 2D calculations rather than 3D.[33] This dimensional issue should be given consideration given that wall effects dominate at the microscale, although vertical lamination may be more of a problem.

It is essential, therefore, that techniques capable of visualising fluid composition with high quantification and spatial resolution are found. This will allow testing of prototype devices, and will provide essential experimental data to guide development of theoretical models and validate computational simulations. Computational fluid dynamics models have proved useful in preliminary mixer designs, but a rigorous understanding of the fundamental principles of microfluidics would lead to the development of better models for complex mixing devices.[55]

In addition, techniques capable of providing quantitative information on micromixers would be extremely valuable in the validation of modelling techniques applied to future micromixer design to eliminate costly trial-and-error techniques and greatly improve design optimization.

4.1.10 Spatial mapping of mixing using FLIM

The results using fluorescence lifetime imaging microscopy (FLIM) reported in this chapter demonstrate a superior approach to the imaging of mixing within microfluidic systems. This technique involves spatially resolving the fluorescence lifetime of a fluorescent dye, rather than the intensity, and overcomes many of the aforementioned problems of intensity-based methods because the lifetime is independent of the number of fluorescing molecules. Before the publication of the data from this chapter in 2005, the use of FLIM had been restricted to the imaging of biological systems and these papers are on non-flowing systems.[65-67] This thesis is the first study to demonstrate that FLIM enables spatially-resolved quantification of fluid mixing in microfluidic devices. Following this publication, numerous papers exploiting FLIM techniques to spatial map mixing within microfluidic devices have been published.

4.1.10.1 Subsequent applications of FLIM techniques in microfluidics

Benninger *et al.* reported mixing in microfluidic devices using two different time-resolved imaging techniques.[68] A fluorescence anisotropy technique produced images of mixing between inlet solutions of fluorescein in pure water and fluorescein in a glycerol/water mixture (50/50 v/v) within a microfluidic device. The anisotropy technique allows the acquisition of an image of the fluorophore rotational mobility within solvents of differing viscosities. From these images, quantitative mixing profiles were extracted. The disadvantage of this technique of mapping the rotational correlation time is the necessary recording of two intensity-gated images with fluorescence collected parallel and perpendicular to the excitation polarization. This, along with requiring a high signal to noise ratio, resulted in acquisition times of several minutes for each image.[68] The second technique reported real-time fluid mixing using high-speed fluorescence lifetime imaging recorded at 12.3 Hz using a different fluorophore (DASPI), which displayed a fluorescent lifetime directly dependent on the local solvent viscosity.[68] FLIM images of DASPI in pure water and a glycerol/water mixture was acquired from two time-gated images. No quantatitive data was extracted from the high-speed FLIM images, most likely due to a low signal to noise ratio.

Redford *et al.* used fluorescence lifetime imaging to provide information on the mixing processes and efficiency in a continuous-flow turbulent microfluidic reactor.[24] Fluorescent lifetime images of the mixing of fluorescein and iodide solutions within the reactor were recorded. The excited state of fluorescein is effectively quenched by iodide, which resulted in the decrease of the fluorescence lifetime of fluorescein from 4.05 ns to almost zero. Fluorescence lifetime imaging was able to reveal detailed information on the mixing processes and turbulence on the molecular scale from the response of the fluorescein probe to the surrounding molecular fluid environment.[24]

Elder *et al.* demonstrated the application of LEDs as inexpensive alternative excitation sources for frequency-domain FLIM using a microfluidic mixer to combine fluid streams of a fluorophore solution (Rhodamine 6G in KCl solution) and a quencher solution (Rhodamine 6G in KI solution).[69] This work was extended in a second paper published several months later, which focused entirely on diffusional-based mixing within microchannels.[70] Frequency-domain FLIM could be more readily implemented in imaging within microfluidic devices due to the relatively inexpensive LEDs employed for the excitation of the fluorophores. However, a major drawback was the extended time necessary to acquire information on samples with multiple fluorescence lifetimes, as this will require different modulation frequencies of the LED intensity to resolve the separate lifetimes. Therefore, the technique was only really suitable to simple single exponential decays, as is displayed by the fluorophore quenching reaction. Elder *et al.* (June 2006) highlighted the problems with using fluorescence intensity imaging for investigating mixing in microfluidic devices by comparing the results with FLIM images. Strong variations in the intensity images were considered to be due to absorption of excitation light and re-absorption of emitted fluorescence light. In addition, this problem was exacerbated by optical distortions when imaging deep into the channel. The authors draw the conclusion that it would be extremely complex to extract any quantitative data from the intensity images collected.

4.1.10.2 Introduction to the FLIM technique

In this study the fluorescent probe 1,8-anilinonaphthalene sulfonate (ANS) was selected to investigate microfluidic mixing using FLIM, as ANS displays a fluorescence lifetime which is extremely sensitive to the composition of water-methanol mixtures, showing a near-linear variation from 240 ps in pure water to 6 ns in pure methanol.[71] It will be demonstrated using ANS that FLIM enables spatially-resolved quantification of fluid mixing in microfluidic devices.

4.2 Experimental Details

4.2.1 Solution preparation

All measurements were made with the ammonium salt of 1,8-anilinonaphthalene sulfonate (ANS) obtained from Fluka and used as received. Solutions of ANS (*ca.* 1×10^{-3}M) in pure methanol and a water-methanol mixture (1:1 molar ratio, which corresponds to 30.8% water v/v) were prepared using HPLC grade methanol and water (Fisher Scientific), used as received. The solutions of ANS were stored in the dark, and the lifetime of ANS fluorescence at room temperature was used as a routine check of sample purity after storage. No fluorescence emission, at the wavelengths employed, could be detected from the solvents under the instrumental conditions used.

4.2.2 Microfluidic mixing system

The microfluidic flow cell was fabricated from Perspex, with a 'T' shaped channel milled out to a depth of 0.2 mm, using a 0.4 mm diameter end mill (Drill Service Ltd). The dimensions of the milled ‘T’ channels are illustrated in Figure 4.1.

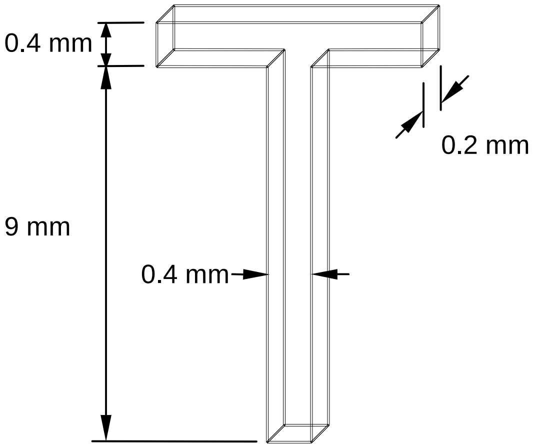

Figure 4.1: Dimensions of the ‘T’ milled into the Perspex block.

The three inlet/outlet holes were drilled 1.6 mm in diameter and fitted with polypropylene tubing (outer diameter 1.65 mm), cut from dispensing tips (EFD Inc). Araldite glue was used to seal the join between the polypropylene tubing in the drilled holes if any leaking occurred from a poor fit. Silicone tubing (inner diameter 1.0 mm, Altec Products Ltd) was used to attached the polypropylene tubing to syringes (3 ml, plastic Luer-lock syringes, BD), fitted with uncut polypropylene dispensing tips (EFD Inc.). The cell was sealed by gluing (Norland Optical Adhesive No. 61) a coverglass over the channels. The glue was applied around the perimeter of the milled ‘T’ shape using a pressure-dispensing system (EFD Inc.) to precisely control the amount of glue dispensed. The glue was held within a UV-resistant syringe fitted with a micro-needle and piston (syringe, needle and piston from EFD Inc.). The syringe, with piston, was attached to tubing, through which pressurized air was forced to move the syringe piston. The air pressure was varied to change the piston force and hence control the amount of glue dispensed. The coverslip was then lowered onto the glue and cured under UV light. The precision of the gluing enabled minute amounts of glue to be dispensed around the microchannels and helped prevented glue, from flowing into the microchannels and causing any blockage problems. A photograph of a fully assembled and several un-assembled mixers, is displayed in Figure 4.2.

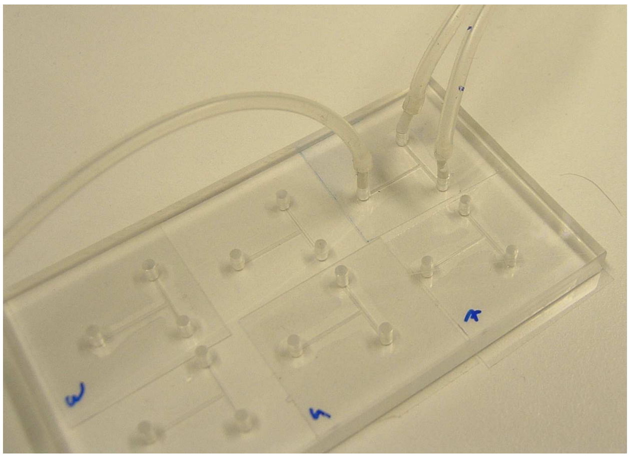

Figure 4.2: Series of six milled and drilled T-shaped mixers on a Perspex block. Three of the T-mixers are sealed with glued-on coverslips. The mixer at the top is fully assembled, fitted with polypropylene tubing into the drilled holes, and attached to silicone tubing leading to the syringes.

Solutions of ANS in pure methanol and a water-methanol mixture (30.8% water v/v) were pumped into the flow cell, meeting head-on at the top of a T-junction, as illustrated in the annotated photograph of the assembled flow cell (Figure 4.3). The flow of fluids from the syringes was controlled by a syringe pump (Univentor 802, Univentor Ltd).

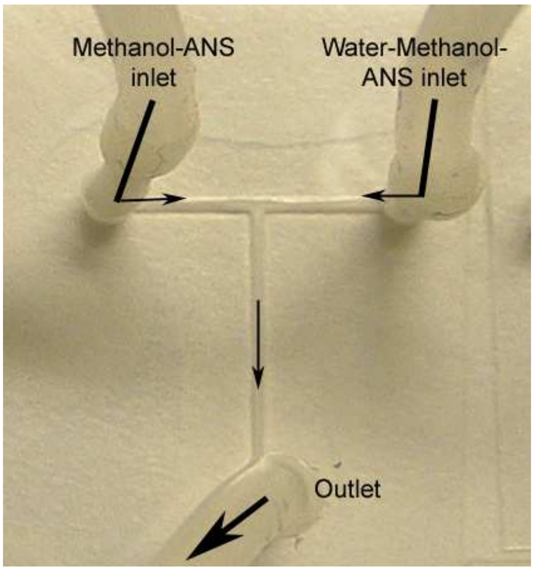

Figure 4.3: Annotated photograph of the T-shaped micromixer with tubing attached, leading to the syringes. The arrows indicate the inlet flows of methanol-ANS and water-methanol-ANS solutions, and outlet flow.

4.2.3 Fluorescence lifetime imaging (FLIM)

The flow cell was clamped to the microscope stage to prevent movement during recording. The ANS solutions were pumped through the device, to allow the flow to develop and ensure no leakage problems before recording the mixing. Excitation laser radiation of wavelength 400 nm was reflected from a dichroic filter (DM430, Nikon) and focused into the flow cell using either 20× (PA, NA=0.75, Nikon) or 100× (Ph3, NA=1.3, oil immersion, Nikon) objectives. The light was focused whilst the solutions were flowing through the device, using the CCD camera in a constant intensity imaging mode, with the time-gate set at the peak of the decay to obtain a peak intensity of between 3000 and 4000 counts. The resultant fluorescence collected was passed through a 515-555 nm barrier filter (Nikon) and recorded using a 600 ps gate width. The images were the average of 5 separate exposures, and were recorded in steps of 500 ps over a 23 ns range. The integration time for each image was 0.1 ms, with 0.05 ms readout time, giving a total acquisition time of approximately 35 s. The peak of the fluorescence intensity was found in the fourth image of the image series. To ensure that the instrument response did not interfere with the fitting, the first five images were not used for analysis. The sixth image, which was 1 ns after the peak, and the subsequent images were analyzed, allowing a decay curve to be constructed for each pixel. Pixels with low counts in the first analyzed image (typically 700 counts) were removed at this stage. Each of these curves was then fitted to a single exponential decay. A lifetime map was produced by assigning a colour on a 16-bit pseudocolour scale to each of the fitted lifetimes, and these were displayed over a range of 2-6.8 ns.

4.2.4 Time-resolved fluorescence spectroscopy (TCSPC)

The solvent dependence of the fluorescence lifetimes of ANS in methanol-water mixtures was determined by time-correlated single photon counting. Fluorescence decays were recorded on a range of solutions of ANS in water-methanol mixtures, with the concentration of water varying from 0 to 30.8 % v/v. The aerated solutions were contained in a 1 cm pathlength fused silica cuvette (10 x 10mm inside dimensions, Optiglass Ltd). Fluorescence was excited at 400 nm and decay curves were recorded at an emission wavelength of 520 nm. Fluorescence decay curves were recorded into 4096 channels and accumulated to 10,000 counts in the peak channel on a time range of 20 ns. The fluorescence decay curves were analysed by tail-fitting (i.e. without convolution with the instrument response function), from ~1 ns after the peak of the decay, to correspond to the conditions used to fit the FLIM decays. Discrete decay analysis was performed with the F900 software package (Edinburgh Instruments).

4.3 *Results and Discussion*

4.3.1 Time-resolved fluorescence spectroscopy of ANS

ANS displayed a single exponential decay at all compositions of water and methanol, making it an ideal, unambiguous probe of solvent composition. The residuals for ANS in pure methanol and a water-methanol mixture (30.8% water v/v) are displayed in Figure 4.4, and are random across the whole decay, illustrating the satisfactory single exponential fit to the fluorescence decays.

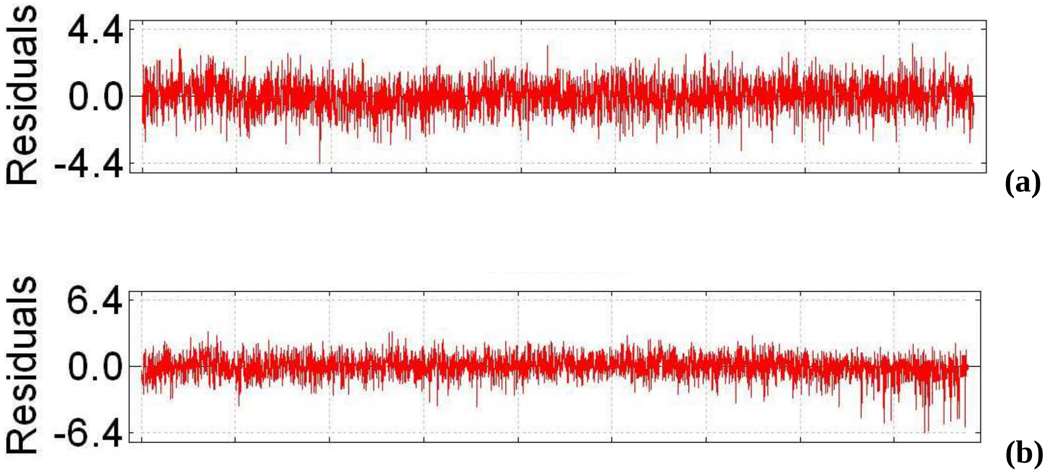

Figure 4.4: The residuals from fitting a single lifetime to fluorescence decay for **(a)** pure methanol and **(b)** 30.8 % water v/v in a water-methanol mixture (corresponding to a 1:1 molar ratio).

The individual fluorescence decays recorded by TCSPC have been combined and displayed in Figure 4.5. This shows the lifetimes decreasing as the percentage composition of water in the water-methanol mixtures increases.

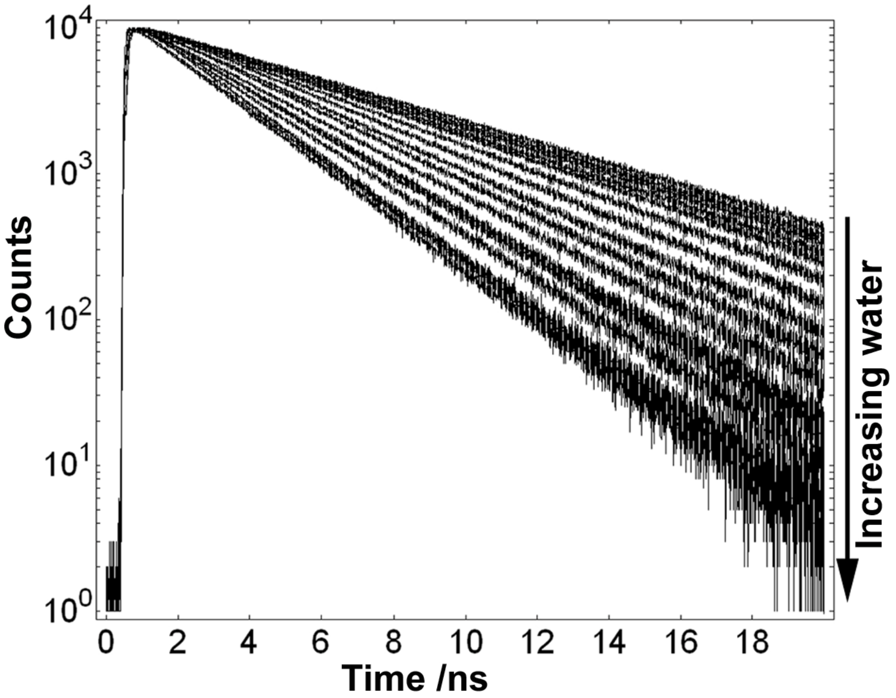

Figure 4.5: TCSPC data for solutions of ANS in methanol-water mixtures. Starting from the top curve, the concentration of water (% v/v) in the solutions is 0, 2, 4, 6, 8, 10, 13, 16, 18, 20, 23, 24, 26, 28, 30, 30.8 %.

The fluorescence lifetimes and reduced χ^2 values for ANS in the water-methanol solutions is presented in Table 4.2. The reduced χ^2 values are all considerably less than 1.1, which demonstrates an excellent fit to a single exponential decay function for all the mixtures. The lifetime of ANS changes from 5.97 ns in pure methanol to 2.36 ns in 30.8 % water v/v in a water-methanol mixture.

% water in water-methanol mixture	τ /ns	χ^2
0	5.97	1.08
2	5.73	1.04
4	5.57	1.05
6	5.34	1.02
8	5.09	1.09
10	4.72	1.03
13	4.29	1.05
16	3.93	1.03
18	3.61	1.02
20	3.36	1.05
23	3.03	1.05
24	2.95	1.03
26	2.74	1.01
28	2.46	1.06
30	2.42	1.04
30.8	2.36	1.08

Table 4.2: Fluorescence lifetimes (τ) of ANS as a function of the percentage of water in water-methanol mixtures. The goodness-of–fit parameter, χ^2, of the fitted mono-exponential function is also shown.

Figure 4.6 quantifies the dependence of the lifetime of ANS upon the water/methanol composition. The equation $Y = 5.97258-0.09267\ X-0.00382\ X^2+9.82168E-5\ X^3$, where Y is the lifetime in ns, and X is the concentration of water in the water-methanol mixture (% v/v) gave a good fit to the data. Values from Figure 4.6 have been used as a calibration between lifetime and composition, by re-plotting the data with the axes switched (Figure 4.7). The composition-lifetime calibration data fitted well to the equation $Y = 84.02401-35.36578\ X+6.52602X^2-0.49581X^3$, where Y is the concentration of water in the water-methanol mixture (% v/v) and X is the lifetime in ns. This equation was used in conjunction with the FLIM images, to convert the lifetime of each pixel to the percentage composition of water, to produce composition maps.

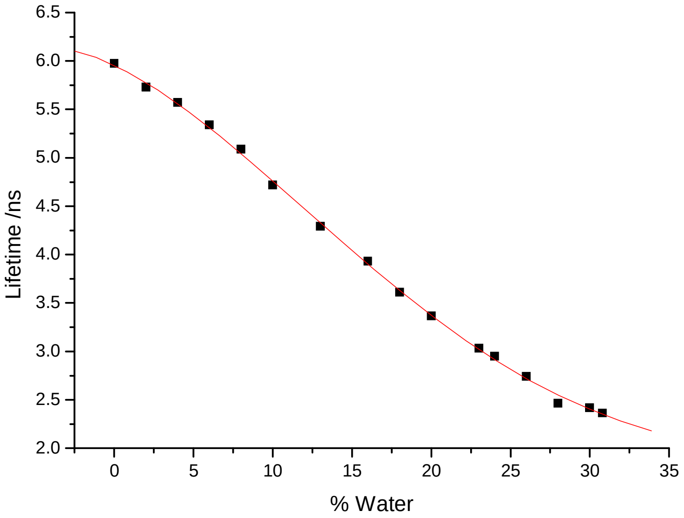

Figure 4.6: Graph showing the dependence of ANS fluorescence lifetime upon the percentage composition of water in water-methanol mixtures.

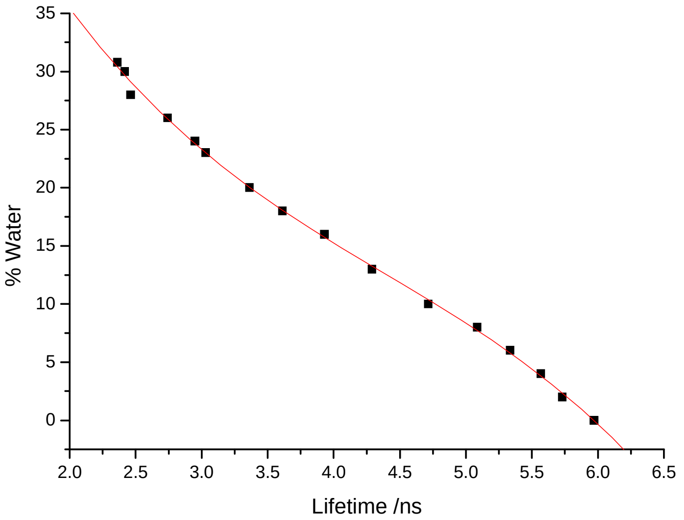

Figure 4.7: Calibration curve showing the relationship between the percentage composition of water in water-methanol mixtures and the lifetime.

4.3.1.1 Effect of the solution refractive index

The Strickler-Berg equation states that the inverse of the fluorescence lifetime scales approximately with the square of the refractive index of the solvent. However, the change in the refractive index of the solvents from pure methanol to the water-methanol mixture is too small to have a significant effect on the radiative lifetime of ANS, hence the refractive index change has a minimal effect on the overall lifetime. (The refractive index of water at 293 K is 1.333 and that of methanol is 1.328). The overall lifetime change displayed by ANS in water-methanol mixtures can be attributed to the significant change in the non-radiative lifetimes resulting from solvent interactions.

4.3.2 Fluorescence lifetime imaging of microfluidic mixing

Fluorescence lifetime imaging microscopy has been used to quantitatively map the mixing of ANS in a pure methanol and a water-methanol mixture within a microfluidic T-shaped mixer. The flow channels had a depth of 200 μm and width of 400 μm, and the inlet flow rates were varied from 10-75 μL/min. These dimensions and inlet flow rates correspond to Reynolds numbers < 10, such that the fluids are in the laminar flow regime.[72]

4.3.2.1 Comparison of FLIM with intensity-based imaging

The effectiveness of the time-resolved technique is demonstrated in Figure 4.8, which compares the intensity and lifetime images for two regions of the flow cell during a typical experiment. The intensity and FLIM images, which are displayed using the same pseudocolour scale, are noticeably different. The intensity images (Figure 4.8a) show large, irregular variations in intensity across the field of view, with the highest intensity regions located near the input of the solution of ANS in methanol. The FLIM images give a clear and unambiguous picture of the liquid composition (Figure 4.8b). These images show smooth transitions from long to short lifetime (left to right), across a clearly defined mixing region. By using the calibration curve in Figure 4.7, the composition at each point in the FLIM image can be directly read off. The intensity image was constructed by summing the lifetime images, which allows a direct comparison between the time-resolved and intensity-based methods. In principle, there should be a clear correlation between the intensity images and the lifetime images; the longer the fluorescence lifetime, the higher the quantum yield and hence the higher the fluorescence intensity (given that the ANS concentration is constant). In practice, however, no such correlation is apparent and it is clear that the intensity-based images are strongly distorted by variation of the illuminating field, the collection efficiency and the other variables previously mentioned. The microfluidic flow cell used in this study is of a simple design, and it is likely that intensity-based imaging will be even more prone to optical artefacts in complex devices. FLIM, on the other hand, faithfully reports the fluid composition, as the lifetime is governed solely by the solvent environment of the ANS probe, and is immune to other undesirable effects.

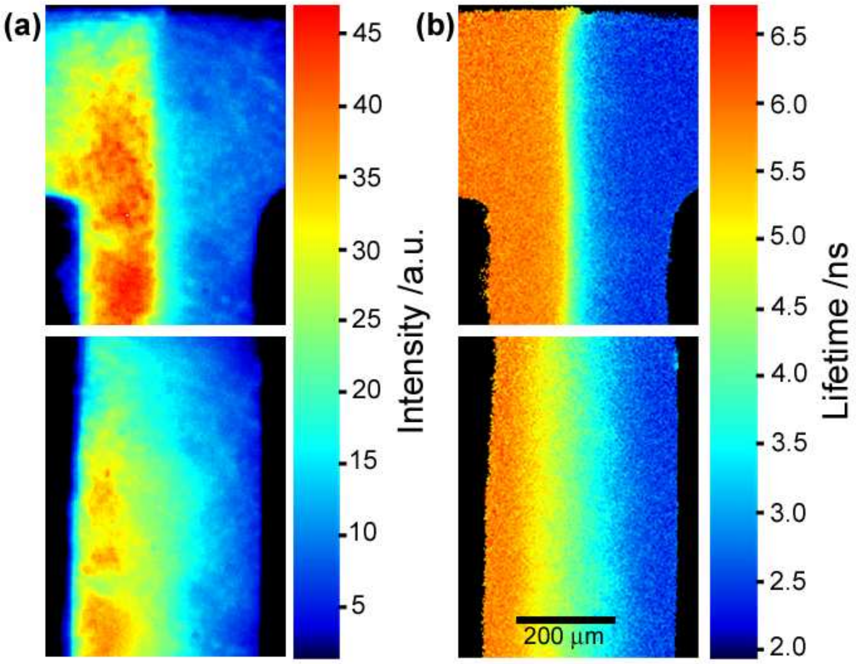

Figure 4.8: Comparison of fluorescence intensity images (a) and FLIM images (b) for the mixing of solutions of ANS in pure methanol and ANS in a water/methanol mixture (70:30 v/v), using the arrangement shown in Figure 4.3. The flow rate of fluids in both inlets was 50 µL/min.

4.3.2.2 Microfluidic mixing maps

The FLIM technique has been used to monitor mixing as a function of flow rate and flow distance (Figure 4.9). The compositional variation observed in Figure 4.9 is indicative of two fluids under laminar flow, as expected. One feature of the resultant images is how little mixing occurs in the region where the two input streams meet. Despite being forced together, there is no sign of turbulent mixing. The input streams are well behaved, with no fluctuations in the position of the boundary between them. Instead, the two streams stay completely separate, except for a narrow mixing region due to diffusion. The overall trend is for the mixing region to broaden as the flow rate decreases, and as the fluids move further downstream, as expected for diffusional mixing. For the fastest flow rate (75 μL/min), regions that are identical in composition to the input streams persist, even after travelling 1 cm down the channel. In contrast, the two fluids have completely mixed at this distance downstream at the slowest flow rate (10 μL/min).

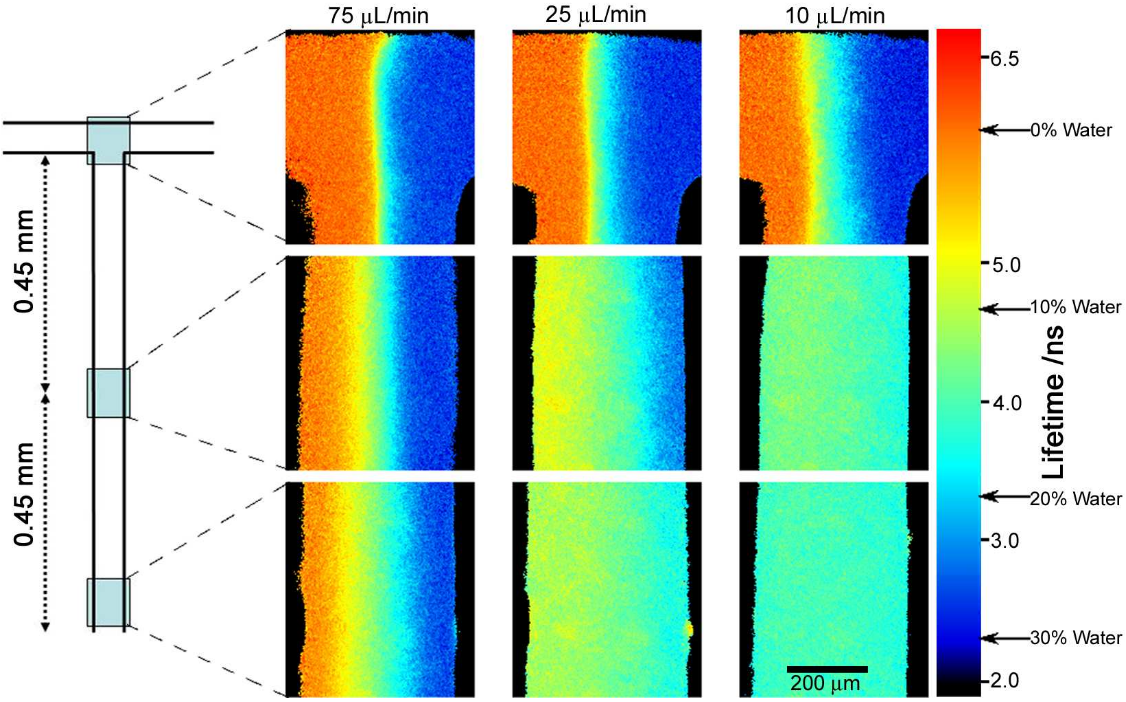

Figure 4.9: FLIM images for the mixing of solutions of ANS in pure methanol and ANS in a water/methanol mixture (70:30 v/v), showing the spatial dependence of lifetime upon the flow rate and the position within the flow cell. Images were acquired at three positions in the flow cell, and at three flow rates, as indicated in the schematic diagram.

4.3.2.3 Quantification of mixing

FLIM allows the monitoring of mixing with high spatial resolution (Figures 4.10a and b), accurately measuring small changes in the fluid composition in sub-picolitre interrogation volumes. The technique is sensitive enough to reliably detect a *ca.* 2% change in the volume fraction (Figure 4.10c); this is equivalent to a lifetime change of *ca.* 250 ps, which is a measurement limit set by the temporal width of the detection windows. The compositional resolution could be improved by increasing the time-resolution of fluorescence detection, using photon counting methods. This method is equally applicable to diffusional mixing (the fluorescence lifetime responds to the net diffusion of water molecules across the flow boundary) and mixing by mass transport of fluid, and is, therefore, generally applicable to the evaluation of all types of micromixers. The quantitative spatial profiles of fluid composition that can be generated by FLIM (Figures 4.10c and d) are particularly valuable for supporting and guiding theoretical models of fluid flow in microfluidic systems.

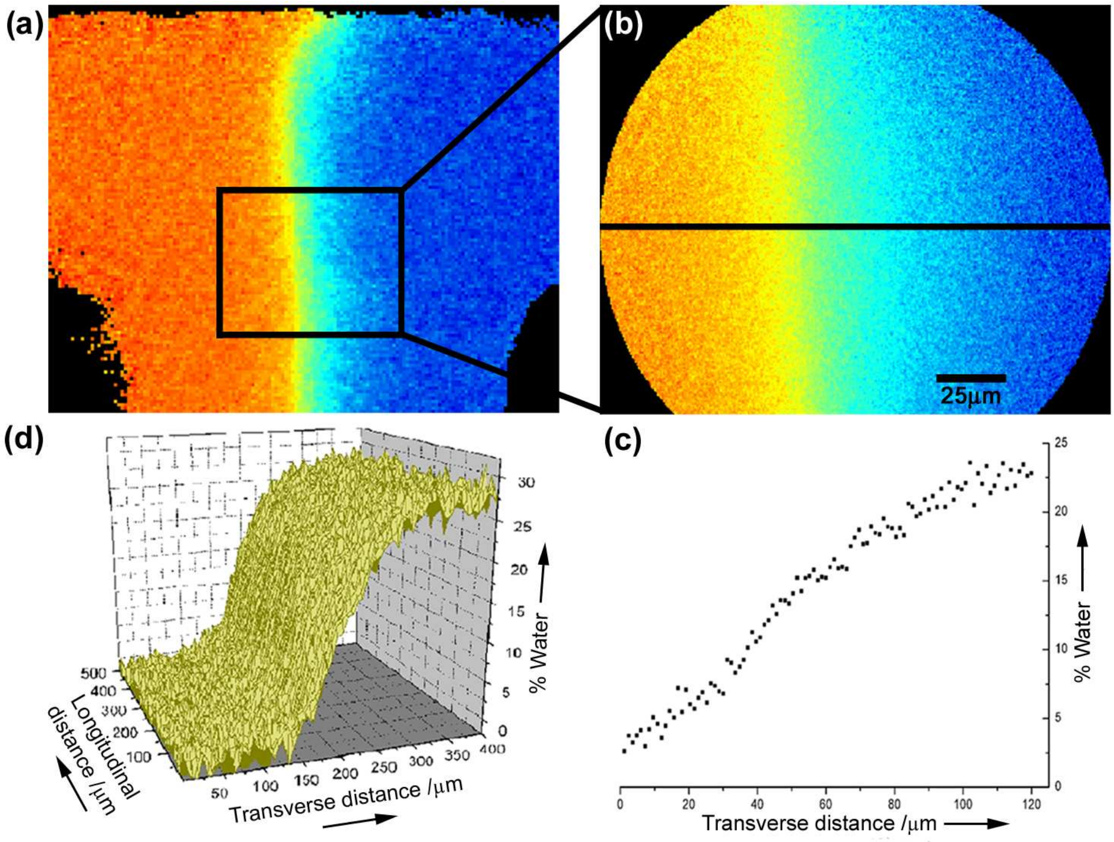

Figure 4.10: Quantification of mixing using FLIM. **(a)** FLIM image of the mixing of methanol and water/methanol using a 20× objective. The flow rate was 75µl/min. **(b)** Expanded image of the same mixing region using a 100× objective. **(c)** Composition profile along the cross section indicated in Figure 4.10b. **(d)** Representation of the lifetime data in Figure 4.10a as a composition surface. Composition values were calculated using the calibration curve in Figure 4.7.

4.3.2.4 Composition profiles

Composition profiles have been extracted from the FLIM images recorded at the confluence zone (beginning of the mixing channel) and before the fluids passed into the outlet tubing (end of the mixing channel), for flow rates 10, 25, 50 and 75 µL/min (Figure 4.11). At the confluence, the composition profiles show a quasi-sigmoidal shape, displayed by the red plots for each flow rate in Figure 4.11. At the highest flow rate of 75 µL/min (Figure 4.11d), the profile at the beginning of the mixing channel shows a sharp composition gradient between the water-methanol stream and the pure methanol stream, with horizontal regions at the channel walls, identifying the different compositions of the inlet fluids. As the flow rate decreases from 75 to 10 µL/min, the profile shapes of the fluids at the confluence changes gradually. The sharp difference between the inlet fluid streams decreases and the overall profile becomes less sigmoidal-shaped. This is most noticeable in the profile of the water-methanol fluid stream, which at 10 µL/min (Figure 4.11a) displays a near-linear gradient (represented by the red plot in Figure 4.11a). As the fluids progress through the mixing channel, the composition profiles change from a sigmoidal to a linear profile at the end of the mixing channel, for all the flow rates.

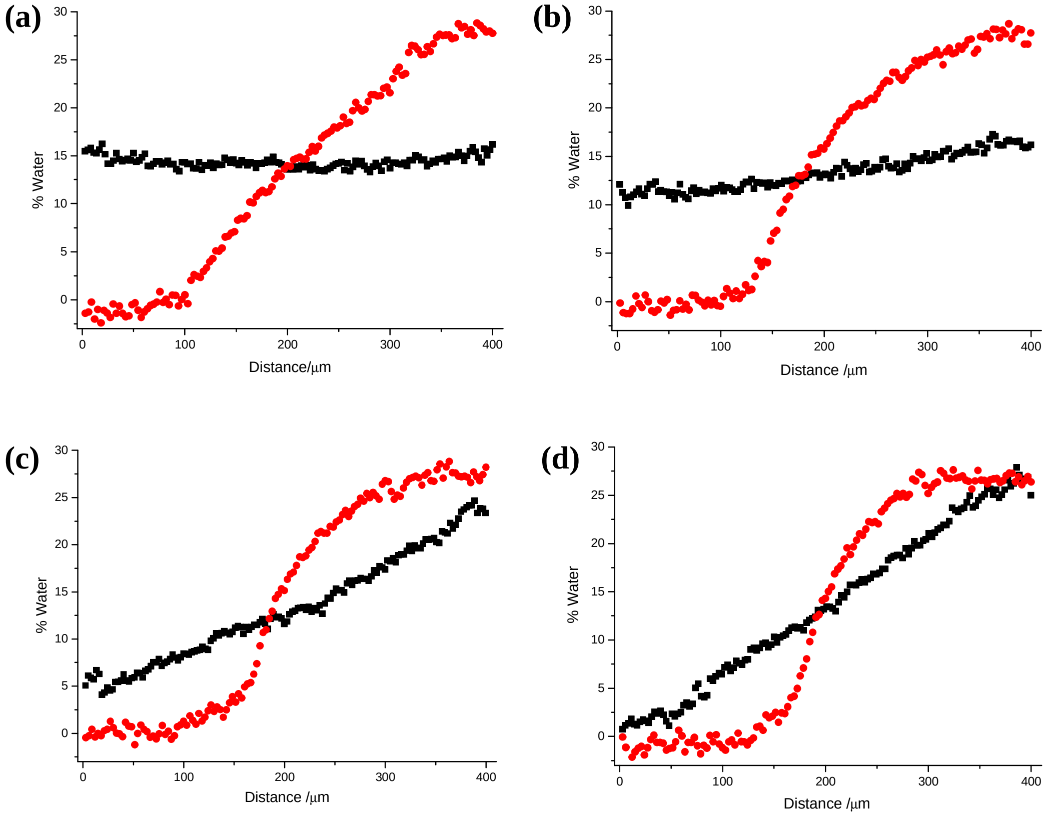

Figure 4.11: Composition profiles showing the percentage composition of water across the beginning of mixing channel (red circles) and across the end of mixing channel (black squares) for flow rates (a) 10 µL/min, (b) 25 µL/min, (c) 50 µL/min, and (d) 75 µL/min.

Table 4.3 provides the Reynolds and Péclet numbers for the inlet fluid streams at each flow rate represented in Figure 4.11 to quantify the limited extent of the mixing by diffusion. The high Péclet numbers show that the convection of the fluid flows through the channels is significantly greater than the lateral diffusion across the channels, hence mixing is limited.

Flow rate (µL/min)		Pure methanol	Water-methanol
10	Reynolds number	0.8	0.3
25		1.9	0.7
50		3.8	1.4
75		5.6	2.2
10	Peclet number	250	440
25		630	1100
50		1300	2200
75		1900	3300

Table 4.3: Reynolds and Péclet numbers for the inlet fluid streams at each flow rate represented in Figure 4.11.

Figure 4.12 shows the composition profiles across the end of the mixing channel for all the flow rates, to compare and evaluate the degree of mixing. All the profiles are linear, with the gradient of each profile decreasing from 75 µL/min to 10 µL/min. At 10 µL/min the profile is flat, i.e. the gradient is essentially zero, denoting that the fluids are completely mixed.

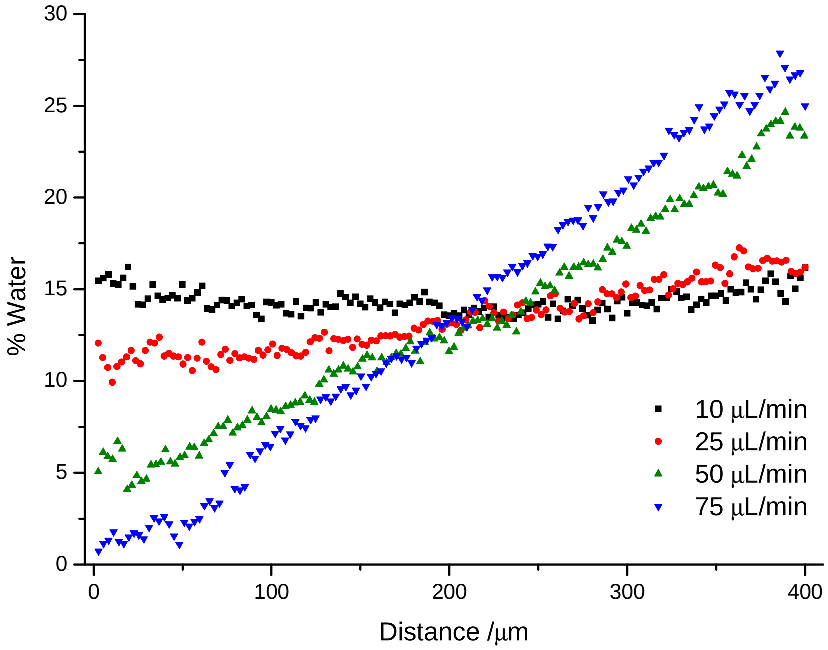

Figure 4.12: Composition profiles showing the percentage composition of water across the end of the mixing channel for flow rates 10 μL/min (black squares), 25 μL/min (red circles), 50 μL/min (green triangles), and 75 μL/min (blue triangles).

4.3.2.5 Fluorescence intensity movie

A fluorescence intensity movie was recorded of the two fluid streams at the confluence of the T-mixer, with an inlet flow rate of 25 μL/min. The movie can be viewed from the supporting information provided on a separate CD. ANS was present in the pure methanol inlet flow (10^{-3} M), but was absent from the methanol-water inlet flow. This set-up was used to image only one inlet flow, to check if flow fluctuations were present as fluctuations can induce mixing effects.[73;74] The movie showed that the inlet flows of the microfluidic system were stable and well-behaved. Images were continually recorded using the same system described for FLIM and were collected at the peak of the fluorescence decay. The integration time for each image was 100ms, with 50 ms readout time, giving an acquisition rate of approximately 7 frames/s. The movie was created using Microsoft Video 1 compression (75% quality). The time-gated intensity images recorded, for producing

FLIM images, were visually monitored over the entire fluorescence decay to ensure no flow fluctuations were present. If any air bubbles flowed through the mixing channel, the recording was repeated.

A single intensity image from the movie is displayed in Figure 4.13, this image is representative of all the frames collected. The flow showed little deviation from this image template. The left inlet flow, represented by blue, shows the ANS-methanol inlet flow. The right inlet flow, although present, is not displayed in the image due to the absence of ANS from the water-methanol mixture. Therefore it does not exhibit fluorescence and cannot be detected.

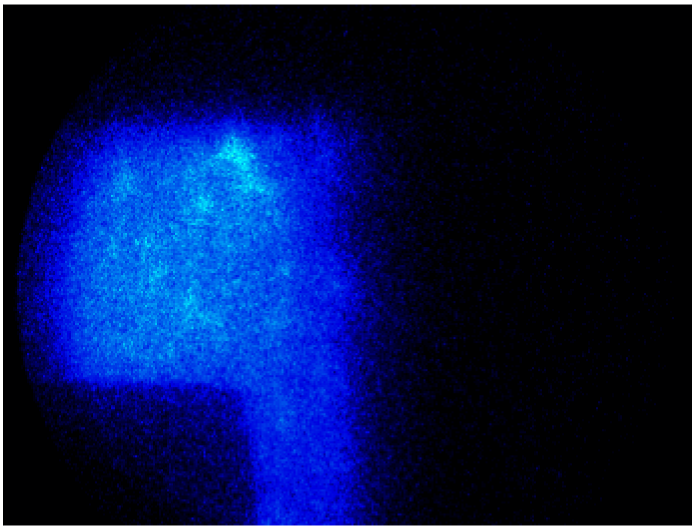

Figure 4.13: A single image showing a typical frame from the fluorescence intensity movie recorded at the confluence of the T-shaped mixer.

4.4 Conclusion

The results presented demonstrate that widefield FLIM can directly measure the two-dimensional mixing of fluids in microfluidic systems with a level of quantification that was not available from other methods at the publication time of this data. It has been shown that intensity-based techniques such as confocal microscopy[23] and optical coherence tomography[75] can provide three-dimensional imaging of microfluidic flows. This is important when the variations in fluid composition are along the optical axis, since these cannot be resolved by intensity-based widefield methods.[75] The FLIM approach can be extended to full three-dimensional imaging by using confocal or multiphoton excitation, while still maintaining the attendant benefits of time-resolved detection that have been established here. In this version of the technique, the tightly focused excitation laser beam is rastered across the sample and the fluorescence decay is acquired point-by-point, using time-correlated single photon counting. The use of multiphoton excitation would also enhance imaging penetration through strongly absorbing or scattering fluids or structures.

The mixed solvent system used in the present work, in conjunction with the ANS probe, was devised purely as a measurement tool for the generic study of micromixing, and was not intended to relate to any specific applications of lab-on-a-chip systems. This approach is, however, generally applicable to any solvent system, as long as there is a change in molecular environment upon mixing that results in variation in the fluorescence lifetime of an appropriate probe. For example, mixing of aqueous solutions could be studied by using streams of different pH that incorporate a pH-sensitive dye, such as a seminaphthorhodafluor (SNARF) probe. Alternatively, streams containing different concentrations of a collisional quencher, such as iodide, can be used, as shown by Elder *et al.* and Redford *et al.*[24;70] In view of the flexibility of this approach, it was anticipated that FLIM would become an essential tool in the design, modelling and evaluation of microfluidic systems. Since the publication of this data, four further papers have been published using FLIM to probe microfluidic mixing.[24;68-70] The results from this chapter have been used by the National Physical Laboratory to evaluate commercial CFD codes used for microfluidic applications. A copy of this manuscript, which has been submitted to the journal *Microfluidics and Nanofluidics,* is presented in the Appendix. The paper demonstrates the excellent agreement achievable between the FLIM results and simulated results.

Chapter 5

Evaluation of geometric parameters of commercial micromixers

5.1 Introduction

There have been numerous publications covering a variety of unique micromixer designs and their subsequent characterisation to evaluate the mixing efficiency. The microfluidic flow cell used in the previous chapter to quantify mixing between fluid streams was an extremely simple design. The device was fabricated to optimise the excitation and collection of fluorescence emitted, by imaging through a glass microscope coverslip (thickness ~ 0.16 mm), which is typically used for microscopy and imaging studies. The device was practical to assess the feasibility of the FLIM technique for the new application of quantitatively mapping mixing within microfluidic devices. However, most microfluidic devices are of a more complex design and the majority are not manufactured to allow optical transparency over a range of wavelengths and interrogation with advanced fluorescence imaging techniques. In this chapter a range of commercial micromixers, produced by Epigem Ltd, have been analysed and evaluated using the FLIM system.

The polymeric micromixers produced by Epigem are passive laminar flow mixers, designed to improve the efficiency of diffusion-based mixing at the microscale. Information on the manufacturing process and device materials were not disclosed by the company. The effect of the inlet channel angle, channel dimensions, chambers and serpentine channel designs have been assessed using the FLIM technique. In addition, two unique micromixers with more intricate designs have been assessed. The first of these mixers has sharp asymmetric curves in the vertical mixing channel walls and the second has vertical columns or obstacles fabricated in the mixing channel. The designs were selected by Lab 901 Ltd due to their interest in enhancing the mixing of fluid streams, but also for the ease of future fabrication of cheap disposal polymeric microfluidic devices.

Prior to this work, few studies had quantitatively evaluated such mixing designs and parameters. The following sections review the literature to date in this area.

5.1.1 Effects of bends in microchannels on mixing

Mengeaud *et al.* investigated the effects of 90^o bends in microchannels or a ‘zigzag’ geometry, on the mixing efficiency between two fluid streams using finite element simulations.[33] They concluded that a critical Re number of 80 was required before the 90^o bend had a positive effect on the mixing efficiency, Re numbers below 80 had no effect on the mixing. The increased mixing due to the zigzag geometry was determined to be due to inertial effects, which led to a pressure gradient inversion after each angle turn. This recirculation forces the transverse component of the velocity spread species from the mixing interface to the walls. Therefore, for high flow rates, mixing was induced by a combination of laminar recirculation and diffusional processes. They found an optimum geometry which could increase the effect of laminar flow recirculation generated at each angle, induced by the zigzag design, at high flow rates. However, all the simulations were performed only in 2D. The authors explained that modelling of 3D channels would significantly dampen the recirculations due to the walls at the top and bottom of the channels. Fluorescence intensity profiles over a range of flow rates were recorded in an attempt to validate the simulations. However, the researchers could only validate their modelling results for low Re numbers (0.1 to 9) as a result of problems at the inlets of their micromixer, which prevented high flow rates being achieved. In addition, it was not ideal to use experimental data from channels with dimensions of 100 µm wide by 48 µm deep to validate 2D modelling, which had assumed infinitely deep channels, especially as the mixing effect will be greatly dampened by the channel walls. Indeed, the authors confess that for real 3D experiments a critical Re number of ~7 is probably more realistic, an order of magnitude lower than the simulated result. Mixing deviations observed in the fluorescence profiles were assumed to result from defaults in the channel structure. The mixing effect will be reduced in channels of smaller cross-section due to the effect of the larger surface to volume ratio.

Yamaguchi *et al.* investigated the enhancement of mixing based on a serpentine microchannel design with 180° bends. The effects were simulated with CFD, however, fluorescence intensity-based confocal imaging was used to validate the initial simulations of the basic mixing principles before extrapolating the model over a wider range of variables. The confocal imaging was essential to enable vertical optical sections through the microchannels to be obtained. There was good agreement between experimental confocal images of the interfaces and the CFD images.[27] The enhancement of mixing is due to inertial forces acting on the liquid flowing round the turns; this distorts the normally vertical interface between the fluids, and increases the surface area of the interface to increase the molecular diffusion. At the fluid velocities and Re numbers used in this experiment, after the first turn the interface is distorted from a vertical interface (I shaped) to a curved interface (> shaped), which was calculated to increase the surface area by ~50 %.[27] Following the second turn the inertial forces were now exerted in the opposite direction, which causes the curved interface (> shaped) back to the initial vertical interface (I shaped).[27] If much higher flow rates were used, the interface did not recover to the vertical form and was permanently wave-shaped.[27] This increased the interfacial area and increased mixing by molecular diffusion. However, the researchers found it difficult to achieve such high Re numbers in their devices without significant pressure-drops and problems with backpressure.[27] The interface was only noticeable in the first few turns and then disappeared as the fluids mixed. The distortion of the interface was more pronounced with fluids of different densities and was less affected by viscosity differences.[27] Secondary flow vortices could be produced as an effect of the serpentine turns with Re numbers as low as 25.[27]

5.1.2 Effects of obstacles in microchannels on mixing

Wang *et al.* simulated, using CFD, the effect of obstacles or vertical columns within microchannels to improve mixing by creating lateral mass transport, thereby stirring the fluid.[76] Various arrangements of one to eight cylindrical obstacles of 60 µm diameter within a channel of 300 µm wide by 100 µm deep were simulated. A Y-shaped mixer with a 60° angle between the two inlet channels of width 200 µm was used to converge the inlet fluid streams. They predicted from their CFD simulations that increasing the number of obstacles increased the mixing efficiency and that an asymmetric arrangement of obstacles was more effective. Again, due to limited computational resources, the modelling was performed only in 2D. Obstacles placed in microchannels cannot generate eddies or turbulence due to the low Re numbers of the flow.[76] The authors postulated that the increased mixing was due to the disturbance of the parabolic velocity flow profile distribution. The disruption of the parabolic flow profile would extend the time for diffusion at the interface between the fluids. Due to the flow restrictions where the obstacles are placed, there is an increase in the local velocity to conserve the mass flow rate, which must remain constant for incompressible fluids, i.e. the average inlet flow rate must be the same as the outlet flow rate. No experimental verification was performed to complement the modelling.

5.1.3 Parameters to consider for micromixers

Many researchers have quoted various factors that ideally should be taken into account when considering using or designing a micromixer. These include the performance, throughput, operability, ease of maintenance, absence of clogging and avoidance of high-pressure drop.[39;63;76]

Because of the length of channels needed to mix fluid streams by diffusion and the limited size of microfluidic devices, a serpentine channel design is ideal to maximise mixing in a limited chip space. However, increasing the length of channels to mix fluids has the disadvantage of increasing the pressure drop, making the flow of fluids more difficult.[76] An ideal simple passive micromixer should enhance the mixing performance without increasing the pressure drop by a great extent.[76]

5.2 Experimental Details

5.2.1 Microfluidic mixing system

Solutions of ANS in pure methanol and a water-methanol mixture (30.8% water v/v), prepared and stored as described in Section 4.2.1, were pumped into the commercial micromixers. The flow of fluids from the syringes was controlled by a syringe pump (KDS200, KD Scientific), in these experiments a different model was used from the previous experiments.

Fluorescence was excited and collected through a 0.5 mm polymer layer (Figure 5.1), in comparison with a 0.16 mm thick optically transparent glass microscope coverslip used in the previous T-shaped micromixer. The microfluidic channels were fabricated on a 2 mm thick polymer sheet, which was then sealed to the 0.5 mm thick polymer sheet.

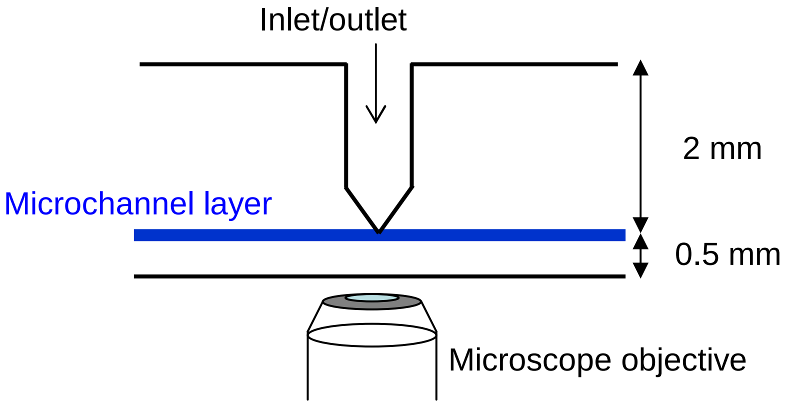

Figure 5.1: Diagram showing the side-view of the Epigem micromixer chips. The microfluidic channels, represented by the blue layer, were imaged from below the device through a 0.5 mm layer of polymer.

The microfluidic chips were robust and durable due to the 2 mm polymer-top layer, in which the fluid inlet and outlet ports were connected *via* compression ferrules to fluidic connectors screwed vertically onto the chip. Each of the chips contained eight mixing designs in which the fluidic connectors and ferrules could be removed and reconnected to any of the mixers on the chip. The fluidic connectors had horizontal screws through which tubing leading to the syringes could be threaded and pressure sealed onto the chip connector *via* larger ferrules. Originally the chips were provided with PTFE tubing, which was expected to provide a good seal with the connectors to the mixer chips, but failed. Instead polypropylene tubing (outer diameter 1.65 mm) cut from dispensing tips (EFD Inc.), as used in the previous chapter with the simple T-mixer, gave a much better seal to the larger ferrules. The polypropylene tubing was connected to syringes as detailed previously in Section 4.2.2. The lack of robust seals between fluidic components ultimately restricted the flow rates to limit the pressure on the seals and prevent leakage.

A photograph of several micromixers fabricated onto one of the chips is shown in Figure 5.2. This illustrates the intricate designs of a selection of the mixers.

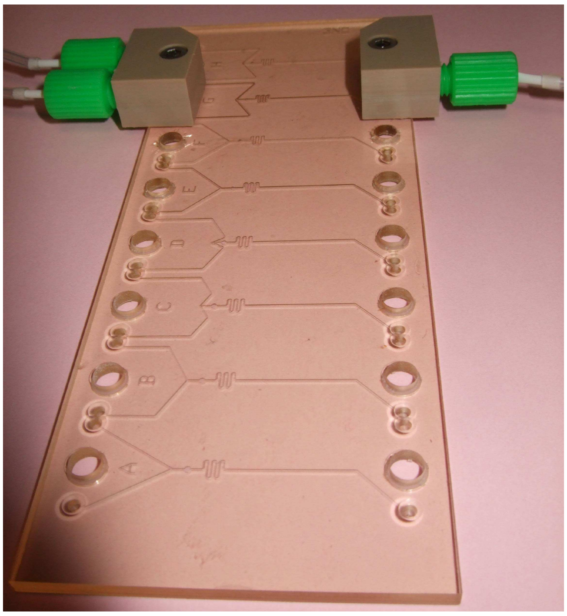

Figure 5.2: Photograph of an Epigem chip with eight micromixer geometries, with the fluidic connectors attached to one micromixer.

The channel dimensions of the mixers were verified at one channel position by intensity-based confocal microscopy with the measured dimensions calibrated against a Richardson test slide. The dimensions were consistent with Epigem's dimensions except for channel widths quoted of 100 µm; these were actually measured as 80 µm.

The extensive length of the mixing channels (maximum of 50 mm) increased the back pressure on the inlet fluids. The pressure drop which is necessary to force fluids to flow within the channels is proportional to the channel length ($\Delta P \propto L$).[29;33] Therefore, for longer channels the pressure drop increases and can even result in leaking from the connectors due to the resulting high pressures. As a consequence the flow rates were reduced to eliminate this problem. The problem of leaking from connectors has been encountered by many experimental researchers in the field, some of whom experienced great difficulty in validating modelling at higher flow rates.[27;33] The problem was exacerbated when using reduced channel dimensions due to the inverse fourth power dependence of the pressure drop ($\Delta P \propto d_h^{-4}$).[29;76] Hence, a constant volumetric flow rate of 20 µL/min was selected for all of the micromixers, as the microchannel dimensions ranged from 80 µm to 300 µm in width but all were fabricated with a depth of 150 µm. In addition, blockage problems where observed with the narrower microchannels with width of 80 µm. Figure 5.3 shows a FLIM image of a microfluidic chamber with a blockage at the entrance channel to the chamber which was situated in the mixing channel downstream from the fluid confluence. Blockages have been reported as a problem previously by some researchers who tackled this by using micro-filters inserted before the fluids enter the microchannels.[39;77]

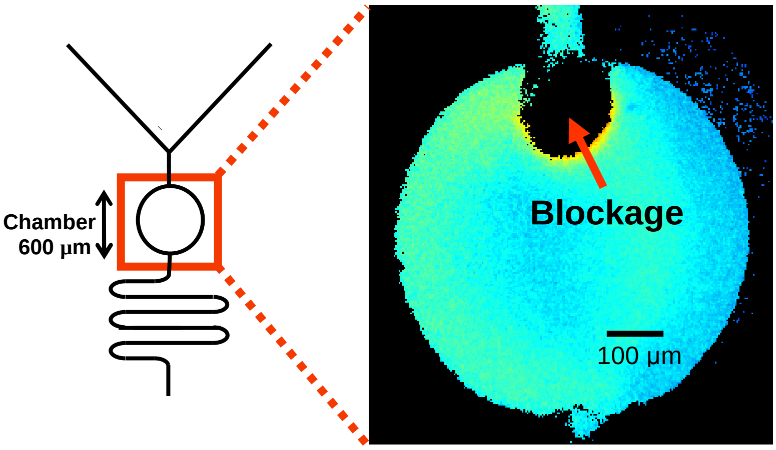

Figure 5.3: FLIM image of a microfluidic chamber with a blockage at the channel entrance. The channel dimensions are 80 µm wide by 150 µm deep and the chamber has a diameter of 600 µm and a depth of 150 µm.

The material of the Epigem micromixers was observed to have a quenching effect on the fluorescence lifetime of ANS in the pure methanol inlet stream. This quenching was only observed only within approximately 5-10 µm of the channel edges. The lifetime of ANS in the equimolar water-methanol mixture does not appear to be affected by the surfaces, this maybe due to the already reduced lifetime by the presence of water. This quenching of the fluorescence lifetime of ANS in pure methanol can sometimes be observed at the extreme edges of the MeOH inlet channel in some of the FLIM images. However, this quenching effect is mostly not even noticeable. The effect becomes less apparent as the fluids become mixed with consequent reduction in the ANS lifetime. This effect was not observed in the previously studied T-shaped mixers and therefore can be attributed to an effect of the material of the Epigem mixers. The limited information on the material and fabrication of the commercial micromixers prevents identification of the nature of this quenching effect. However, the effect could be eliminated by changing the composition of the inlet mixing fluids. In the present studies, an equimolar water-methanol mixture with a lifetime of 2.4 ns was selected for use instead of pure water with a lifetime of 240 ps, as it proved too difficult to acquire sufficiently accurate FLIM images with the commercial gated-CCD camera apparatus and software to cover the extended dynamic range of 240 ps to 6 ns (pure methanol). With the benefit of hindsight, it is apparent that changing the two inlet fluid compositions to an equimolar water-methanol mixture and pure water would overcome the quenching problem. This would, of course, require a new lifetime to fluid composition calibration to be performed by the TCSPC technique.

If the quenching problem is a consequence specifically of using methanol, other alcohols could be used instead with ANS; for example, the fluorescence lifetime of ANS in ethanol is 8.9 ns and that in propanol is 10.2 ns.[78] This would also be extremely useful to investigate the effects of other fluid properties on microfluidic mixing.

To prevent the confusion of quenching and mixing effects on the fluorescence lifetimes, the composition profiles were cropped ~5-10 µm from the channel surface at the methanol side.

5.2.2 Fluorescence lifetime imaging of the micromixers (FLIM)

The fluorescent lifetime imaging experiments were performed as described in Section 4.2.3. However, the integration time for each image was 0.02 s, with 0.05 ms readout time, giving a total acquisition time of approximately 16 s for each FLIM image. A 40x objective (PF, NA=0.60, Nikon) was used to record FLIM images of micromixer C, whereas all the other FLIM images presented within this chapter were recorded using a 20× objective (PA, NA=0.75, Nikon).

5.3 Results and discussion

5.3.1 Comparison of FLIM with intensity-based imaging

In the previous chapter the significant difference between the intensity-based and FLIM imaging for an extremely simple microfluidic design of a T-shaped mixer (Figure 4.8) was noted. The imaging of the fluid mixing in this simple design was performed through a glass microscope coverslip of thickness 0.16 mm, providing optimal optical transparency. Therefore, it is likely that intensity-based imaging will be even more prone to optical artefacts in more complex microfluidic devices.

Figure 5.4a and b display the intensity and FLIM image respectively for the confluence zone of one of the commercial micromixers.

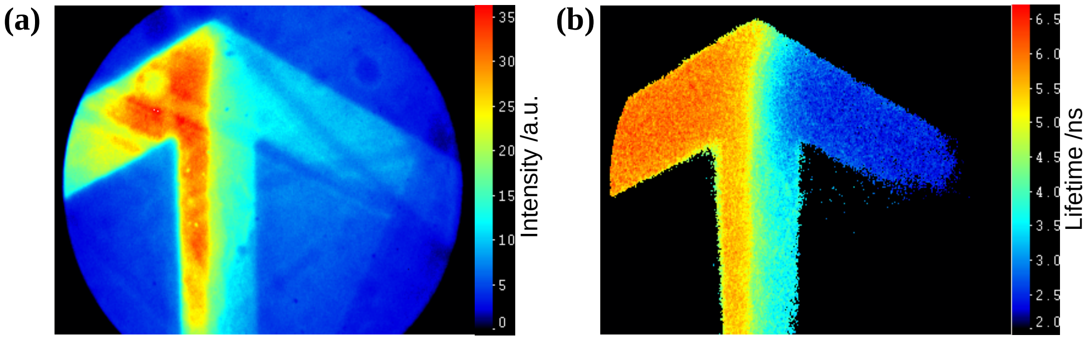

Figure 5.4: Comparison of fluorescence intensity image **(a)** and FLIM image **(b)** for the mixing of solutions of ANS in pure methanol and ANS in a water/methanol mixture (70:30 v/v), using a commercial micromixer arrangement. The flow rate of fluids in both inlets was 20 μL/min. Surface scratches are evident in the intensity image, but absent in the FLIM image.

The intensity image was constructed as described in Section 4.3.2.1 and both the intensity and FLIM images are displayed using the same pseudocolour scale. Along with the noticeable irregularities in the intensity image in comparison with the FLIM image, the effects of surface scratches and other deformations in the 0.5 mm polymer layer imaged through are evident and inhibit the extraction of any quantitative information. The FLIM image is totally unaffected by these problems and is hence suitable for evaluating mixing within a variety of commercial micromixers that are not specifically fabricated for optical imaging purposes. The polymeric micromixers were observed to be prone to surface scratches, although they were stored in separate sealed plastic bags to reduce damage. An example of the scratches is shown in Figure 5.4a, the scratches can be identified by the straight lines through the image which display lower intensities than the surroundings.

5.3.2 Effect of inlet channel geometry on mixing

The effect of changing the inlet channel geometry of the micromixers, defined as the angle of the confluence, on mixing was investigated. Micromixers A and B with confluence angles of 45^{o} and 120^{o} respectively (Figure 5.5), were selected for this study. Micromixers A and B had a generic channel structure shown in Figure 5.6, with channel dimensions of 300 µm wide and 150 µm deep (Figure 5.5).

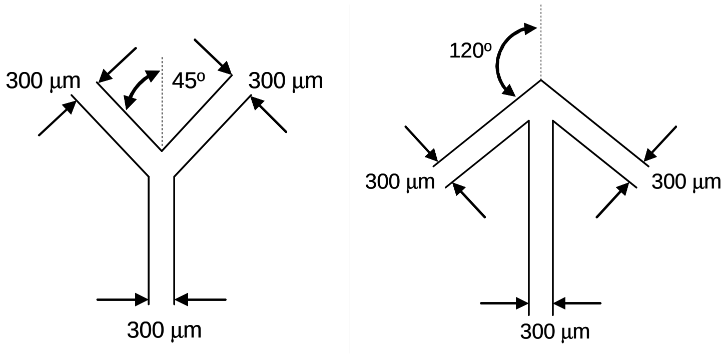

Micromixer A

Micromixer B

Figure 5.5: Diagram showing the channel geometry with confluence angle and dimensions of micromixers A and B. The confluence angles were 45^{o} and 120^{o} degrees from a vertex extended from the mixing channel for mixers A and B, respectively. The channel dimensions were 300 µm by 150 µm (width by depth).

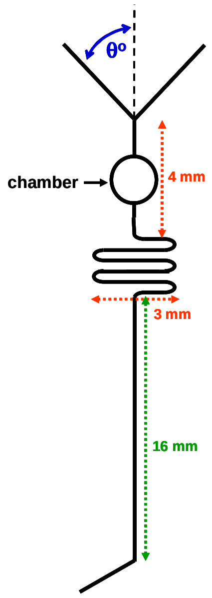

Figure 5.6: Diagram showing the generic channel design and lengths of micromixers A, B and C. The chamber diameter was 600 µm for these mixers.

A series of FLIM images were recorded at various positions in micromixer A and B, as shown in Figure 5.7.

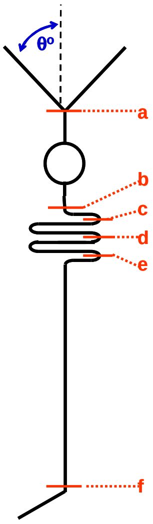

Figure 5.7: Diagram identifying the positions on the generic channel design where FLIM images were recorded, from which composition profiles for each micromixer were compiled. Position: **(a)** at the confluence zone, **(b)** the first 90^{o} degree bend, **(c)** the first 180^{o} bend, **(d)** the second 180^{o} bend, **(e)** the third 180^{o} bend, **(f)** at the end of the mixing channel.

The FLIM images and corresponding composition profiles at each position in the micromixers are presented in Figure 5.8. The graphs in Figure 5.8 show the composition profiles along the cross-sections drawn on the corresponding FLIM images for micromixers A and B.

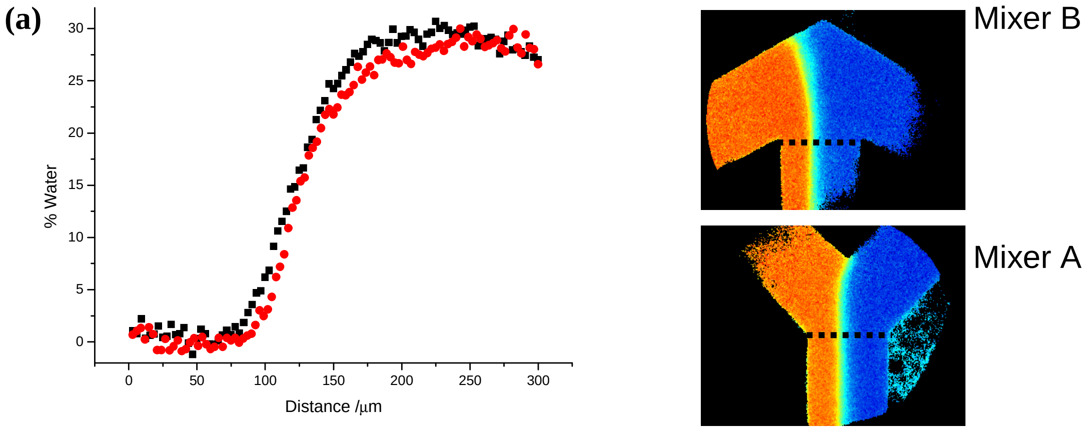

(b)

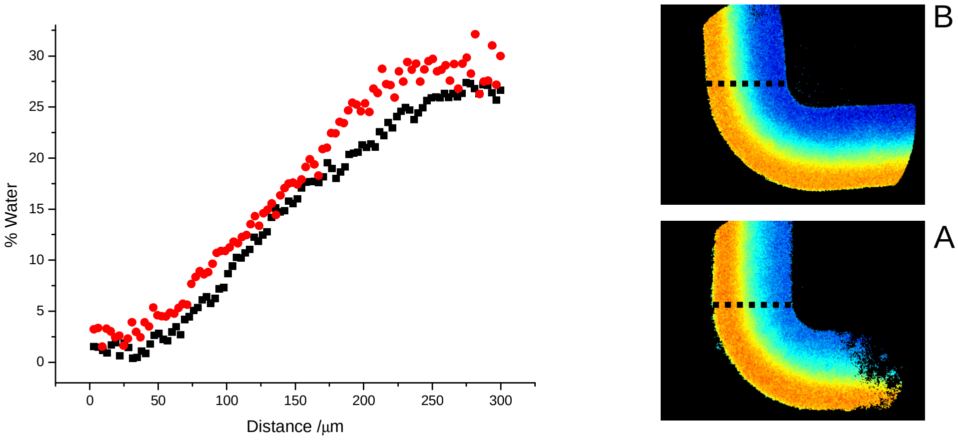
% Water
0
5
10
15
20
25
30
0
50
100
150
200
250
300
Distance /μm
B
A

(c)

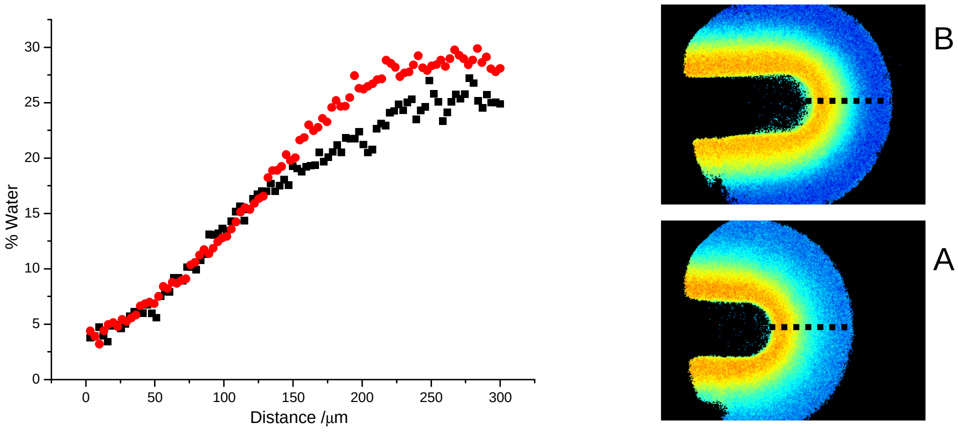
% Water
0
5
10
15
20
25
30
0
50
100
150
200
250
300
Distance /μm
B
A

(d)

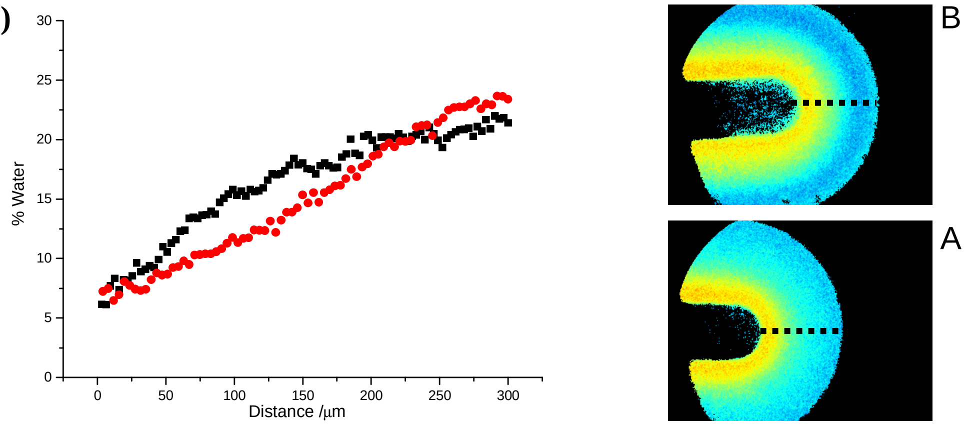
% Water
0
5
10
15
20
25
30
0
50
100
150
200
250
300
Distance /μm
B
A

(e)

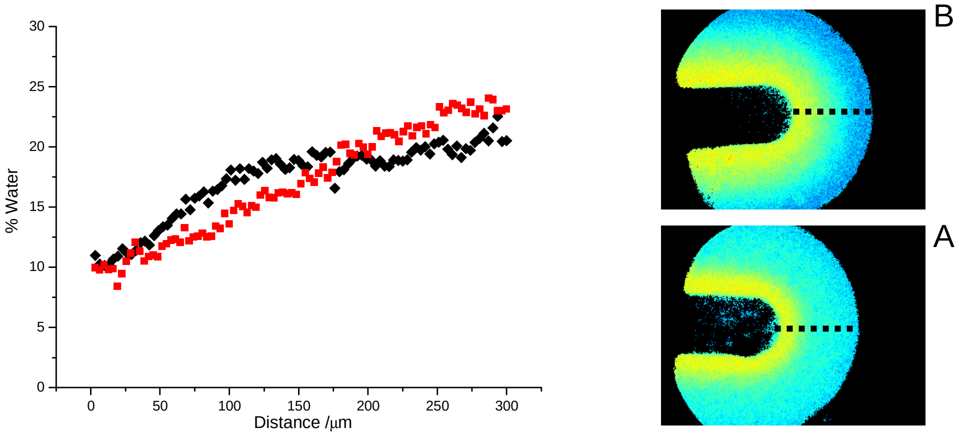
% Water
0
5
10
15
20
25
30
0
50
100
150
200
250
300
Distance /μm
B
A

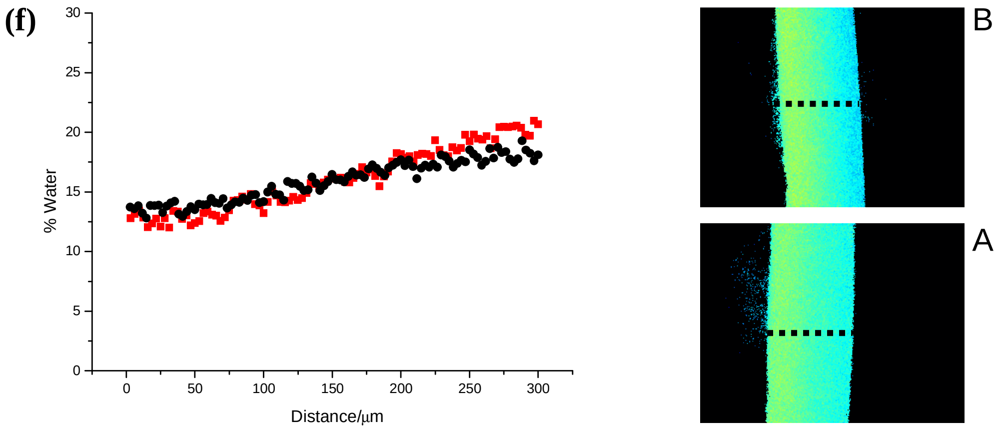

Figure 5.8: FLIM images for the mixing of solutions of ANS in pure methanol and ANS in a water/methanol mixture (70:30 v/v) in micromixer A and B. Percentage water composition profiles for micromixer A (black profile) and B (red profile) are also shown, corresponding to the appropriate FLIM images. The FLIM images show the cross-sections along which the composition profiles were extracted. The FLIM images labelled as **(a-f)** were recorded at the corresponding positions **(a-f)** as depicted in Figure 5.7.

The FLIM images of the confluence zone for mixers A and B (Figures 5.8a) show that the fluid interface is skewed off centre to the left-hand side of the mixing channel. This affect is more noticeable in the composition profiles of each mixer. Both the inlet fluids have the same volumetric flow rates but due to differing viscosities and densities each fluid stream develops different velocity fields. This leads to a non-symmetric velocity profile of the fluids at the confluence. The shape of the fluid interface is influenced by the fluid properties. If the fluid properties were identical then the velocity field would be identical for each fluid stream and the fluid interface would be expected to be symmetrical rather than skewed. A curved fluid interface is visible in both FLIM images at the confluence zone, the interface is curved to the left in the ↑-shaped junction, whereas it is curved to the right in the Y-shaped junction. The FLIM images and corresponding composition profiles at the confluence of the two fluids (Figure 5.8a) for both mixers shows that the H_2O-MeOH fluid mixture (represented by blue in the FLIM image) occupies a greater volume of the mixing channel. This is clearly evident in the profiles with the ratio between the horizontal regions representing pure methanol and the H_2O-MeOH mixture. From the profile, the area occupied by the H_2O-MeOH mixture is almost double that of the pure methanol. This can be explained by the large difference in viscosity between the two inlet fluids. Symmetrical flows can be achieved by changing the relative pressures in the two inlet streams. The fluid flow after the confluence is determined by the fluid properties, i.e. the viscosity and density of the mixtures. Even simulating mixing of fluids with similar fluid properties can be complex, which explains why computational modelling usually includes many assumptions. Both the viscosity and density of methanol and water mixtures displays a very strong non-linear relationship with the compositions.[79;80] At this stage the effect of the junction angle appears to have little impact on fluid mixing.

Although the fluid velocity profile displayed in the theory section displays a symmetrical parabolic flow this is usually true for single fluid components or the flow of parallel fluid streams with similar fluid properties and with no temperature deviations. However the profile will be distorted with parallel streams of MeOH and a H_2O-MeOH mixture due to the significant difference in fluid properties. This is demonstrated by the FLIM images and composition profiles illustrated in Figure 5.8a. When the fluid interface is skewed to the left after the confluence and the cross-sectional areas occupied by the fluid stream is non-symmetrical, the methanol stream has a higher velocity, due to the smaller cross-sectional area of the stream, to conserve the mass flow rate.

It is interesting to observe the effect of the 90° and 180° bends on the fluid mixing. It is evident from the FLIM images that these appear to have a minimal effect on the mixing. The fluid streamlines appear to follow the curve of the channels displaying an interesting rainbow-like effect. The variations between the profiles from mixer A and B are most noticeable in Figures 5.8d and e, which shows a curved profile for mixer A (Y-shaped confluence) and a linear profile for mixer B (↑-shaped confluence) at both the second and third 180° bends. This may be explained by the fluid velocity profile which will be distorted from a typical straight channel profile due to the effect of the bends and as the distance travelled by fluid streamlines is greater at the outside of the curved channel. Research by Yamaguchi *et al.* suggested that the normally vertical interface (I shaped) between the fluids is distorted to a curved interface (> shaped) which may have an influence the mixing profiles. However, this does not explain the linear profiles for mixer B. Another suggestion is the effect of defects in the channel structure which has been acknowledged to cause deviations in mixing.[33] A third suggestion is the presence of flow fluctuations which are know to occur from syringe pumps and are more pronounced at lower flow rates.[81] It is unlikely that the latter should occur in only one mixer, therefore it may be the result of channel deviations or an effect of different focal planes when recording the images.

The effect of the confluence angle does not appear to greatly influence mixing at the flow rates employed. The Péclet number for the inlet streams of methanol and the water-methanol mixture was constant for both mixers at 680 and 1170, respectively. This would suggest that neither micromixer increased the mixing by diffusion alone. On inspection of the final profiles at the end of the mixing channel the Y-shaped junction would seem to have very slightly enhanced the mixing. However, without explaining the irregular curved profile displayed by this mixer at the bends, it is difficult to confirm the effect is entirely due to the geometry of the confluence. Significantly higher flow rates may produce a more noticeable dependence of the mixing on the confluence angle. At higher Re numbers T- and Y-shaped micromixers can generate vortices at the collision zone which results in the fluid stream being split and streamed to reduce the diffusion length.[63] This would present an ideal opportunity to employ confocal FLIM techniques to probe fluid layering effects predicted within microfluidic devices.[36] However, flow rates were limited in this study due to the inability of fluidic connectors to maintain a tight seal at significantly higher flow rates.

5.3.3 Effect of channel dimensions on mixing

The effect on mixing on changing the channel dimensions of the micromixers was investigated. Micromixer B (↑-shaped confluence), examined in the previous section, was compared with Micromixer C, an identical mixing design except the width of the channels was reduced from 300 µm to 80 µm (Figure 5.9). Both mixers B and C have channel depths of 150 µm, confluence angles of 120^{o} and a generic channel structure as shown in Figure 5.5. Mixer B, with channel dimensions of 300 µm by 150 µm, has a channel aspect ratio (ratio of channel width to depth) of 2, whereas mixer C, with dimensions of 80 µm by 150 µm, has an aspect ratio of ~ 0.5. The Re numbers in these mixers were all below 4, with the Re numbers for the wider channel approximately half that of the smaller channel.

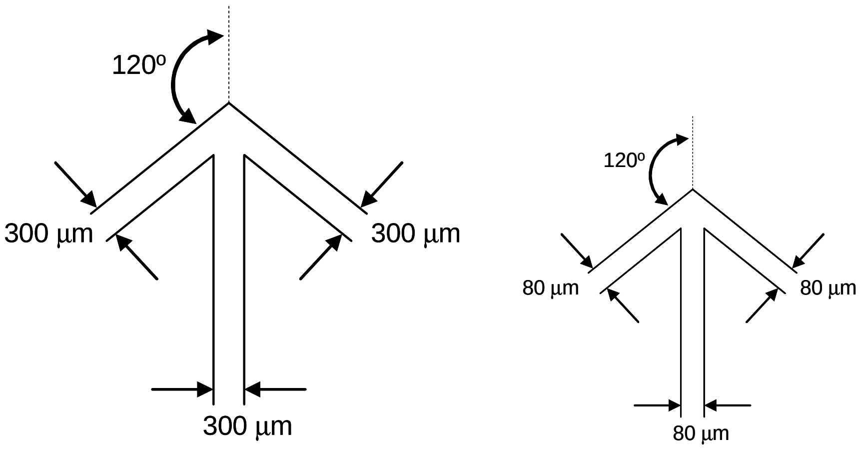

Micromixer B

Micromixer C

Figure 5.9: Diagram showing the channel geometry and dimensions of micromixers B and C. The channel widths were 300 µm and 80 µm for micromixers B and C, respectively. The channel depth for both mixers was 150 µm.

FLIM images were recorded at positions **a, b, e** and **f** of micromixers B and C, as illustrated in Figure 5.7. The FLIM images and corresponding composition profiles at each position are presented in Figure 5.9. The graphs (Figure 5.10) show the composition profiles along the cross-sections drawn on the corresponding FLIM images for micromixers B and C.

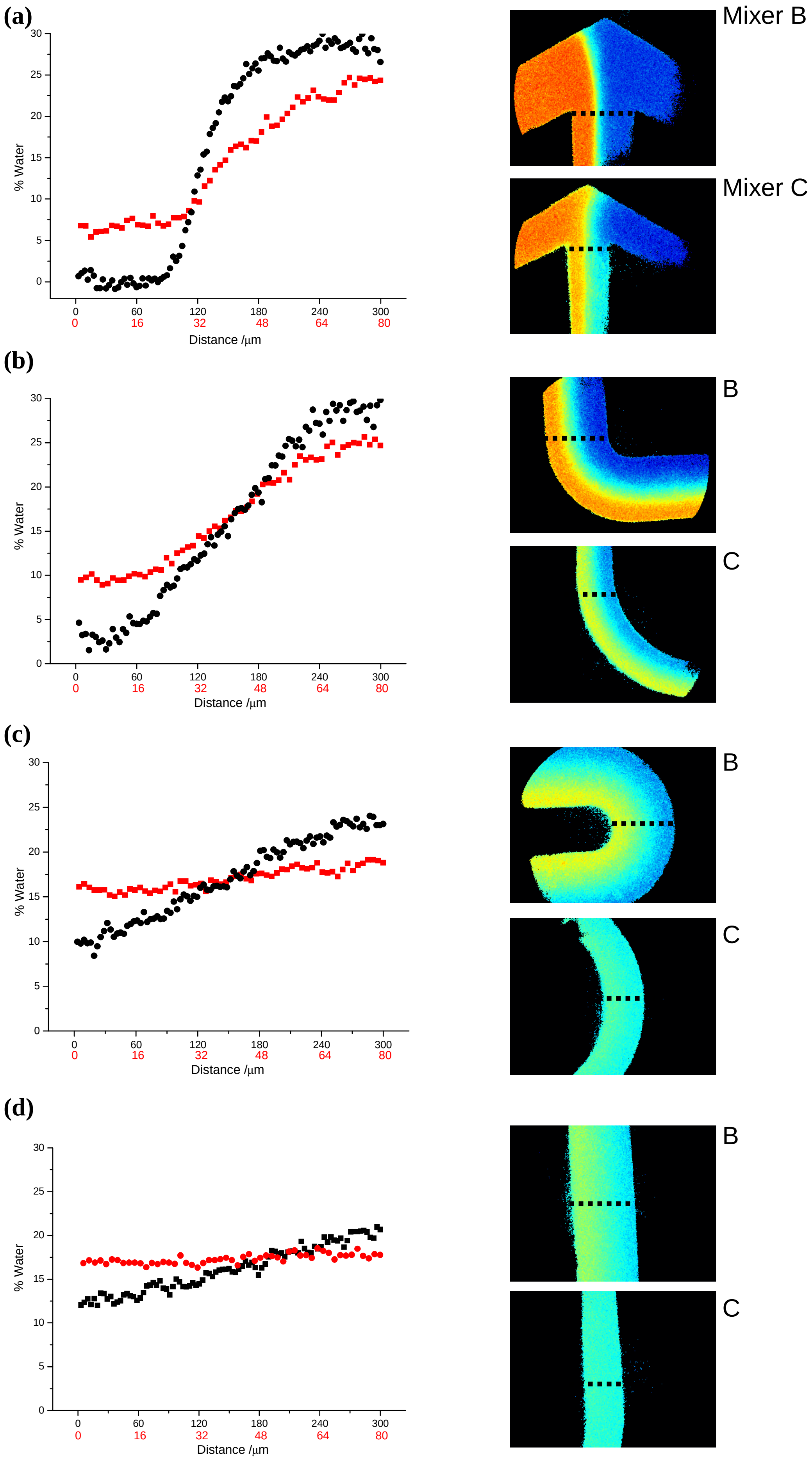
(a)
Mixer B
Mixer C
% Water
30
25
20
15
10
5
0
0 60 120 180 240 300
0 16 32 48 64 80
Distance /µm
(b)
B
C
% Water
30
25
20
15
10
5
0
0 60 120 180 240 300
0 16 32 48 64 80
Distance /µm
(c)
B
C
% Water
30
25
20
15
10
5
0
0 60 120 180 240 300
0 16 32 48 64 80
Distance /µm
(d)
B
C
% Water
30
25
20
15
10
5
0
0 60 120 180 240 300
0 16 32 48 64 80
Distance /µm

Figure 5.10: FLIM images for the mixing of solutions of ANS in pure methanol and ANS in a water/methanol mixture (70:30 v/v) in micromixer B and C. Percentage water composition profiles for micromixer B (black profile) and C (red profile) are also shown, corresponding to the appropriate FLIM images. The distance scale on the x-axes is displayed in black for micromixer B and in red for micromixer C, corresponding to the profile colours. The FLIM images show the cross-sections along which the composition profiles were extracted. The FLIM images labelled as **(a-d)** were recorded at corresponding positions **(a, b, e, f)** respectively, as illustrated in Figure 5.7.

The spatial resolution was reduced when recording FLIM images of the narrower channels due to the inability to progress to a higher magnification object than 40x. The higher magnification objects had considerably shorter working distances and long working distance objectives beyond x40 magnification were not available. Long working distance objectives are necessary to image through 0.5 mm of plastic to reach the plane of the microchannels.

The FLIM images at the confluence of both mixers shows an interesting effect on the curve of the fluid interface (Figure 5.10a). The wider-channelled mixer B shows the interface curved to the left-hand side, towards the pure methanol inlet, whereas the narrower-channelled mixer C displays the interface curved towards the opposite side at the H_2O-MeOH inlet. Although the volumetric flow rates are equivalent at 20 µL/min, the fluid velocities will be significantly higher in the narrower channels of mixer C. The average fluid velocity in the narrower inlet channels of mixer C is 27.8 mm/s and that in the wider inlet channels of mixer B is 7.4 mm/s, scaling appropriately with the ratio of channel widths. These velocity values will double in the corresponding mixing channels. The interface shape was stable in both mixers and observed in additional consecutive images of each confluence area. The change in the interface shape could be an effect of the fluid velocities and channel dimensions in relation to the fluid properties. This can ideally be investigated with CFD to extract the influence of various parameters on the fluid interface shape. The composition profiles at the entrance to the mixing channels (Figure 5.10a) show that the narrower channels actually have a significant effect on the mixing, as the composition profile gradient is considerably reduced (red profile in Figure 5.10a) and the profile shape is progressively more linear in comparison to the profile across the wider channel (black profile in Figure 5.10a). This effect is likely due to the increased shear rate of the fluids at the confluence zone and entering the mixing channel due to the reduced dimensions of the channels. The shear rate is the change of velocity at which one layer of fluid passes over another adjacent layer.[63] In the narrower channels the fluid velocity is nearly four times higher (x3.75) than the wider channels and the confluence area is nearly four times smaller (x3.75) than that of the larger channel. The hydraulic diameter for the narrower channels is approximately half that of the wider channels. The shear rate can be defined as the velocity gradient, i.e. the velocity divided by the confluence zone diameter; for the narrower channel this is a factor of 7.2 times greater than that of the larger mixing channel.

This rapid mixing effect due to the shear rate at the confluence does not appear to be propagated down the mixing channel, as the difference in the profiles between the two channels appears to remain similar further down the mixing channel. This is evident from comparison of the profiles in Figure 5.10b, recorded after the fluids had progressed approximately 4 mm down the mixing channel, with the profiles in Figure 5.10a. The 4 mm length of channel has had a noticeable effect on mixing in the wider mixing channel, as shown by the decrease in gradient of the black profile in Figure 5.10b compared with that in Figure 5.10a.

Although mixing is improved in the narrower channel, the fluids are still not totally mixed at the third 180^{o} bend, after progressing nearly 18 mm through the mixing channel, as shown by the red profile in Figure 5.10c, which is not horizontal. It took an additional 32 mm of progress through the channel to ensure the fluids were totally mixed, as is shown by the horizontal red profile in Figure 5.10d. Therefore, the fluids had to travel the entire length of the mixing channel to achieve full mixing. In the wider mixing channel the fluids are still not fully mixed at the exit, as seen by the positive gradient of the black profile in Figure 5.10d. To achieve complete mixing within this channel the volumetric flow rate would have to be reduced to increase the residence time to allow full mixing by diffusion. The fluid residence times for the wider and narrower mixing channels are 6.75 s and 1.8 s respectively, taking the mixing channel length to be 50 mm. Although the residence time for the narrower channel is significantly lower, the fluids are fully mixed at the exit. Therefore, it is advantageous to use a narrower channel dimension to increase mixing, but there will be a payoff with an increased pressure drop due to the smaller dimensions. From these results it appears that the increase in mixing efficiency is mainly due to the increase shear rate of the fluids in the confluence zone which induces more rapid mixing, rather than an effect throughout the length of the mixing channel. Reducing the channel width reduces the length over which molecules must diffuse to fully mix, thereby reducing the time necessary for diffusion. However, the linear velocity of the fluids in smaller channels is increased which may hinder the lateral diffusion required for mixing. The Péclet numbers for micromixer B (300 µm wide) for the methanol and water-methanol inlet are 680 and 1170, respectively. The Péclet numbers for micromixer C (80 µm wide) for the methanol and water-methanol inlet are 1320 and 2290, respectively. The higher Péclet numbers for the narrower channel confirm that the lateral diffusion ratio to the convection of the fluid through the channel is reduced. Hence, the enhanced mixing observed can be attributed to the increased shear rate of the fluids. The interfacial area between the fluids in each micromixer is equivalent, as the depth of the each channel is 150 µm in both cases although this was only verified at one position. (The National Physical Laboratory is currently performing dimensional characterisation on a range of Epigem microfluidic channels.)

5.3.4 Effect of incorporation of a chamber on mixing

Micromixers A, B, C and F all had a microfluidic chamber situated downstream of the confluence but upstream of the serpentine channel geometry, as shown in Figure 5.6. The chamber shape is comparable to a cross-section through a cylinder. The depth of all the channels and chambers was assumed constant at 150 µm, with the dimensions of the channel width and chamber diameter for the micromixers listed in Table 5.1.

Micromixer	Channel width /µm	Chamber diameter /µm
A	300	600
B	300	600
C	200	800
F	200	800

Table 5.1: The dimensions of the channel width and chamber diameter for micromixers A, B, C and F.

The effect of the varying the flow rate and chamber diameter can be clearly observed in Figure 5.11. This shows chambers with diameters of 600 µm and 800 µm, with inlet flow rates of 20 µL/min and 5 µL/min.

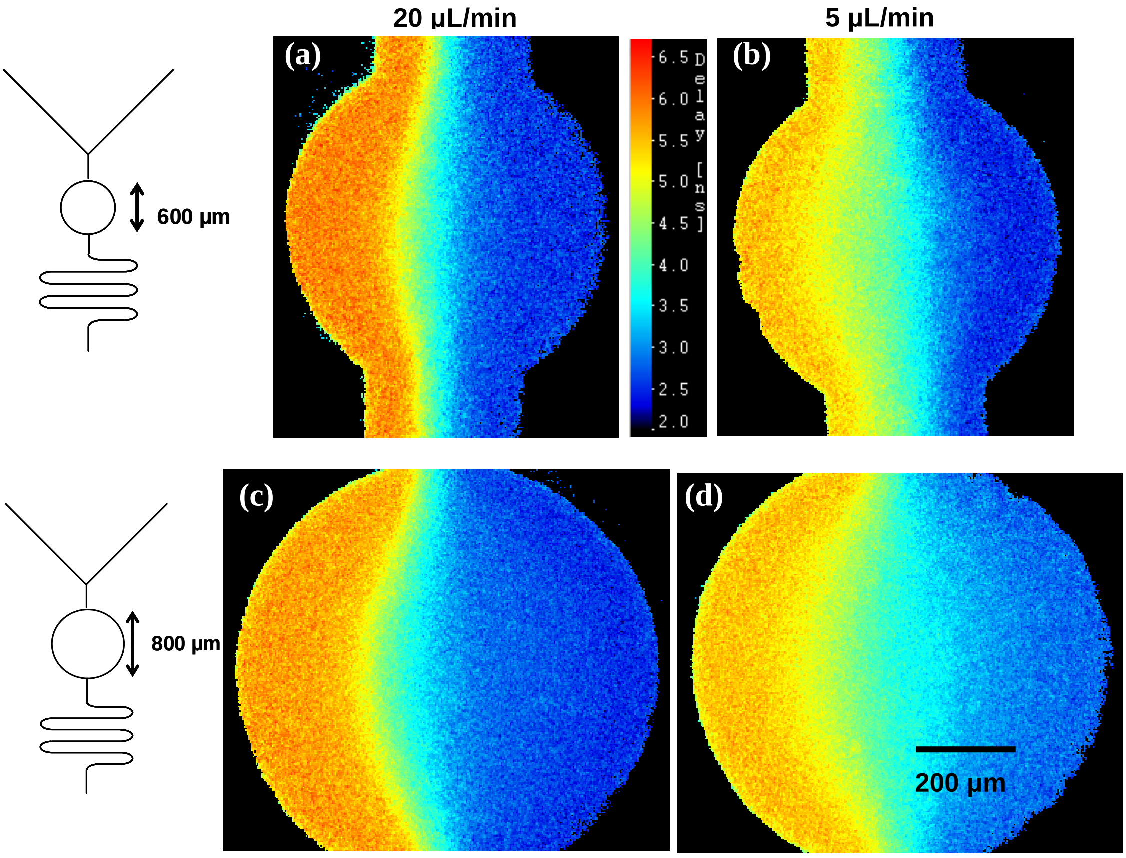

Figure 5.11: FLIM images of various sized chambers. Chambers **(a)** and **(b)** have diameters of 600 µm and chambers **(c)** and **(d)** diameters of 800 µm. The depths of all the chambers is 150 µm. The inlet flow rates of chambers **(a)** and **(c)** was 20 µL/min and that of chambers **(b)** and **(d)** was 5 µL/min.

What is most noticeable is the temporary expansion of the mixing region at the fluid interface in the centre of the chamber; this is most marked at the lower flow rate. The chamber has the effect of stretching the fluid velocity profile and temporarily decreasing the fluid velocity to compensate for the greater volume. This will increase the residence time but will also increase the diffusion length over which lateral diffusion must occur for mixing. This effect is not sustained, as the fluid progresses through the outlet channel the fluid velocity returns to a similar value to that on entry to the chamber.

5.3.5 Effect of asymmetric curves in the vertical mixing channel walls

The next micromixer design tested was micromixer D, as illustrated in Figure 5.12. This mixer had three sharp asymmetric curves fabricated on each of the vertical mixing channel walls covering a 1 mm channel distance immediately after the confluence, followed by a straight 21 mm mixing channel. The general channel width was 200 µm and 150 µm deep, with the angle of confluence at 45^o to the mixing channel.

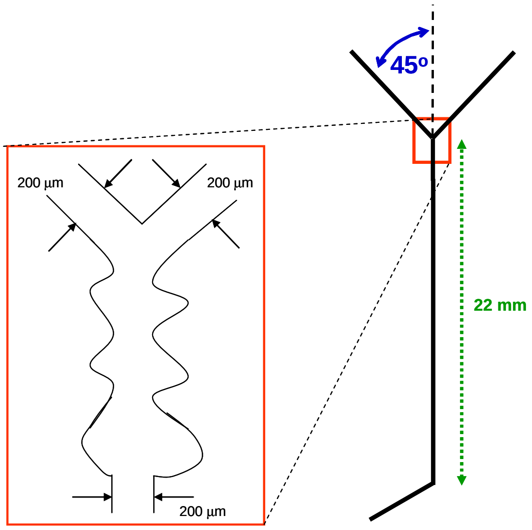

Figure 5.12: Diagram of micromixer D with the confluence zone and entrance of the mixing channel magnified to highlight the asymmetric bends in the vertical channel walls.

FLIM images were recorded at the fluid junction, covering the region of curves in the mixing channel and before the exit of the mixing channel (Figure 5.13).

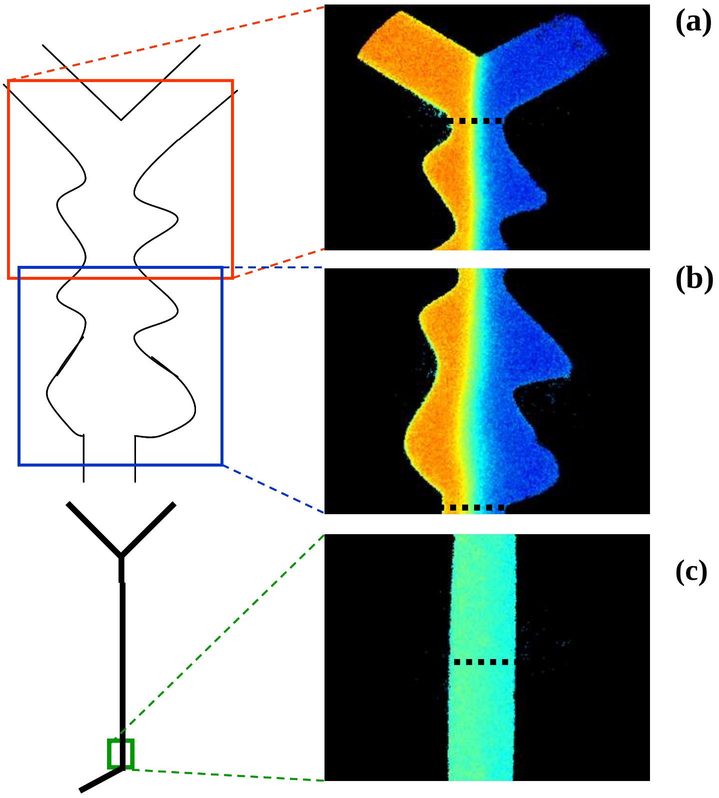

Figure 5.13: The diagrams show the selected areas of micromixer D were the FLIM images were recorded. The FLIM images show the cross-sections along which the composition profiles were extracted for Figure 5.14.

The FLIM image of the confluence zone (Figure 5.13a) shows a slight curve to the fluid interface which is similar to the FLIM image of micromixer A with identical confluence angle but with a width of 300 µm instead of 200 µm (Figure 5.8a). However, the curve appears to be less pronounced in the 200 µm wide channels. The first sharp curves immediately following the junction appear to have little effect on the mixing region from inspection of the FLIM image (Figure 5.13a). From observation of the fluid interface and mixing region at the third and largest set of curves in Figure 5.13b, it can be noticed that the mixing region is expanded at the widest region of the channel, displaying a similar effect to that seen in the chamber in Figure 5.11. The sharp curves continuously broaden and narrow the width of the channel three times, which has the effect of stretching and condensing the fluid velocity profile, whereby at the widest regions the flow velocity is temporally decreased allowing an increase in residence time, hence the expanded mixing region or fluid interface. However, this is not propagated down the channel and has only a localised effect. This is evident from the comparison of the composition profiles of the fluids at the entrance to the mixing channel and after the series of sharp curves, displayed by the red circles and black squares, respectively, in Figure 5.14. These profiles show little difference and demonstrate the overall lack of effectiveness of the curves and the temporary expansion of the mixing region. From the FLIM image recorded before the fluid exits the mixer (Figure 5.13c), the fluids may appear fully mixed, but the composition profile across the channel is not horizontal (blue triangles in Figure 5.14), therefore mixing is not complete.

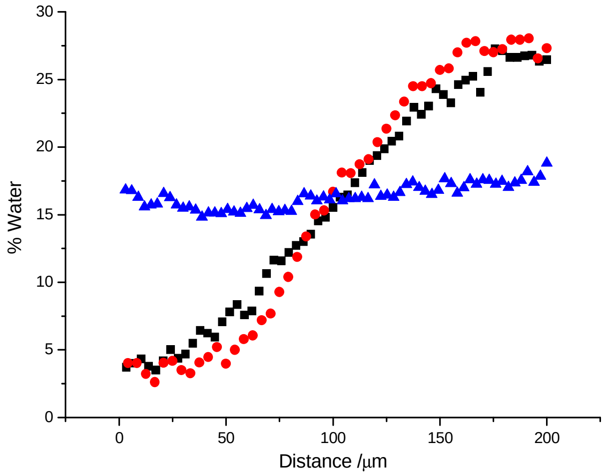

Figure 5.14: Composition profiles for micromixer D. The red circles, black squares and blue triangles represent the composition along the cross-sections displayed in the FLIM images from Figure 5.13 **a, b** and **c**, respectively. The red composition profile is taken as the fluids enter the mixing channel, the black profile after the fluids pass through the series of sharp curves in the mixing channel and the fluid composition at the end of the 22 mm mixing channel is represented by the blue profile.

First described by Stroock et al., a more effective design to enhance mixing would be the use of a staggered herringbone mixer which has grooves fabricated into the underside and topside of the mixing channel.[23] This continually stretches and folds the fluid interface, effectively stirring the fluids and increasing the surface area over which diffusion can occur,[82] thus reducing the mixing length necessary to homogenise unmixed fluids.

5.3.6 Effect of columns in the mixing channel

The effect of vertical columns or obstacles randomly placed in the mixing channel was studied to investigate if these could increase the mixing efficiency. The channel dimensions were identical to the previous mixer D, at 200 μm wide by 150 μm deep, but had a confluence angle of 120° (Figure 5.15). Ten vertical columns of elliptical cross-section, with a length of 100 μm, were fabricated at the confluence zone and within 1 mm of the entrance of the mixing channel (Figure 5.15). A constant flow rate of 20 μL/min was maintained for this study. Attempts to investigate the mixing effect of the columns at lower flow rates were hampered due to problems with air bubbles trapped between some of the obstacles, thereby reducing their effect.

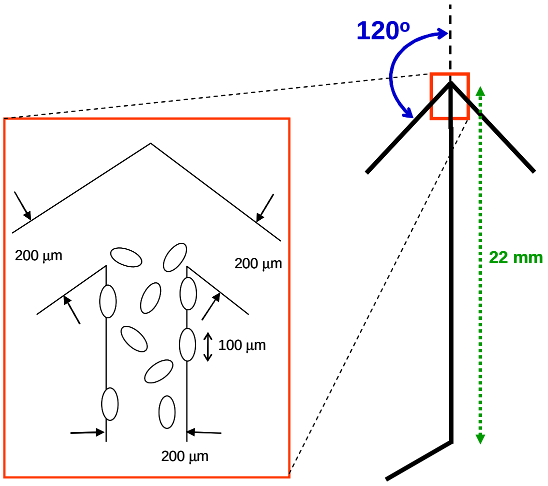

Figure 5.15: Expanded diagram of the confluence zone for micromixer E showing the channel geometry, dimensions, and the positions of the ten vertical columns at the entrance of the mixing channel. The channel dimensions are 200 μm by 150 μm (width by depth), with a length of 100 μm for the elliptical columns.

The increased surface area produced by the introduction of the columns created more resistance to the flow of the fluids and caused constant flow fluctuations. The interface between the two inlet fluid streams was not stable but fluctuated considerably as shown in Video 5.1 from the supplementary information on CD. Video 5.1 displays images of the performance of the micromixer recorded with confocal fluorescence intensity imaging. The scan speed of the data acquisition was such that complete images were acquired at a frame rate equivalent to 4.7 Hz. The video was recorded at the confluence with one inlet fluid dyed with a fluorophore (fluorescein) and the other containing no fluorophore, to increase the contrast. The video clearly shows the constantly fluctuating fluid interface caused by the obstacles within the mixing channel. The fluid interface between the MeOH and MeOH/H_2O inlet fluids was not stable, but was constantly fluctuating and moving from a central position into the MeOH inlet channel. In all the micromixers studied previously, the interface between the inlet fluids has been stable and shown no fluctuations at the given flow rates, as illustrated in Video 4.1.

Figure 5.16 shows two sequential FLIM images of the confluence zone under identical conditions, displaying two different positions for the fluid interface. The interface moved from the centre of the mixing channel, into the pure methanol inlet channel represented by the red-coloured inlet channel in the FLIM image (Figure 5.16).

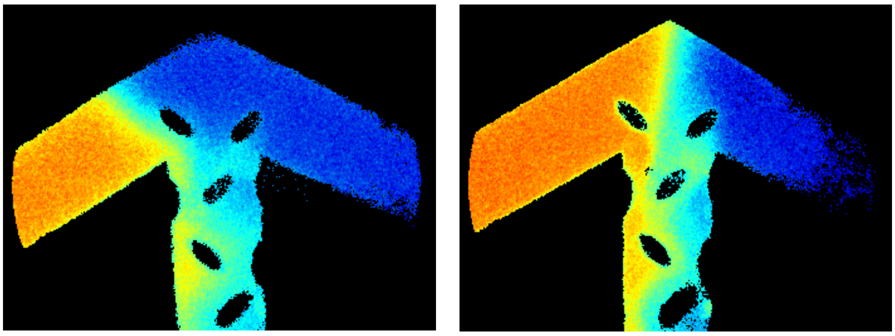

Figure 5.16: Sequential FLIM images of the micromixer E recorded at the entrance of the mixing channel. The images show the changing fluid interface between the inlet fluid streams. Video 5.1 provides an indication of the time scale of fluctuations.

Due to the fluctuating fluid interface a composition profile could not be extracted from the entrance of the mixing channel. Instead a composition profile was extracted from the entrance of the mixing channel of micromixer F, with identical dimensions and geometry, but no obstacles, under identical flow conditions. This enabled the effect of the columns on the mixing of the fluids to be examined.

FLIM images recorded of the entrance of the mixing channel of micromixer E and just after the entrance, to capture the effect of the columns, are displayed in Figure 5.17a and b). A third FLIM image was recorded at the exit of the micromixer to assess if complete mixing was achieved (Figure 5.17c). The composition profiles corresponding to the cross-sections displayed on the FLIM images are presented in Figure 5.18.

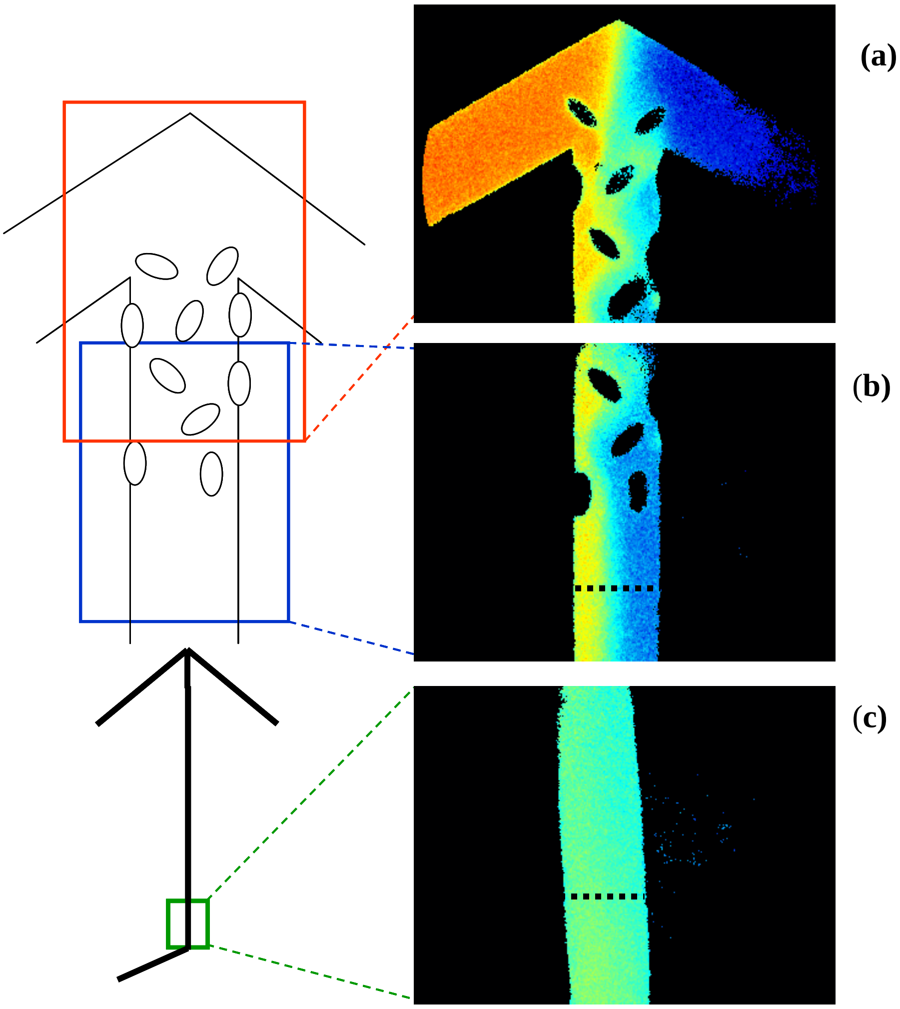

Figure 5.17: The FLIM images recorded of micromixer E at the positions shown in the corresponding diagrams: **(a)** at the confluence zone, **(b)** just after the entrance of mixing channel, and **(c)** at the end of the mixing channel. FLIM images **b** and **c** show the cross-sections along which the composition profiles were extracted for Figure 5.18.

The fluid composition profile at the entrance of the mixing channel with no obstacles (mixer F) is displayed by the black squares in Figure 5.18, whereas the composition profile of the fluids after passing the obstacles (mixer E) is represented by the red circles. From these profiles, the fluids appear to be slightly more mixed after passing through the columns but a large difference in composition still exists. At the end of the mixing channel the fluids are still not completely mixed as the profile, represented by the blue triangles in Figure 5.18, is not horizontal.

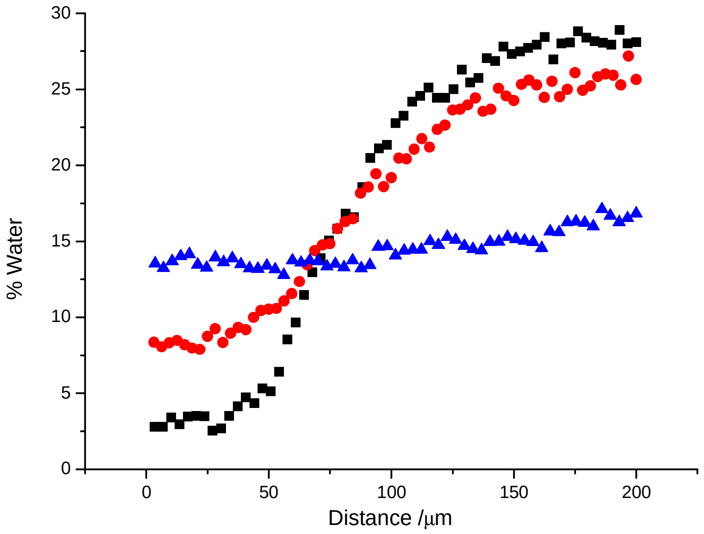

Figure 5.18: Composition profiles for micromixers E and F. The black squares represent the composition profile at the entrance of the mixing channel of micromixer F, which had no obstacles. The red circles represent the composition profile along the cross-section shown in Figure 5.17b of the mixing channel of micromixer E immediately after the obstacles. The composition profile along the cross-section shown in Figure 5.17c, at the end of the mixing channel of micromixer E, is represented by the blue triangles.

The asymmetric layout of the obstacles should distort the fluid flow and offer differential resistance to the flow, with the flow redirected through the route of least resistance.[76] The increased resistance to flow from the obstacles resulted in strong fluctuations of the inlet fluid interface. Fluctuations in micro flows have been exploited to enhance mixing. Glasgow *et al.* (2003 and 2004) demonstrated enhanced mixing from inducing strong flow fluctuations within a T-shaped micromixer.[73;74] Therefore, the slightly increased mixing observed after the obstacles could be the result of flow fluctuations rather than a direct effect of the obstacles. Alternatively, this could be an artefact of the time-averaged image (image acquisition time of 16 s). The large number of obstacles created significant backpressure hence causing the flow fluctuations. A video assembled from the recorded time-gated intensity images used to construct the FLIM image can be viewed in the supplementary CD (Video 5.2). This shows the fluid interface fluctuating during the 16 s acquisition time. Hence, the FLIM image will be an 'average' of these fluctuations. This micromixer presents a situation where video-rate FLIM would be beneficial to probe the effect of the fluctuations on mixing, as the obstacles may appear to increase mixing in a time-averaged FLIM image.

5.3.7 Confocal FLIM images

A confocal FLIM setup was used to optically section through the micromixers to provide 3D imaging of mixing through the use of confocal imaging techniques coupled with photon counting equipment and software (Becker & Hickl). Figure 5.19 shows a selection of confocal FLIM images recorded at a range of depths through the confluence zone of the one of the Epigem micromixers. This micromixer labelled G has identical dimension to the micromixer labelled D used previously (Figure 5.12), except the angle of confluence is 120^{o} giving a ↑-shaped junction instead of a Y-shaped junction as in mixer D. The FLIM images were recorded at distances of 10 µm, 35 µm, 85 µm, 125 µm above the bottom surface of the mixer. The images recorded close to the surfaces displays fluorescence lifetimes slightly lower than expected for the MeOH streams, as observed in the images recorded at 10 µm and 125 µm from the lower surface in Figures 5.19a and d, respectively. In these images the MeOH stream on the left-hand side of the mixer is more of a green colour than the expected red, as observed from the MeOH stream at positions towards the centre of the channel, for example, the images recorded at 35 µm and 85 µm from the lower surface shown in Figures 5.19b and c. This effect demonstrates that the fluorescence emission exhibited by ANS in pure methanol is quenched by the surface of the micromixers, shown by the reduction in the fluorescence lifetime at the surface. ANS in the equimolar water-methanol mixture does not appear to be affected by the surfaces, this as suggested earlier maybe due to the already reduced lifetime by the presence of water. This is not a mixing effect due to a layer of the water-methanol mixture at the surfaces, as the same effect was observed when both inlet fluids were ANS in pure methanol. The MeOH may be leaching a quenching impurity from the plastic.

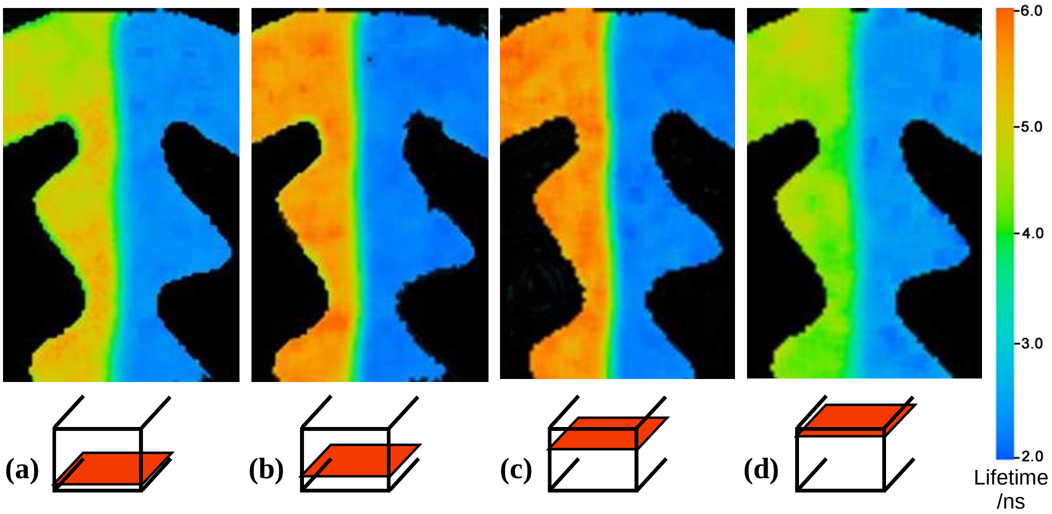

Figure 5.19: Confocal FLIM images of micromixer G with ANS mixing solutions at distances **(a)** 10 µm, **(b)** 35 µm, **(c)** 85 µm, **(d)** 125 µm, from the bottom surface of the mixer. The diagrams below each confocal FLIM image illustrate the relative positions of the optical sections from which data was recorded through the device.

The suggestion of using inlet fluids with lower lifetimes to overcome the quenching effect would be particularly advantageous with the confocal FLIM system as a pulse-picker should be inserted into the laser beam path before exciting the sample to reduce the repetition rate of the laser from 76 MHz to 4.75 MHz (corresponding to times of approximately 13 ns and 210 ns between consecutive laser excitation pulses). The confocal FLIM images presented were recorded with a laser repetition rate of 76 MHz. By changing the two inlet fluid compositions to ensure that the fluorescence has decayed sufficiently between laser excitation pulses, i.e. fluids with lifetimes below ~3 ns, would enable the quantitative use of the confocal FLIM images. Hence, using an equimolar water-methanol mixture and pure water would suffice.

5.4 Conclusion

The FLIM technique has been applied to a selection of commercially available passive laminar flow micromixers. Imaging was achieved through a 0.5 mm polymer layer in comparison with a 0.16 mm optically transparent glass coverslip, used in the simple T-junction flow cell. FLIM faithfully reports the fluid composition, as the lifetime is governed by the solvent environment of the ANS probe, and was proved to be immune to other undesirable optical effects. The effect of the inlet channel geometry, channel dimensions, chambers and serpentine channel designs has been studied using the FLIM technique. In addition, the effect on mixing of asymmetric curves in the vertical channel walls and of obstacles has been explored using the FLIM technique.

Changing the angle at which fluids converge between a Y-shape or a ↑-shape junction appeared to have a negligible effect on mixing at the flow rates employed. A more pronounced effect maybe evident at significantly higher flow rates, but this could not be assessed due to the inability of the fluidic interconnections to sustain high pressures.

Reducing the channel width did achieve complete mixing at the exit of the micromixer, whereas, for an identical volumetric flow rate the fluids were not fully mixed on exiting the micromixer with wider channels. For wider channels it would be necessary to decrease the flow rate, to increase the residence time, to ensure the fluids were fully mixed by diffusion. However, this dramatically reduces the throughput or productivity of mixed fluids, which may not be ideal for the applications intended. Reducing the channel dimension to increase the mixing must be balanced against the increased pressure drop, which may create flow problems and even restrict the flow rate. The increased mixing observed with the reduced channel dimensions was caused by the increased shear rate at the confluence. Reduced channel dimensions are also more susceptible to blockages, although this can be overcome with the use of filters.

The presence of a chamber within the micromixer creates an interesting effect by expanding the mixing region at the fluid interface. However, this has a limited effect on the mixing, as the mixing region is subsequently reduced back to that originally present upon entering the chamber.

Asymmetric curves in the vertical walls of the mixing channel have an insignificant influence on the mixing. They create an effect similar to that observed in the chamber, whereby the mixing region is expanded and reduced several times, but on a smaller scale.

The vertical columns fabricated at the entrance to the mixing channel created a significantly higher pressure drop through the channel, resulting in backpressure causing the fluid interface at the confluence to continually fluctuate. The fluids were more mixed after passing through the obstacles than over the same distance through the asymmetric curved walls. The layout and shape of the obstacles could be optimised to both significantly reduce backpressure and enhance the mixing.

The FLIM technique has successfully evaluated a selection of commercial microfluidic mixers and has the potential to be extended to numerous other micromixer designs. Video rate FLIM using a minimum of two intensity gates is easily achievable with adaptation of the FLIM software, which would be beneficial to probe dynamic mixing strategies. Three dimensional interrogation of micromixing is attainable through the use of confocal imaging techniques coupled with photon counting equipment and software, to acquire FLIM images of optical sections through microfluidic devices. FLIM techniques have now been used by several research groups to investigate microfluidic mixing and its employment is expected to increase due to the significant advantages it offers over other available techniques.

Chapter 6

Temperature measurement within microfluidic devices

6.1 Introduction

The development and use of microfluidic reactors in biological and chemical research has dramatically increased in the past decade due to the benefits of performing reactions at the microscale. The main advantage of miniaturising temperature-dependent reactions is a consequence of the high surface-area-to-volume ratio, which allows increased control of temperature due to the rapid heat-transfer efficiency, this enables quick heating and cooling in reaction chambers with isothermal conditions and well-defined residence times to be achieved.[83] Countless biological processes and chemical reactions require precise temperature control, to guarantee successful yields and to ensure consistent and repeatable performance.[84] The thermal management of microfluidic devices is an extremely important consideration for the design, fabrication and performance of microfluidic devices. Temperature regulation is fundamental for many biological and chemical reactions and processes, yet it can be problematic to accurately measure temperature in extremely small volumes of fluids, for example in microfluidic devices.[85]

6.1.1 Microfluidic chemical reactions

A particular advantage of chemical synthesis in microreactors is the reduction of undesirable temperature-induced side reactions, because isothermal conditions are achieved.[83;86;87] Indeed there have been many reports of higher selectivity, yield and product quality as a result of using microreactors to carry out chemical reactions.[83] Precise temperature control is an important parameter because of the effect of temperature on reaction kinetics.[87] The control of temperature is critical in microreactors where the reaction mixture must be refluxed. Reflux is problematic at such small scales, since the boiling mixture may rapidly expand and can be ejected from the device prematurely.[86] To increase the reaction time, the temperature must be precisely controlled to prevent boiling, but the reaction must be maintained at an optimum temperature, where the reaction efficiency is adequate to produce a sufficient yield.[86] Real-time temperature monitoring would also be beneficial for highly exothermic or endothermic reactions, where the temperature can be altered by the progression of the reaction.

6.1.2 Microfluidic biological processes and reactions

Microfluidics has found numerous uses in biological applications, for many of which precise temperature control is important. Microfluidic devices have proved very successful in handling and manipulating individual biological cells in solution.[88;89] The control of temperature within such devices is critical, as temperature increases of only a few degrees above the physiological temperature can cause the production of cellular heat shock proteins and damage the cells.[90] This can be a major problem for many biological systems in which temperatures may dramatically increase as a result of excessive Joule heating during electroosmotic flow or capillary electrophoresis. This can lead to temperature increases of as much as 20 ^{o}C.[91;92]

DNA hybridization reactions have been performed at 35 ^{o}C and it was found that a constant temperature of ± 1 ^{o}C across the micro-heating chamber was essential to ensure reproducible reaction kinetics.[84] DNA analysis using macroscopic techniques such as gel electrophoresis is difficult to perform with high throughput, as analysis time can exceed several hours for each gel.[93] Lab-on-a-chip devices to perform capillary electrophoresis have been designed to reduce analysis time, and can outperform traditional analysis methods by increasing the separation efficiencies.[93;94] These advantages can be dependent on temperature, which has a limiting effect on the resolution, as excessive temperatures can cause band spreading.[95]

The possibility of using microscopic temperature gradients to separate DNA (thermophoresis) in microfluidic devices as an alternative to capillary electrophoresis has been demonstrated. This can overcome problems such as electrochemical effects at the metal-buffer interface and the time-consuming preparation of gel phases.[96] In addition, microfluidic temperature gradient focusing systems can be used to concentrate and separate proteins as an alternative to isoelectric focusing techniques.[97]

6.1.3 Microfluidic PCR

In the past decade numerous lab-on-a-chip devices have been developed to perform polymerase chain reaction (PCR), an extremely important technique used for the amplification of DNA in molecular biology, chemical and biomedical analysis and diagnosis.[98-100] PCR has been vital to the rapid advances seen in gene diagnostics and genetic identification over the past decade.[101] This reaction is an example of one where temperature control is crucial.

DNA is amplified by PCR through a series of polymerisation cycles which involve the thermal cycling through three temperatures phases; denaturation, annealing and DNA synthesis by a thermostable polymerase. The initial step involves heating the sample to ~95 ^{o}C, which denatures the double-stranded DNA molecules into single stranded molecules. The next step involves cooling to ~55 ^{o}C to allow annealing of primers to the single-stranded DNA template. The final step involves increasing the temperature to ~72 ^{o}C to allow extension of the target DNA in the presence of a polymerisation enzyme and deoxynucleotide triphosphates. This single thermal cycle is repeated many times. The temperature precision of the thermal cycling ideally should be within ± 1 ^{o}C with rapid transition between the different temperatures to achieve optimal amplification and reduction of undesirable products.[83;84;102]

PCR reactions can be exceptionally efficient if optimal conditions are achieved, in particular the annealing temperature is an important parameter.[99] For example, if the annealing temperature is slightly too high, the purity and yield of product can be reduced, whereas too low a temperature can amplify non-specific DNA fragments resulting in the spreading and additional bands when analysing and separating with gels.[99] These effects have been shown with deviations of as small as 1 °C from the optimum annealing temperature.[99]

Conventional PCR requires large volumes of reagents and can take several hours due to the prolonged time required for the temperature to stabilise.[98;103] This can have a detrimental effect on yields as enzyme activities decrease with time.[101] Reducing PCR reactions to the microscale has heralded many advantages. The high surface-to-volume ratio and low thermal mass of sample increase heat transfer efficiency, allowing for rapid thermal cycling.[85;87;98;102] The reduced consumption of reagents and samples is hugely beneficial, as is the ability to establish a uniform temperature distribution throughout the sample.[85;98;100;102] The efficiency of PCR is controlled by accurate and rapid temperature cycling and temperature uniformity which reduces undesirable products.[83;102] These parameters can be attained through the thermal design and experimental validation of prototype micro-PCR devices.

There are two main types of micro-PCR design; continuous-flow, where reagents are continuously cycled, or shuttled through microchannels held at three different static temperatures in different areas of the chip, and chamber-based, where the temperature of a chamber is cycled through the three temperature steps using various heating and cooling strategies. Continuous flow provides a fast amplification time but control of the different temperature regions and process time at each temperature is considerably more challenging.[103] Times as low as 90 s for 20 cycles have been reported for a continuous flow PCR chip.[98] Chamber-based chips are more reliable for controlling the temperature and can be flexible in process time, but are slower overall due to temperature ramping times.[103]

6.1.4 Modelling of temperature in microfluidic devices

Modelling has great potential for optimising the design of heaters and chambers, rather than laborious and time-consuming trial-and-error fabrication techniques, but ultimately it needs to be experimentally verified. It is somewhat surprising to see the reliance of various research groups on using modelling techniques to calculate the temperatures and thermal distribution within heating devices without any experimental calibrations.[98;102] The accuracy of modelling techniques relies on the accuracy of the input parameters and various assumptions are made to simplify the technique, whereas experimental data can provide real and true values.

6.1.5 Temperature measurements in microfluidic devices

Numerous techniques and procedures have been researched and documented for providing temperature measurement within microfluidic devices. The most common methods rely on micro-thermocouples and temperature sensors.[104] There have been numerous reports of how surface-mounted sensors are ineffective at providing reliable temperature information as the surface temperature of a device can greatly differ from the internal temperature of the fluid.[84;86;87;92-94;102] Differences between surface temperature and internal fluid temperature have been reported ranging from 3 °C to 20 °C.[84;92;93] These large temperature errors can be caused by poor thermal contact between the sensor and fluidic device[93], with temperature differences becoming greater as temperature increases.[102] Even attempting to calibrate external sensors by inserting thermocouples directly into chambers can dramatically affect the temperature uniformity and distribution, whilst providing a temperature measurement at only one discrete point.[93;100;102] Thermocouples inserted into devices can perturb the fluid temperature, due to the large thermal capacity compared with that of the channel or chamber, resulting in large errors in the fluid temperature measurement,[103] and can also inhibit certain types of biochemical reactions.[93]

Regardless of efforts to attain and monitor temperature uniformity, problems can still arise from air bubbles produced when temperatures rise above 90 °C, for example while performing PCR.[101;102] Air bubbles can be caused by the evaporation of buffer or by incomplete sealing of the inlet/outlet channels.[101] The air bubbles can cause an unwanted insulation layer, which can inhibit the effective transfer of heat due to the much lower thermal conductivity of air than the PCR buffer, resulting in temperature differences of 4-5 °C.[101] Once bubbles are generated, continued high temperatures will cause bubbles to grow and could eventually completely inhibit PCR due to the lack of convection through the PCR buffer.[101] Sensors and modelling techniques fail to recognise or consider the formation of air bubbles thereby providing potentially false temperature measurements.

6.1.6 Current methods for measuring temperature

Nuclear magnetic resonance (NMR) thermometry has been used to monitor the buffer temperatures during capillary electrophoresis.[105;106] It is well established that Joule heating resulting from capillary electrophoresis can have a significant effect on the temperature of the buffer, which can affect parameters such as the pH of the buffer, reproducibility, separation efficiencies, viscosity, diffusion coefficients, peak shapes and migration times.[105;106] The NMR technique can non-invasively measure temperature within capillaries with sub-second temporal resolution by measuring the shift in the proton resonance frequency of the water signal.[105] A major disadvantage of the technique is the limited spatial resolution of 1 mm due to the probe size.[105]

Raman spectroscopy has been applied to non-invasively and directly measure the buffer temperature for capillary electrophoresis and micro-PCR systems.[95;103;107] Similar to NMR, the technique exploits the temperature dependence of water molecules, in this case the OH vibrational modes. An advantage of the technique is the high spatial resolution of 1 µm. However, the technique is limited temporally by the necessity of recording single-point measurements, which results in high acquisition times, typically 2 s for each point.

Extrinsic Fabry-Perot interferometry has been used as a non-contact technique to calculate fluid temperatures changes within microfluidic devices by measuring changes in the optical path length through microchannels.[108] The technique exploits the temperature dependence of the refractive index of water to calculate the temperature of solutions within microdevices. The optical path length, measured by correlating reflections from the top and bottom surfaces of the microdevice, is directly proportional to the refractive index of the fluid within the device. The refractive index of the fluid is directly dependent on the fluid temperature, showing a decrease as the temperature increases. Complications with this technique include changes in path length due to the thermal expansion of microdevices and low light reflectance, which was overcome by applying a semi-reflective silver coating to the surfaces.

Fluorescence intensity imaging of a temperature-sensitive ruthenium complex, *Tris*(bipyridine)ruthenium(II) $[Ru(bpy)_3]^{2+}$, coated onto one surface of T-shaped micromixer was used to investigate the surface temperature distributions observed from mixing fluid streams of different temperatures.[109] The fluorescent dye was coated onto a microscope cover slip by spin coating to produce a 1 µm thick layer, following which the cover slip was sealed onto the T-shaped mixer. As the measured fluorescence intensity is dependent on the dye concentration and excitation intensity this was acknowledged to create temperature measurement errors due to the problems in the surface dye uniformity and fluctuations in the excitation light source. It was assumed that the surface temperature recorded was representative of the fluid temperatures, which may not actually be true. The ruthenium complex can be used to measure surface temperature over the range 20–60 ^{o}C,[110] therefore it will be unsuitable for PCR temperature calibrations.

Temperature imaging within microfluidic devices using aqueous suspensions of thermochromic liquid crystals (TLC) has been used by various researchers as it is relatively simple to implement.[85;86;100;102] TLC's have been used to measure temperature distributions and to optimise designs for PCR chambers and continuous flow chemical reactors. When illuminated by white light, TLCs change colour depending on the surrounding fluid temperature by selectively reflecting part of the spectrum of incident white light, which is then imaged onto a CCD camera. Once calibrated, the colour image can be converted to a temperature image. TLCs can be highly sensitive within a narrow temperature range and can provide a temperature resolution of ± 0.4 ^{o}C.[86] Problems with the technique include a sensitivity to the illumination method and the optical path through the device, which can distort results.[100] The colour of the reflected light can be dependent on the density of the TLCs in the aqueous solution, which has caused problems imaging at temperatures above 90 °C, due to the evaporation of water, and when imaging near walls.[102] Also, given that the density of TLCs can be greater or less than water, they have a tendency to either sink or float to the top or bottom surfaces, thereby only providing temperature information in these areas.[100] Other problems include the accuracy of temperature measurement based on the technique used for colour to temperature calibration and the non-uniform colour characteristics of TLCs, their temporal response to temperature and the effect of the viewing angle on results.[85] Spatial resolution is reduced due to the large size of TLCs (10-15 µm), which can make them impractical for microfluidic applications.[85;102] Advantages include their temperature sensitivity over a range of -30 to +120 °C, with an actual colour bandwidth over a range from 0.5 to 40 °C.[86] The possibility that TLCs could be encapsulated by an inert material and added directly to reaction mixtures to measure temperature, but not affect the progress of the reaction, could be a great advantage.[86]

A common detection method used for DNA is a fluorescence intensity signal when target DNA binds to a specific probe. However, the binding or hybridization of DNA to the probe is sensitive to temperature, as the DNA duplex can be denatured at specific temperatures.[93] Indeed this problem has been utilised to measure the temperature within microfluidic devices by monitoring the rapid fluorescence intensity decrease or increase at the denaturing or ‘melting’ temperature (T_m) of the duplex, which occurs over a very small temperature range.[87;93;96;111] Typical melting curves are sigmoidal in shape with the T_m defined by the inflection point of the curve.

Molecular beacons are oligonucleotide probes which report the presence of specific nucleic acid sequences by either exhibiting fluorescence when the DNA is hybridised to the beacon, or by quenching fluorescence. If temperature is increased to the T_m, the DNA double strand denatures and separates, thereby increasing or decreasing the fluorescence intensity depending on whether the fluorescent label is no longer quenched or is now quenched. The T_m is very specific and depends on the beacon double strand length and composition, therefore, beacons with a range of temperature sensitivities can be produced. Obtaining a melting curve by increasing temperature and measuring fluorescence intensity can be used to precisely calibrate a microdevice over a very restricted temperature range. The melting curve for single-stranded DNA can actually be used to monitor the product purity and reaction progress during PCR amplification.[111]

The temperature sensitivity of the fluorescent lifetime of fluorescent-labelled DNA oligomers has been evaluated as a means to measure the temperature within ultra small volumes, with applications for microfluidic heating devices.[112] The technique exploits the different efficiency with which DNA bases can quench fluorescence. The distance between DNA bases and a fluorophore is modulated due to the conformational changes of the DNA chain, with the fluorescence lifetime of the fluorophore modulated with conformational changes. As temperature increases, this results in faster conformational changes and shorter fluorescence lifetimes. From measuring the fluorescence lifetime of the fluorophore this can be calibrated and used to calculate the temperature within microfluidic devices. Only temperature changes between 15-35 ^{o}C have been measured by using the average of two lifetimes.[112]

A popular method for temperature imaging and single-point measurements exploits the temperature-dependence of the fluorescence quantum efficiency of rhodamine B (RhB) solutions. The free rotation of diethylamino group in the xanthene chromophore of RhB is the main non-radiative deactivation pathway of the excited state, and is thought to increase the internal conversion from the first excited state to the ground state, leading to a temperature-dependent lifetime.[113] There have been numerous publications reporting the use of the fluorescence intensity of RhB to measure temperature within microfluidic devices as this technique is relatively easy to implement using a standard fluorescence microscope, mercury excitation lamp and CCD camera.[90;92;94;97;114]

The temperature gradient induced in a microchannel has been calculated using measurements of RhB fluorescence intensity while simultaneously measuring the intensity of an internal reference (a second fluorophore) to account for laser intensity and photobleaching effects.[97] However, this did not take into account that photobleaching effects could be different for each fluorophore. Temperature gradients for microscale thermophoresis have been calculated by imaging the fluorescence intensity of tetramethylrhodamine (TAMRA).[96] However, the ability of fluorescence intensity-based techniques to provide accurate temperature information of fluids in microfluidic systems is severely compromised by their sensitivity to variations in the optical path, instability of the light source, scattering, uncertainty in the dye concentration, and photobleaching effects.[18]

Problems have been reported with RhB adsorbing onto the surfaces of certain plastics and not being removed even after repeated rinsing.[94] When using fluorescence lifetime imaging or intensity imaging this can be a problem because the temperature dependence of the adsorbed molecule may be different to that in the bulk solution.[94] This could limit the applicability of RhB-based temperature mapping.

6.1.7 Fluorescence lifetime measurements of temperature

The sensitivity of the fluorescence lifetime of a molecule to its surrounding environment, including temperature, provides an alternative method for temperature profiling of fluids in microfluidic devices. Fluorescence lifetime measurements have the advantage that they are insensitive to the problems that can affect intensity-based measurements (see above).

Kitamura *et al.* 2003 and 2004 performed single-point fluorescence lifetime measurements of RhB in aqueous and methanoic solutions separately, to measure the temperature within microchannel-heating devices.[115;116] The lifetime of RhB in methanol was recorded at five positions along a 1100 µm section of microchannel, with a minimum of 100 µm between subsequence positions. Methanol was used rather than water, as this was the solvent in which the chemical micro-reaction would be performed. Twelve single-point lifetime measurements using aqueous RhB were also recorded along a 600 µm section of microchannel. The disadvantage of using single-point lifetime measurements for temperature profiling in microfluidic devices is the extremely low spatial resolution of temperature variation that is provided.

Benninger *et al.* have used FLIM techniques to image the temperature of RhB in methanol within a glass microchip, designed to perform continuous-flow PCR reactions.[104] It is surprising that methanoic solutions of RhB have been used to measure temperatures up to 95 ^{o}C, as this is considerably higher than the boiling temperature of methanol (*ca* 65 ^{o}C) [117] and will induce reflux problems previously mentioned. The disadvantage of the technique is acknowledged by the authors who state the benefits of performing aqueous-based temperature measurements. Temperature profiles through the heating chip were obtained from the average lifetimes calculated from a number of entire FLIM images, recorded at various positions along the microchannel. The individual FLIM images displayed were relatively noisy and provided limited spatial resolution of temperature. To achieve the quoted temperature resolution of ± 1 ^{o}C, relied on using the average lifetime over the entire FLIM image. 3D temperature imaging was performed using multiphoton excitation to provide confocal FLIM images of optical sections through the microchannel. The temperature data acquired from the confocal FLIM images is noisy and displays large temperature fluctuations between subsequent data points. The low-NA objectives used in this study reduced the signal intensity and increased the noise of data collected. It was suggested that the use of high-NA objectives could overcome this problem.

6.1.8 Aqueous polymer probes to measure temperature

Imaging temperature within microfluidic devices can be achieved using polymer probes which exhibit a sharp phase transition at a specific temperature, the lower critical solution temperature (LCST) of the polymer. Aqueous solutions of poly(N-isopropylacrylamide) (PNIPAM) with a LCST of 32 ^{o}C have been used within microfluidic heating devices to image and indicate when the solution within a microchannel is above or below 32 ^{o}C.[11;90] Below 32 ^{o}C aqueous PNIPAM is completely transparent but when the temperature increases to above 32 ^{o}C the polymer undergoes a temperature-induced phase transition resulting in the precipitation of the polymer. The precipitate of the polymer has be optically imaged within microchannels using a transmission microscope and CCD camera set-up, however, problems resulted with distinguishing between the precipitation region and that of the transparent solution.[90;115] Fluorescence intensity imaging was achieved using an aqueous mixture of PNIPAM and Acridine Orange (this fluorophore exhibits strong fluorescence in hydrophobic conditions).[11] At 32 ^{o}C the polymer changes from hydrophilic (hence dissolved in water) to hydrophobic (precipitates out of water) and the fluorophore which has accumulated within the hydrophobic particles exhibits fluorescence.[115]

Polymers of *N*-alkylacrylamide labelled with a fluorophore have been developed as fluorescent molecular thermometers which are extremely sensitive to temperature.[118-120] The reproducibility of the molecular response was tested and shown to have an active temperature sensitivity when the temperature was reversed with a small hysteresis effect.[118] The polymers labelled with benzofuran gave the largest reported enhancement in fluorescence intensity within a narrow temperature range, typically of 6-7 °C.[118-120] The N-alkylacrylamide polymers in aqueous solution undergo a phase transition above their LCST, causing a considerable change in microenvironmental polarity in the vicinity of the main polymer chain. By copolymerising a fluorophore which is polarity-sensitive with the N-alkylacrylamide, a temperature sensor can be produced, in which the polarity changes from the thermal-induced phase transition have a strong effect on the fluorophore fluorescence. The fluorescence intensity of benzofuran increases with decreasing solvent polarity, therefore, it is effective in reporting the polymer phase change.[121] A major benefit of this technique is the ability to change the temperature-sensitive range with the availability of other N-alkylacrylamide polymers, which have different LCSTs. Also, by co-polymerising two different N-alkylacrylamide polymers the temperature sensitive range can be adjusted to between 18 and 54 °C by varying the ratio of the polymers.[119] Additional tuning of the temperature range can be achieved by the addition of different organic solvents.[118] Although only polymers with temperature sensitivity in the range of 18-54 ^{o}C have been synthesised, it is potentially possible to develop fluorescent molecular thermometers for higher temperatures and extended sensitivity ranges by using a selection of polymers with temperature induced phase transitions above 50 ^{o}C.[119] It is worth noting that the polymers are not limited to completely aqueous solutions but can also function as fluorescent thermometers when dispersed in water as microgel particles.[122]

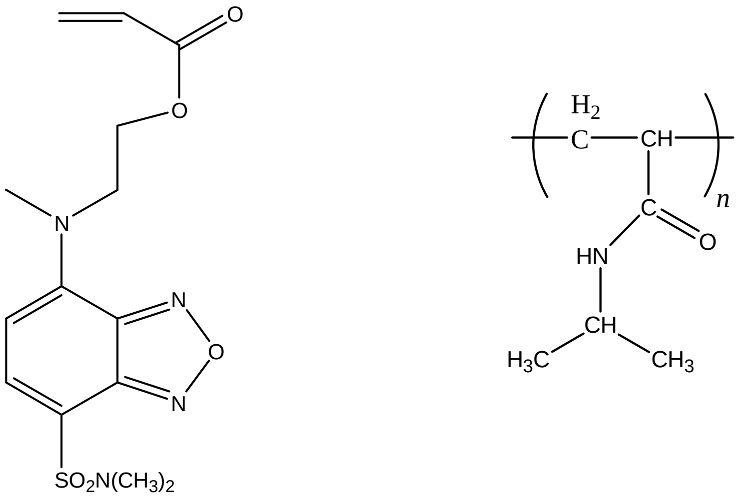

(a) **(b)**

Figure 6.1: Chemical structure of **(a)** DBD-AE, **(b)** PNIPAM

Of the different benzofuran monomers investigated, the most sensitive molecular thermometers of this type have incorporated benzofuran DBD-AE, full name 4-N-(2-Acryloyloxyenthyl)-N-methylamino-7-N,N-dimethylaminosulfonyl-2,1,3-benzoxadiazole (Figure 6.1a).[118-120;122] DBD-AE is not intrinsically sensitive to temperature, which means the intensity change or response is solely caused by the temperature-induced phase transition of the polymer.[118] This is notable, as many fluorophores display a decrease in fluorescence intensity with increasing temperature due to an increase in the contribution of non-radiative relaxation pathways.[90]

In this chapter, a copolymer of DBD-AE with N-isopropylacrylamide (NIPAM) has been investigated as a possible FLIM probe of temperature in microfluidic devices. Poly-NIPAM (PNIPAM, Figure 6.1b) undergoes a phase transition in aqueous solution with a LCST of ~32 °C,[123] and the copolymer with DBD-AE, poly(DBD-AE-co-NIPAM), has been shown to exhibit a 13.3-fold increases in fluorescence intensity between 29 and 37°C.[118] The emission spectra of the polymer was observed to blue-shift by 30 nm as the temperature increased, which would be expected as benzofurazans show a hypsochromic spectral shift with decreasing polarity of solvent.[119-121] In previous studies, the ability of these polymers to function as fluorescent molecular thermometers was studied using steady-state fluorescence spectroscopy.[119-121] In the present work, the response of the fluorescence lifetime of poly(DBD-AE-co-NIPAM) in aqueous solution to temperature has been studied. To complement this study, the use of Kiton Red, a RhB based dye, as a FLIM temperature probe has also been investigated.

6.2 Experimental Details

6.2.1 Solution preparation

The copolymer, poly(DBD-AE-*co*-NIPAM) was received from A. P. de Silvas, having been prepared according with reference.[118] It was used as an aqueous solution of concentration 0.2% w/v. Kiton Red was obtained from Exciton Ltd and used as received. It was used as an aqueous solution of concentration 10^{-3} M. Both solutions were prepared using HPLC grade water (Fisher Scientific, used as received), and stored in the dark. The fluorescence lifetime was used as a routine check of sample purity after storage. No fluorescence emission, at the wavelengths employed, could be detected from the solvents under the instrumental conditions used.

6.2.2 Microfluidic heating system for poly(DBD-AE-co-NIPAM)

A moulded polymer-based microfluidic chamber (provided by Lab 901 Ltd) was filled with poly(DBD-AE-co-NIPAM) solution. Information on the details and dimensions of the equipment provided by Lab901 is restricted due to commercial sensitivity. The solution was injected (from a 1 ml Luer syringe fitted with a 0.4 mm diameter needle, both from BD) through an inlet channel to fill the chamber. The inlet and outlet channels were then heat-sealed. A temperature gradient was achieved by applying parallel heating and cooling elements at either side of the chamber. The left-hand side of the chamber was heated by contact with nichrome wire element (0.71 mm diameter). The temperature of the wire was controlled by varying the voltage supplied using a DC power supply (Thander TS3022). A cold sink was achieved at the right-hand side of the chamber through contact with a copper rod, cooled with ice packs. The cold sink and parallel heat source created a linear temperature gradient across the chamber.[111]

6.2.3 Microfluidic heating system for Kiton Red

A T-shaped flow cell, as described in Section 4.2.2, was used in these experiments. Two input streams of Kiton Red solutions, each held at a different temperature, were mixed. One inlet stream was heated by an electrically heated coil of nichrome wire around the inlet tube, temperature controlled as previously detailed. The other inlet fluid remained at room temperature (22 ^{o}C). The flow of fluids from the syringes (3 ml Luer-lok, BD) was controlled by a syringe pump (KDS200, KD Scientific).

6.2.4 PCR heating system

A series of eight polymer-based micro-PCR chambers (provided by Lab 901 Ltd) were filled with Kiton Red solution. The solution was injected (from a 1 ml Luer syringe fitted with a 0.4 mm diameter needle, both from BD) through an inlet channel to fill each of the chambers. The inlet and outlet channels were then heat-sealed. The series of chambers was mounted into a temperature controlled PCR heating device, manufactured by Lab 901 Ltd.

6.2.5 Fluorescence lifetime imaging (FLIM)

The experimental system for FLIM measurements has been described fully in Section 3. Here, experimental details specific to this study are presented. Excitation laser radiation of wavelength 430 nm was reflected from a dichroic filter (DM455, Nikon) and focused into the microfluidic devices using either 4x (PA, NA=0.2), 10x (PA, NA=0.45), 20x (PA, NA=0.75), 40x (PF, NA=0.60) or 50x (LU Plan, NA=0.80) Nikon objectives. The resultant fluorescence was collected through the same objective, passed through a band pass filter (590 nm, Nikon) and imaged onto the CCD camera. The experiments described herein were recorded with either a 300 or 600 ps gate width, which was measured by detecting laser light reflected from a mirror. Images were the average of 5 separate exposures employing 4 x 4 binning. The details of gate width, threshold counts, number of images recorded, number of averages, CCD exposure time and total acquisition time for each FLIM image recorded is presented in Table 6.1. Each intensity image was the average of 5 separate exposures, the acquisition time of each of which was the sum of the CCD exposure time plus the 50-ms camera readout time. The excitation intensity was adjusted to give a peak intensity of between 3000 and 4000 counts in the brightest image, which corresponds to the start of the fluorescence decay. The instrument response function (IRF) was recorded, by using a mirror in place of the sample, for each of the gate widths used. It was thus established that the fluorescence decay could be fitted from 0.4 ns or 1 ns after the emission peak image, for Kiton Red or poly(DBD-AE-*co*-NIPAM), respectively, without distortion by the instrument response. The images were analysed by constructing a decay curve for each pixel. Pixels with low counts in the first analysed image were removed by adjusting the threshold. A lifetime map was produced by assigning a colour on a 16-bit pseudocolour scale to each of the fitted lifetimes.

	Objective	Gate width /ps	Number of images recorded	Number of averages	CCD exposure /ms	Total acquisition time /s	Threshold counts
Figure 6.4a	x4	600	102	5	200	127.5	670
Figure 6.4c	x40	600	51	5	120	43.4	500
Figure 6.5a	x50	600	51	5	100	38.3	500
Figure 6.5c	x20	600	51	5	50	25.5	500
Figure 6.9a	x20	600	20	5	50	10.0	350
Figure 6.9b	x20	600	82	5	50	41.0	500
Figure 6.15	x20	600	63	5	60	34.7	400
Table 6.5 55 °C	x10	300	52	5	60	28.6	500
72 °C	x10	300	64	5	70	38.4	500
95 °C	x10	300	50	5	70	30.0	500
Figure 6.19	x10	300	50	5	70	30.0	500
Figure 6.20a	x10	600	31	5	450	77.5	500
Figure 6.20b	x10	600	91	5	450	227.5	500
Figure 6.20c	x10	600	91	5	500	250.3	500

Table 6.1: Acquisition times for the FLIM images.

6.2.6 Time-resolved fluorescence spectroscopy (TCSPC)

The temperature dependence of the fluorescence lifetimes of Kiton Red and poly(DBD-AE-*co*-NIPAM) solutions were determined by time-correlated single photon counting on Edinburgh Instruments. Aerated aqueous solutions were contained in a 1 cm pathlength fused silica cuvette (10 x 10 mm inside dimensions) and a 1 cm pathlength fused silica micro-cuvette (10 x 2 mm inside dimensions) for Kiton Red and poly(DBD-AE-*co*-NIPAM) solutions, respectively. The temperature of the solutions was controlled by circulating water from a thermostatically controlled water bath (Grant LTD6) through the cuvette holder. The temperature was measured with a thermocouple (Hanna Instruments HI93530) immersed directly in the sample cuvette. The temperature of the solution was monitored until a constant value was attained.

Fluorescence was excited at 430 nm and decay curves recorded at emission wavelengths 580 and 585 nm for the poly(DBD-AE-*co*-NIPAM) and Kiton Red solutions, respectively. An emission filter (Schott) was required when recording the fluorescence decays of poly(DBD-AE-*co*-NIPAM), to eliminate light scattered by the polymer molecules.

Fluorescence decay curves were recorded into 4096 channels and accumulated to 10,000 counts in the peak channel on time ranges of 20 ns and 100 ns ranges for Kiton Red and poly(DBD-AE-*co*-NIPAM), respectively. The fluorescence decay curves were analysed by tail-fitting (i.e. without convolution with the instrument response function), from 0.4 ns and 1 ns after the peak of the decay for Kiton Red and poly(DBD-AE-*co*-NIPAM) solutions, respectively, to correspond to the conditions used to fit the FLIM decays.

Discrete decay analysis was performed with the F900 (Edinburgh Instruments) software, whilst global analysis was performed using the FAST software package (Alango).

6.3 Results and discussion

6.3.1 Time-resolved fluorescence spectroscopy of poly(DBD-AE-*co*-NIPAM)

The time-resolved fluorescence of poly(DBD-AE-*co*-NIPAM) was studied using time-correlated single-photon counting (TCSPC), with an excitation wavelength of 430 nm. The benzofuran emission was detected at an emission wavelength of 585 nm, over a temperature range of 22.9 to 38.3 ^{o}C. The fluorescence decay of poly(DBD-AE-*co*-NIPAM) was fitted to a multi-exponential decay function, as shown by equation 6.1. Three lifetime components were required to give a satisfactory fit to the experimental data.

$$I(t) = \sum_{i=1}^{n} A_i \exp\left(\frac{-t}{\tau_i}\right) + B \qquad \text{Equation 6.1}$$

where τ_i is the fluorescence lifetime, A_i, the "A-factor", is the fractional amplitude of the ith decay component, and B is the background. The A-factor indicates the fraction of the emitting molecules that has a particular lifetime, τ_i.

The lifetimes (τ_i), their fractional amplitudes (A_i), and the average lifetime, are shown in Table 6.2. The average lifetime is given by: $\tau_{av} = \frac{\sum A_i \tau_i}{\sum A_i}$

Temperature	Lifetimes /ns			Fractional Amplitudes				
/^{o}C	τ_1	τ_2	τ_3	A_1	A_2	A_3	τ_{av}	χ^2
22.9	1.80	3.77	11.06	0.55	0.40	0.05	3.03	1.04
29.1	1.85	4.03	11.60	0.51	0.42	0.07	3.46	1.05
30.5	1.89	4.09	11.64	0.50	0.43	0.07	3.53	1.06
31.1	1.83	4.10	12.74	0.44	0.46	0.10	3.97	1.07
31.6	1.94	4.49	14.47	0.43	0.38	0.19	5.33	1.19
31.9	2.10	5.92	15.39	0.39	0.30	0.31	7.36	1.08
32.2	2.33	7.40	15.67	0.25	0.27	0.48	10.13	1.07
32.7	2.10	7.16	15.53	0.16	0.28	0.56	11.00	1.06
33.1	2.47	7.95	15.68	0.12	0.29	0.59	11.84	1.04
33.7	2.24	8.23	16.20	0.09	0.31	0.61	12.55	1.01
34.3	2.36	8.21	15.66	0.06	0.29	0.64	12.64	1.00
34.7	2.50	8.53	15.71	0.06	0.30	0.64	12.77	1.02
35.2	2.33	7.55	15.37	0.03	0.26	0.71	12.90	1.05
36.3	2.91	9.09	16.29	0.05	0.32	0.64	13.37	1.00
37.3	2.32	8.35	15.99	0.03	0.28	0.69	13.41	1.05
38.3	3.26	8.04	15.95	0.01	0.29	0.70	13.51	1.03

Table 6.2: Fluorescence lifetimes (τ_i), their fractional amplitudes (A_i), and the average lifetime of poly(DBD-AE-*co*-NIPAM) as a function of temperature. The goodness of fit parameter, χ^2, is also shown.

The dependence of the average lifetime on temperature is plotted in Figure 6.2. The average lifetime increases from 3.03 ns at 22.9 °C to 13.51 ns at 38.3 °C. There is a quasi-sigmoidal relationship between temperature and lifetime, which is similar to that reported for the temperature-intensity relationship.[118] The strong dependence of the average lifetime on temperature enables poly(DBD-AE-*co*-NIPAM) to be used in conjunction with the FLIM technique as a sensitive probe of temperature.

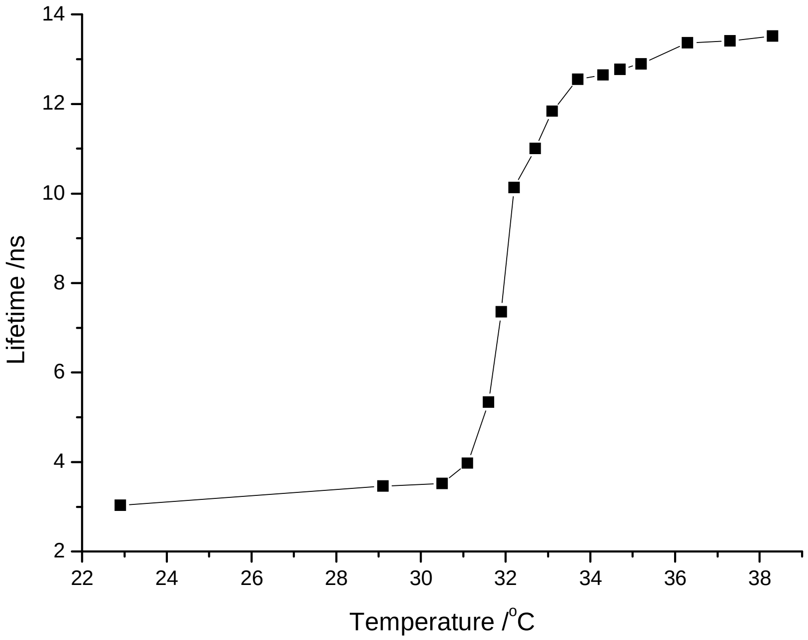

Figure 6.2: Dependence of the average lifetime of poly(DBD-AE-*co*-NIPAM) on temperature.

Examination of the decay parameters in Table 6.2 reveals that the dependence of average lifetime on temperature arises primarily from the variation of the amplitudes A_1 and A_3. A_1 decreases sharply with increasing temperature, with A_3 showing a reciprocal increasing trend. The results in Table 6.2 suggest that the values of all three lifetime components also depend on temperature. However, this could be because of the correlation between the fitting parameters which can occur as an artefact in multi-exponential fitting. To determine whether the decays can, in fact, be described by three temperature-independent decay times, with only the amplitudes depending on temperature, global analysis was undertaken.

Global analysis was preformed by simultaneously fitting all of the decays (obtained at different temperatures) with common lifetimes and variable fractional amplitudes. The results from the global analysis are given in Table 6.3.

Global lifetimes: τ_1 = 2.16 ns τ_2 = 6.02 ns τ_3 =15.1 ns
Global χ^2 = 1.026

Temperature /^{o}C	A_1	A_2	A_3	Local χ^2
22.9	0.88	0.11	0.01	1.00
29.1	0.82	0.17	0.01	1.04
30.5	0.81	0.18	0.01	1.04
31.1	0.77	0.20	0.03	1.07
31.6	0.70	0.20	0.10	1.12
31.9	0.57	0.22	0.21	1.05
32.2	0.34	0.23	0.43	1.04
32.7	0.24	0.25	0.51	1.04
33.1	0.14	0.27	0.59	1.04
33.7	0.14	0.19	0.67	1.06
34.3	0.03	0.28	0.69	1.02
34.7	0.01	0.29	0.70	1.04
35.2	0.00	0.30	0.70	1.06
36.3	0.05	0.19	0.76	1.05
37.3	0.03	0.19	0.78	1.05
38.3	0.02	0.20	0.78	1.04

Table 6.3: Decay parameters obtained from global analysis of the poly(DBD-AE-*co*-NIPAM) decay data.

The global analysis of poly(DBD-AE-*co*-NIPAM) demonstrates that the decay is well fitted by three temperature-independent lifetimes: 2.16, 6.02 and 15.1 ns. Thus the photophysical behaviour of poly(DBD-AE-*co*-NIPAM) can be interpreted in terms of three distinct emitting species which coexist over the measured temperature range. The temperature dependence of the amplitudes of the three decay components is represented graphically in Figure 6.3.

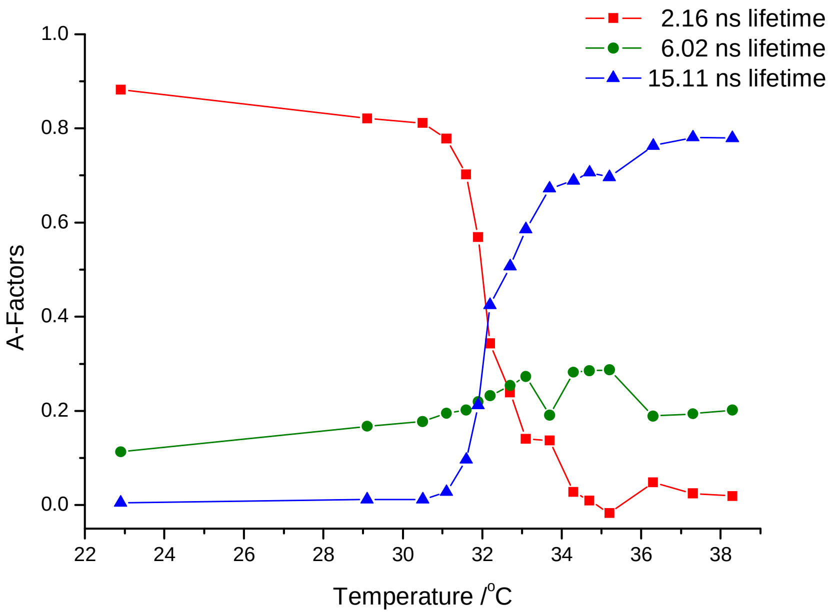

Figure 6.3: Temperature dependence of the A-factor value of each global lifetime of poly(DBD-AE-*co*-NIPAM).

The contribution of the 6.02 ns component is relatively constant with temperature and represents only a small proportion of the overall decay (10-20%). In contrast, it is clear from Figure 6.3 that the contribution of the other two components depends considerably upon the temperature of the aqueous solution. At low temperature, before the phase transition has occurred, the short lifetime component of 2.16 ns predominates (80-90%), and the long component of 15.1 ns is negligible (< 1%). As the temperature is increased, the contribution of the 2.16 ns component decreases, whilst that of the long lifetime component (15.1 ns) increases. At the phase transition of 32 °C, the contribution of these two components is almost equal, whilst above this temperature, the 15.1 ns component now predominates (~80%), and the 2.16 ns lifetime is now decreased to only 1% of the total.

This is good evidence that the spectral and intensity changes that are observed upon changing the temperature are due to the benzofuran experiencing two microenvironments; at low temperature the benzofuran is in a polar, hydrophilic environment with a lifetime of ~2 ns, whilst at higher temperature the phase transition leaves the benzofuran predominately in a different non-polar, hydrophobic environment with lifetime of ~15 ns. The spectral changes observed when this polymer is heated must also be due to these two distinct environments. The fluorescence intensity has been observed to show a 13.3-fold increase between 29 and 37°C,[118] and can be accounted for by the increased formation of the longer lifetime component. The observed blue-shifting of the emission spectra by 30 nm with increasing temperature could also be explained by the rise and fall of the population of the long and short lifetime components, respectively. The emission maximum of the longer component could be blue-shifted by 30 nm in comparison with that of the shorter component. The third lifetime component must represent an intermediate environment for the benzofuran molecule or could possibly be an impurity.

Although this TCSPC data has been fitted using three discrete lifetimes, a more complex model, for example a distribution of lifetimes or stretched exponential may be physically more realistic.[124] However, since the data are well described mathematically by three discrete components, the average lifetime calculated from these discrete components can be used as a reliable measure of temperature.

6.3.2 Fluorescence lifetime imaging of poly(DBD-AE-*co*-NIPAM)

Fluorescence lifetime imaging microscopy (FLIM) of poly(DBD-AE-*co*-NIPAM) has been used to produce temperature maps, with sub-degree temperature resolution within microfluidic heating devices. The temperature-induced phase transition of aqueous NIPAM polymer solutions has only previously been imaged within microfluidic devices using transmission and fluorescence intensity techniques.[11;90] The information from these images was used to indicate regions above or below the phase transition temperature. No quantitative temperature information was extracted from these intensity or transmission images.

6.3.2.1 Comparison of FLIM and intensity images

Figure 6.4a shows the FLIM image of the entire chamber obtained using a 4x objective. The temperature increases across the chamber from the right-hand side to the left-hand side. The FLIM image clearly shows the temperature gradient across the chamber over the temperature range of 32-34 ^{o}C, indicated by the sharp change represented by the transition between the blue and red regions. The area represented by red indicates temperatures above 34 ^{o}C, whereas, the dark blue region indicates temperatures below 32 ^{o}C. The FLIM images are the result of fitting the fluorescence decay per pixel, to a single exponential lifetime and hence only give an approximate indication of temperature. However, individual regions of interest have been analysed and fitted with three lifetimes, to give a quantitative measure of temperature. As the temperature increases from right to left, the average fluorescence lifetime of the polymer changes from ~4.5 ns, represented by dark blue (Figure 6.4a), through a narrow vertical region with a wide range of lifetimes, to a average lifetime of ~13.8 ns, represented by red. The average lifetime of the red area was 4.53 ns, corresponding to 31.4 ^{o}C. While the average lifetime of 13.83 ns within the blue area, corresponds to temperatures above 38 ^{o}C where the response of the probe becomes flat. At the right-hand side of the chamber, where the cold sink is in contact, the temperature increases near the wall, as shown by the light blue and yellow areas at the edge of the chamber. This is due to the chamber material conducting heat around its perimeter and hence increasing the fluorescence lifetime of polymer.

Figure 6.4b shows the fluorescence intensity image for comparison. Red indicates the highest intensity and blue the lowest intensity. Large variations in intensity across the field of view distort the image, with the highest intensity region located where the temperature exceeds 34 ^{o}C. There is no clear indication of the temperature gradient and it would be impossible to extract accurate temperature information. In contrast, the FLIM images give a clearly resolved, quantitative temperature map.

The temperature variation can be resolved in the range where the lifetime of the probe responds strongly, that is between ~30.5 ^{o}C to ~33.5 ^{o}C (Figure 6.2). Temperatures outside this range cannot be accurately measured, as the lifetime is less dependent on temperature. The temperature region where the probe is most sensitive has been expanded, by imaging with a 40x magnification objective, and the FLIM and intensity images are shown in Figure 6.4c and d, respectively. In the FLIM image, the average lifetime changes gradually across the field of view from 10.52 to 5.44 ns, corresponding to a temperature change from 32.4 to 31.7 ^{o}C. The intensity image (Figure 6.4d) shows little contrast change across the field of view and no distinguishable temperature gradient can be observed.

The intensity images were constructed by summing all the time-gated intensity images, to allow a direct comparison between the time-resolved and intensity-based methods. There should be a clear correlation between the intensity images and the lifetime images, as the higher the intensity, the higher the quantum yield and hence the longer the lifetime. There is clearly no such correlation as the intensity images do not give an accurate picture of the temperature distribution because of problems such as an uneven field of illumination, differences in optical path across the image and variations in the density of chamber material imaged through.

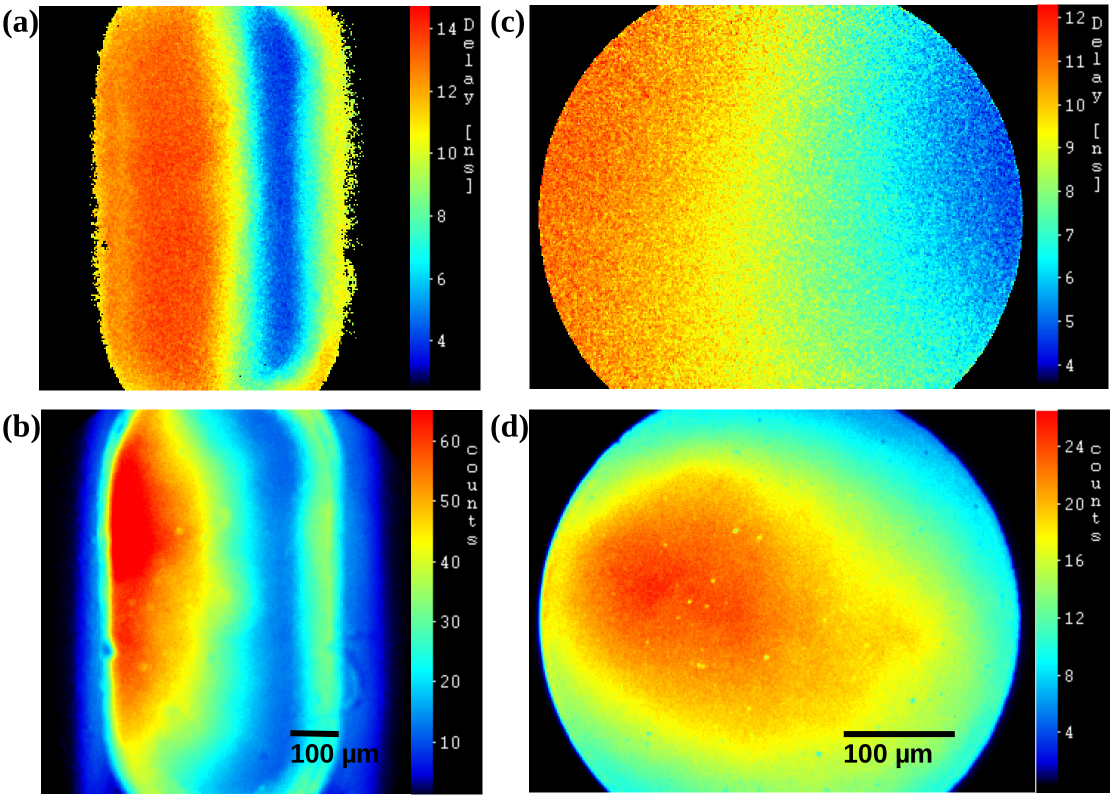

Figure 6.4: Comparison of FLIM images and corresponding intensity images. **(a)** FLIM image showing the entire microfluidic chamber imaged using a 4x magnification objective. **(b)** The corresponding intensity image of **a**. **(c)** FLIM image of the central region imaged using a 40x magnification objective. **(d)** The corresponding intensity image of **c**.

6.3.2.2 High resolution temperature mapping

Figure 6.5a and c show FLIM images acquired using a 50x and 20x magnification objectives, respectively. The acquisition time can be significantly reduced by changing to a higher magnification objective with an increased numerical aperture (NA) value. This decreases the CCD exposure time and also increases the signal-to-noise ratio. Acquisition times for all the FLIM images are displayed in Table 6.1. Temperature profiles have been determined along the cross-sections shown and are plotted in Figure 6.5b and d, respectively. The measured average lifetime at each point in the profile was converted to temperature using the third order polynomial calibration function shown in Figure 6.6.

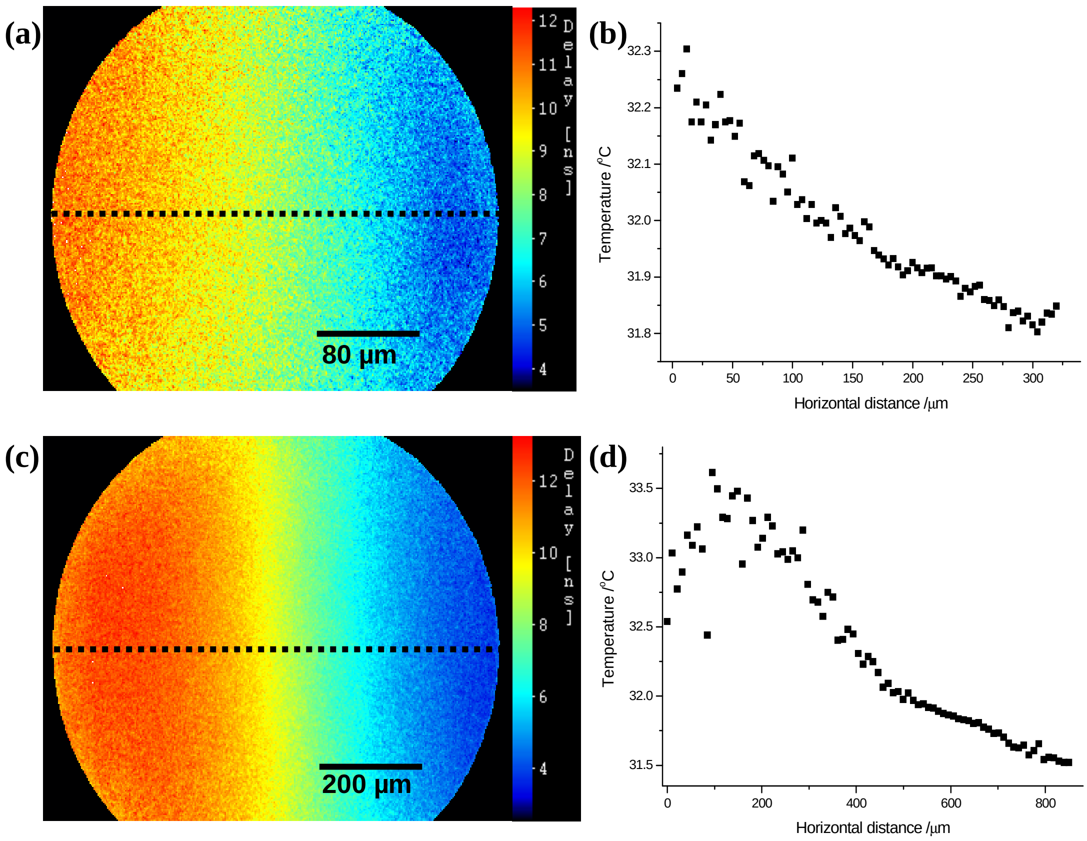

Figure 6.5: FLIM images of the region of interest using **(a)** 50x and **(c)** 20x magnification objective. **(b)** Temperature profile along the cross-section indicated in **a**. **(d)** Temperature profile along the cross-section indicated in **c**.

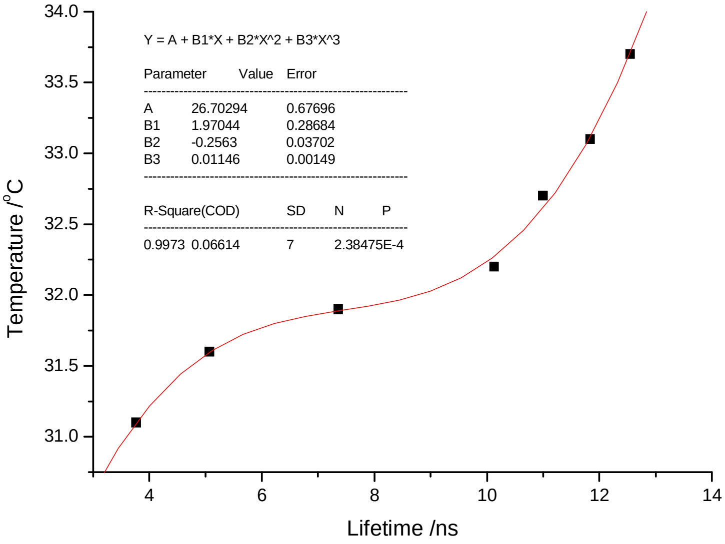

Figure 6.6: The calibration curve relating the average lifetime of poly(DBD-AE-*co*-NIPAM) to temperature was obtained by fitting a third-order polynomial to the TCSPC data (Figure 6.2) over the range in which temperature changes could be resolved. The equation $y = 26.70294+1.97044x-0.2563x^2+0.01146x^3$ gave a good fit to the data.

The temperature profiles were created by extracting and averaging (10 vertical by 4 horizontal pixels) the intensity counts along the cross-sections shown for all the time-gated intensity images. This provided approximately 80 data points along the cross-section for each intensity image. For each data point, the intensity counts were exported and multi-exponential fluorescence decays were fitted using F900 software. The data was fitted to two exponential decays, rather than three, as there were insufficient data points to resolve three decay components. Fitting to two rather than three decay components has negligible effect on the average lifetime obtained, as demonstrated below.

The decay curves measured by TCSPC for calibration purposes (Section 6.3.1) can be fitted to two exponential components with acceptable χ^2 values, however, the residuals when visually inspected are much superior when fitted with three exponential components. As an example Figure 6.7 displays the residuals from fitting two and three lifetimes to the TCSPC fluorescence decay data recorded at 31.9 ^{o}C. The residuals for the bi-exponential are significantly non-random at the beginning of the decay, whereas the residuals for the tri-exponential fit are random across the whole decay. The average lifetimes calculated from fitting the 31.9 ^{o}C decay to two and three exponentials are 7.64 ns and 7.36 ns, respectively, while the chi^2 values are 1.290 and 1.078, respectively.

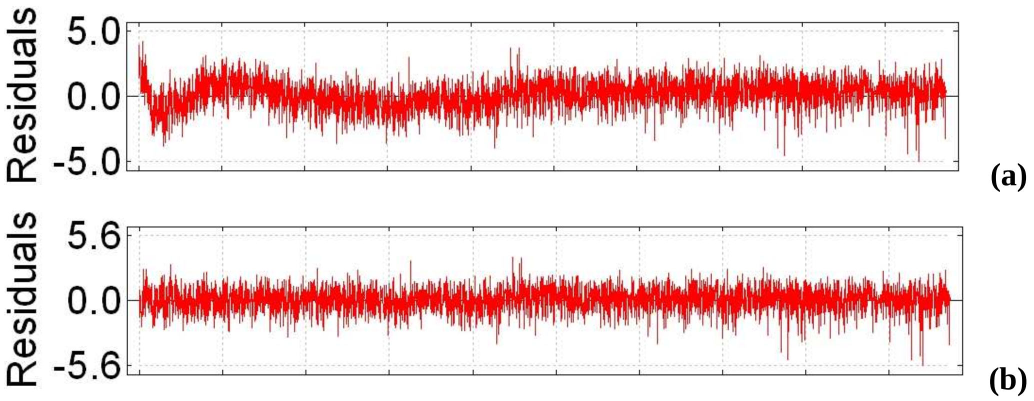

Figure 6.7: The residuals from fitting two (**a**) and three (**b**) lifetimes to fluorescence decay data for poly(DBD-AE-*co*-NIPAM) at 31.9 ^{o}C.

In Figure 6.8 the average lifetimes determined from 2- and 3-component fits are plotted as a function of temperature. It can be seen that across the entire temperature range there is negligible difference between the two alternative average lifetime values.

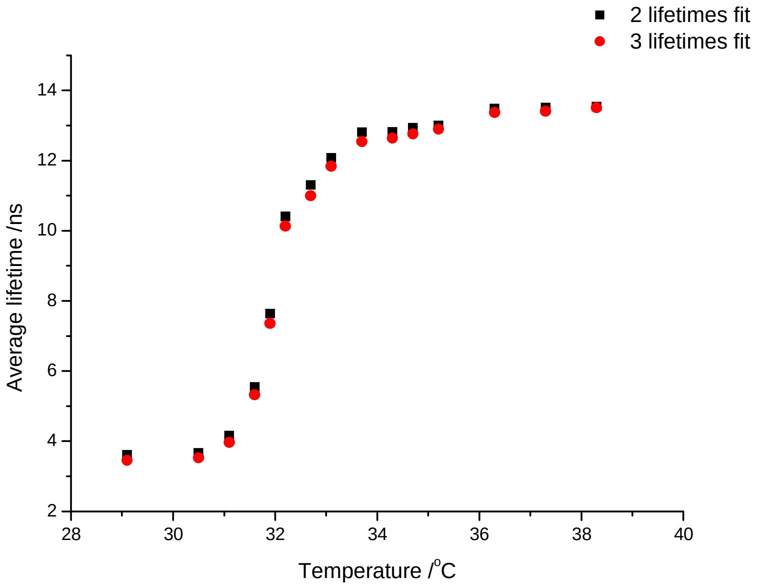

Figure 6.8: The average lifetimes of poly(DBD-AE-*co*-NIPAM) determined by fitting two and three lifetimes plotted as a function of temperature..

The temperature profile obtained at 50x magnification (Figure 6.5b) shows a near-linear temperature gradient from ~31.8 °C to ~32.3 °C, over a total length of 350 µm. This profile demonstrates that a temperature resolution of 0.1°C can be achieved with micrometer spatial resolution and suggests that a temperature resolution of sub-0.1°C is potentially achievable. The resolution could be increased by using higher magnification objectives, decreasing the temporal width of the detection windows, to detect smaller changes in lifetime, and by using photon counting imaging techniques which deliver better lifetime resolution.

The profile obtained at lower magnification, over a greater distance (Figure 6.5d) shows the temperature gradient to be non-linear. Interpretation of this observation is beyond the scope of this thesis. However, work on modelling the thermal properties of microfluidic systems is being carried out by our collaborator Dr David Mendels at the National Physical Laboratory and will be reported in due course.

6.3.2.3 Photobleaching

Poly(DBD-AE-*co*-NIPAM) was found to photobleach significantly during imaging, sometimes resulting in the CCD exposure times having to be increased after several measurements on a single sample. Photobleaching does not affect the lifetimes, therefore, FLIM still provides accurate temperature information. However, photobleaching is a major problem with intensity-based imaging techniques, and is another factor that compromises the performance of such methods.

6.3.3 Conclusions

Polymers of *N*-alkylacrylamide labelled with benzofurans can be used as sensitive molecular thermometers with a resolution of sub-0.1 ^{o}C for mapping temperature within microfluidic devices using FLIM. The high temperature resolution of such probes has much potential in future applications in calibrating and testing the effectiveness of lab-on-a-chip heating devices, where precise temperature control is essential. The FLIM technique provides an effective, non-invasive method to extract accurate temperature information with high spatial resolution. The flexibility of such polymer probes in which the chemical structure can be altered to provide temperature sensitivity over an extended range of 18-54 ^{o}C, makes them suitable to a broad range of applications. The number of applications in which these highly sensitive fluorescent molecular thermometers could be employed, has the potential to be rapidly expanded by the development of polymers with phase transitions above 54 ^{o}C.

These probes could be useful for detecting when temperature exceeds a critical threshold value, for example, the physiological value of 37 ^{o}C which can damage cells. In theory it should be possible to have a solution with a combination of separate polymers synthesised with different LCSTs, either several degrees above, or below an optimal temperature. A FLIM image of a microfluidic device could then be produced to spatially map where and when the temperature veered into critical or sub-optimal ranges with high accuracy. This approach could be beneficial to evaluating optimum temperature conditions in high-throughput microarrays. Currently, at most a single temperature sensor is mounted onto an array plate to provide an indication of temperature within the microarrays. This only gives a single point measurement and provides no information of the temperature of each array well. FLIM images could provide a quick method to evaluate optimal temperatures due to the dramatic change in lifetime over a small temperature change. This dramatic change is analogous to logic gate responses of on/off, which could be used to indicate if temperature in each well is optimum by providing a yes/no response.[120] Rapid temperature evaluations could be performed in high-throughput microarrays using this approach. High-throughput temperature evaluations is advantageous as there can be significant variability between temperature devices.[84] Temperature fluctuations of as little as ± 1 ^{o}C in each well may could produce non-uniform products.[84]

There is the potential to produce analogous probes with different fluorescence properties by copolymerising with different fluorophores, for example, coumarin or acridine. These molecules exhibit an increase in fluorescence intensity in polar environments and a decrease in non-polar environments and would thus show a decrease in intensity or fluorescence lifetime with increasing temperature.[118]

6.3.4 Use of Kiton Red as a FLIM temperature probe

6.3.4.1 Problems with using RhB as a temperature probe

Problems have been reported using aqueous RhB when imaging temperature within microfluidic heating devices.[94] The dye adsorbs onto the surfaces of microchannels and this can be exacerbated depending on the material of the devices. The surface adsorption of the dye can be a serious problem when using intensity imaging and also affects fluorescence lifetime imaging due to the different local environments surrounding the fluorophore. Adsorption onto surfaces can affect the temperature response of the fluorophore, therefore the calibration determined in the bulk solution cannot be used to probe the temperature at effected surface as this will not be reveal the true temperature. Ross *et al.* observed systematic errors in temperature measurements when using RhB due to the problems with surface adsorption.[94] They ignored the problem of dye adsorption at surfaces which was observed with concentrated RhB solutions, as it was suggest that the error incurred was insignificant compared to the noise of the CCD detector. Otherwise, reducing the concentration of RhB alleviated the problem although would result in longer acquisition times.[94]

RhB is more soluble in alcohols than water, hence the use of methanol as a solvent in previous lifetime measurements of temperature by Benninger *et al.*[104] However, the low boiling point of methanol (*ca* 65 ^{o}C), can limit its useful temperature range, as problems with boiling and reflux can occur above this temperature.

Figure 6.9 displays some FLIM images to illustrate the problems of using aqueous RhB for imaging temperature within microfluidic devices. Regions of RhB adsorbed onto surfaces can easily be identified from the FLIM image, displayed by the red coloured regions of significantly higher lifetimes than surrounding RhB solution.

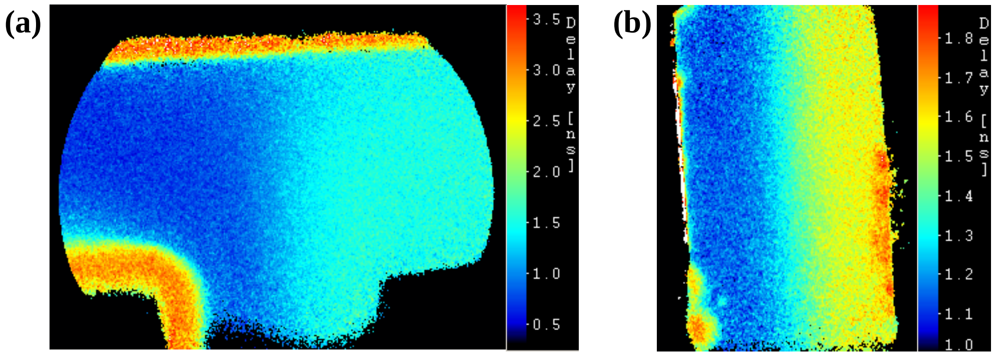

Figure 6.9: FLIM images showing the problems with using aqueous RhB solutions (10^{-3} M) in microfluidic devices. The red coloured regions exhibiting higher lifetime values are the areas where RhB has adsorbed on to the surfaces.

Kiton Red is closely related to RhB, but is significantly more water soluble than RhB, due to its sulphonate substituents (Figure 6.10). The solubility of RhB in methanol is 15 g/L compared with 8 g/L in water,[125] whereas the solubility of Kiton Red in water is ~90 g/L.[126] Kiton Red displays a similar temperature-dependent fluorescence lifetime to RhB, but is advantageous to use with microfluidic heating devices because of its increased solubility in water.

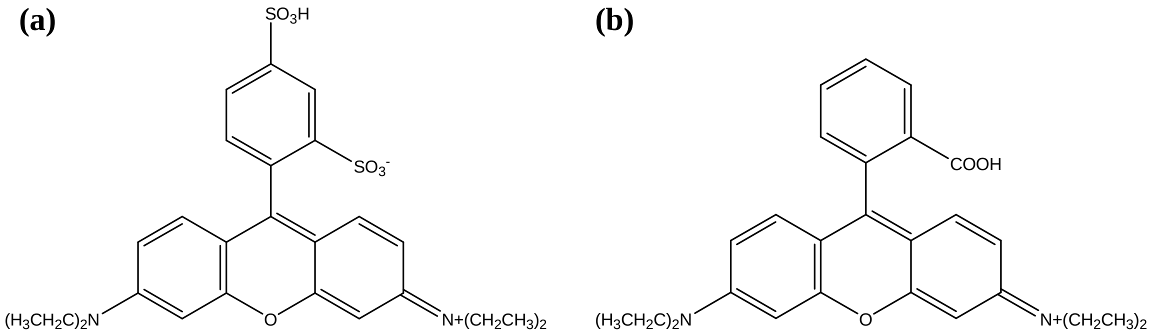

Figure 6.10: Chemical structures of Kiton Red **(a)**, and RhB **(b)**.

6.3.4.2 Explanation of Kiton Red temperature sensitivity

The temperature-dependent lifetime of Kiton Red is due to the free rotation of diethylamino group in the xanthene chromophore. This free rotation is the main non-radiative deactivation pathway of the excited state, and is thought to increase the internal conversion from the first excited state to the ground state.[113] When the diethylamino groups are immobilised, as in rhodamine 101, the molecule exhibits no temperature dependence and the fluorescence quantum yield is near unity.[52]

The photophysical data on rhodamine B derivatives has been interpreted by Casey *et al.* as an internal conversion from a non-emissive twisted state which is in equilibrium with a fluorescent planar state.[113] Data have shown the non-radiative rate constant to be sensitive to the solvent, but the radiative rate is not sensitive.[113] The non-radiative rate constant decreases with an increase in the solvent viscosity, illustrating dynamic solvent effects, which are important in excited-state relaxation processes involving photo-induced conformational changes. The temperature dependence of the fluorescence lifetime is attributed to the non-radiative rate constant, which can be divided into temperature-independent and dependent elements. However, Arrhenius plots of the non-radiative rate constants in various solvents shows no temperature-independent contributions, hence the non-radiative rate constant is independent of viscosity. The temperature dependence of the equilibrium constant for the inter-conversion between the twisted and planar configuration of the molecule $K_{pt,}$, is accountable for the Arrhenius behaviour of the non-radiative rate constant. The solvent polarity has a direct affect on the K_{pt} and hence explains the polarity dependence of the non-radiative rate constant.

6.3.4.3 Calibration of Kiton Red with temperature by TCSPC

The fluorescent lifetime of aqueous solutions of Kiton Red was measured by TCSPC over a range of temperatures from 25 ^{o}C to 90 ^{o}C. Kiton Red displayed a single exponential decay over this range with the lifetime changing from 1.86 ns at 25 ^{o}C to 0.32 ns at 91 ^{o}C (Table 6.4). As the FLIM images are produced by fitting to a single exponential lifetime, Kiton Red which displays a single lifetime over a wide temperature range, is well suited to use as a FLIM temperature probe.

Temperature /^{o}C	τ /ns	χ^2
24.9	1.86	1.13
29.6	1.62	1.06
34.2	1.41	1.06
38.9	1.23	1.09
43.3	1.08	1.09
48.1	0.95	1.09
52.9	0.84	1.15
57.2	0.73	1.10
62.1	0.65	1.11
66.8	0.57	1.15
71.7	0.50	1.13
76.7	0.45	1.19
81.6	0.40	1.04
86.4	0.36	1.08
90.9	0.32	1.10

Table 6.4: Fluorescence lifetimes of Kiton Red as a function of temperature. The χ^2 values indicating the goodness of fit of a single exponential decay function is also shown.

The trend in lifetime change with temperature is represented graphically in Figure 6.11. There is an exponential relationship between lifetime and temperature.

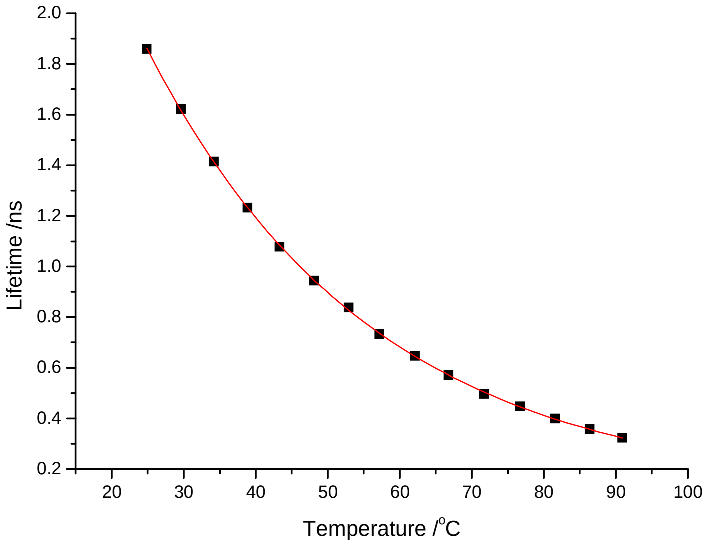

Figure 6.11: The dependence of Kiton Red fluorescent lifetime upon temperature. The data fits well to a single exponential using equation y = 3.86212exp(-x/31.75687) + 0.09765

The temperature dependence of the fluorescence lifetime of Kiton Red obeys the Arrhenius equation, given by

$$\frac{1}{\tau_f} = A\exp\left(\frac{-E_a}{RT}\right) \qquad \text{Equation 6.2}$$

where A is a pre-exponential factor, E_a is the activation energy and R is the molar gas constant. Figure 6.12 shows the linear fit of the temperature dependence of the fluorescence lifetime of Kiton Red using the Arrhenius equation.

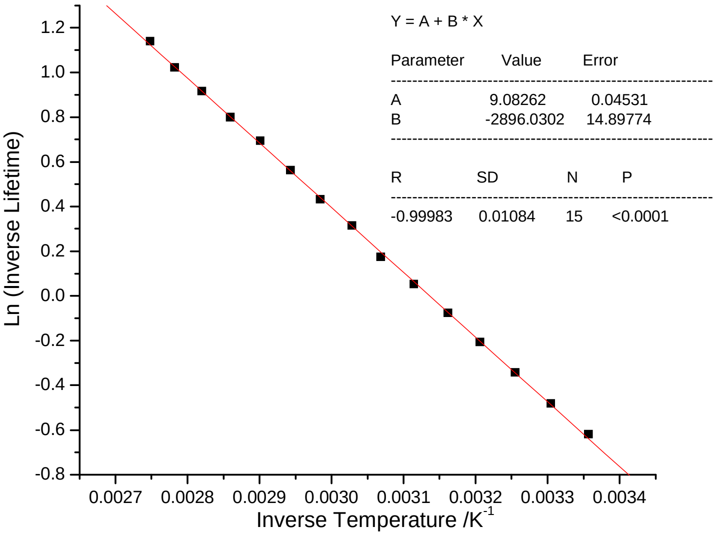

```
Y = A + B * X

Parameter       Value        Error
------------------------------------------------------------
A               9.08262       0.04531
B               -2896.0302    14.89774
------------------------------------------------------------

R           SD          N       P
------------------------------------------------------------
-0.99983    0.01084     15      <0.0001
```

Figure 6.12: Arrhenius plot of the natural logarithm of the inverse lifetime against the inverse temperature. The line is the best fit by the Arrhenius equation with E_a = 24.08 kJmol^{-1}.

A calibration curve to convert fluorescence lifetime to temperature was produced by re-plotting the temperature and lifetime data with the axes switched (Figure 6.13). The temperature-lifetime calibration data fitted well to a bi-exponential function, which was used to convert FLIM images into temperature maps.

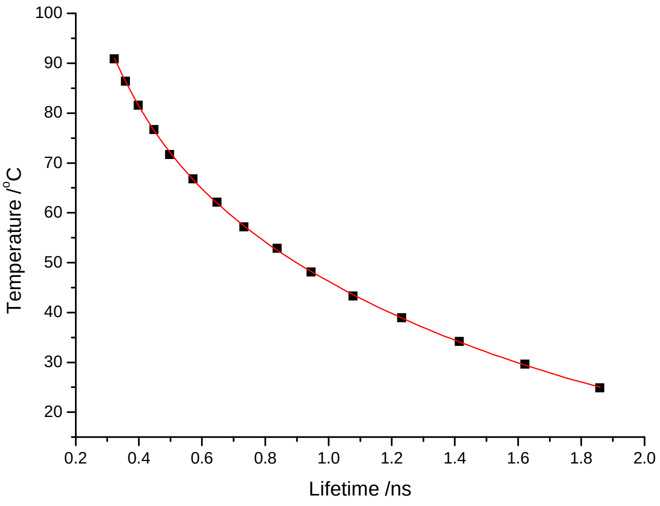

Figure 6.13: Calibration curve showing the relationship between temperature and the fluorescent lifetime of Kiton Red. The calibration graph fits well to a bi-exponential using equation y = 96.57595exp(-x/1.10941) + 126.55986exp(x/0.13408) + 7.01272

The TCSPC data displayed in Table 6.5 was recorded over a 20 ns time range. Increasing the temporal resolution for the shortest lifetimes by acquiring data over a 5 ns time range did not significantly change the fitted lifetimes. Figure 6.15 compares the lifetimes calculated from acquiring data over 20 ns and 5 ns time ranges.

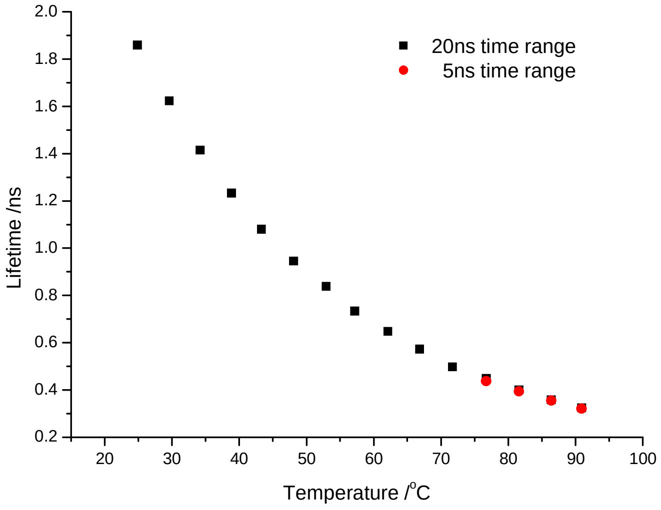

Figure 6.14: Lifetimes from TCSPC data record over 20 ns (black) and 5 ns (red) time ranges for Kiton Red at various temperatures. The four 5 ns data points are obscuring the corresponding 20 ns data points.

6.3.4.4 Fluorescence lifetime imaging of Kiton Red (FLIM)

Two fluid streams of aqueous Kiton Red were pumped into the two inlets of a T-shaped micromixer, to meet head-on and then flow through a mixing channel, as illustrated in Figure 6.15. The left inlet flow was heated, while the right inlet flow was at room temperature.

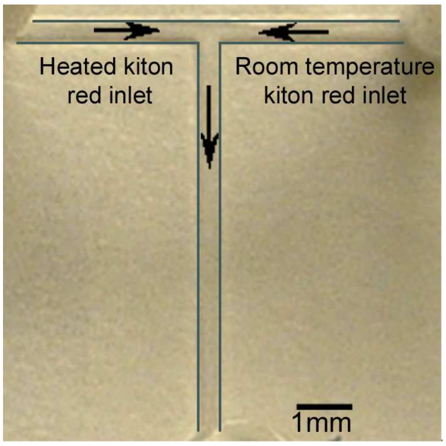

Figure 6.15: Annotated photograph of the T-shaped flow cell. The arrows indicate the inlet flows of heated Kiton Red solution and Kiton Red at room temperature, and the outlet flow.

The mixing of the inlet fluid streams was imaged using the FLIM system at various positions down the mixing channel as indicated in Figure 6.16. A series of temperature profiles across the mixing channel (as detailed in Figure 6.16) was extracted from the FLIM images and converted to temperature using the calibration from Figure 6.13. Figure 6.7a depicts the steep temperature gradient when the fluids streams meet, with the temperature changing from ~58 to ~32 ^{o}C across the channel. As the fluids progress through the mixing channel, the temperature difference across the channel decreases, as shown in the series of temperature profiles (Figure 6.16a-d) at various positions through the mixing channel. The fluids attain a constant temperature of 44 ^{o}C across the channel after progressing 0.9 mm through the mixing channel (Figure 6.16d). An extensive range of temperature profiles along the mixing channels is presented in Figure 6.17.

The inlet flow rate of 75 µm/min was maintained for comparison with the mixing data obtained using the ANS fluorescent probe (as reported in Chapter 4). This was to allow future modelling of the results to distinguish between heat transfer processes and mixing as many reactions need effective mixing and accurate temperature control to achieve high yields. The Péclet number for the room temperature and heated inlet streams are 1500 and 890, respectively. The large difference is attributed to the different fluid temperatures, which has a significant effect on the diffusion coefficient and also the fluid viscosity. The Péclet number for the heated fluid inlet is approximately half that of the cooler inlet, this reduction implies that there is increased lateral diffusion, and hence enhanced mixing, within the channel even though the fluid velocities in each channel are constant. The Reynolds number for the room temperature and heated inlet fluid streams are 5.4 and 8.8, respectively. This difference is mainly due to the effect of temperature on the fluid viscosity, whereas, temperature has a less marked effect on the fluid densities.

As the Kiton Red solutions were constantly flowed through the mixer, no problems with photobleaching occurred and the CCD exposure time was constant for acquiring all the FLIM images (Table 6.1).

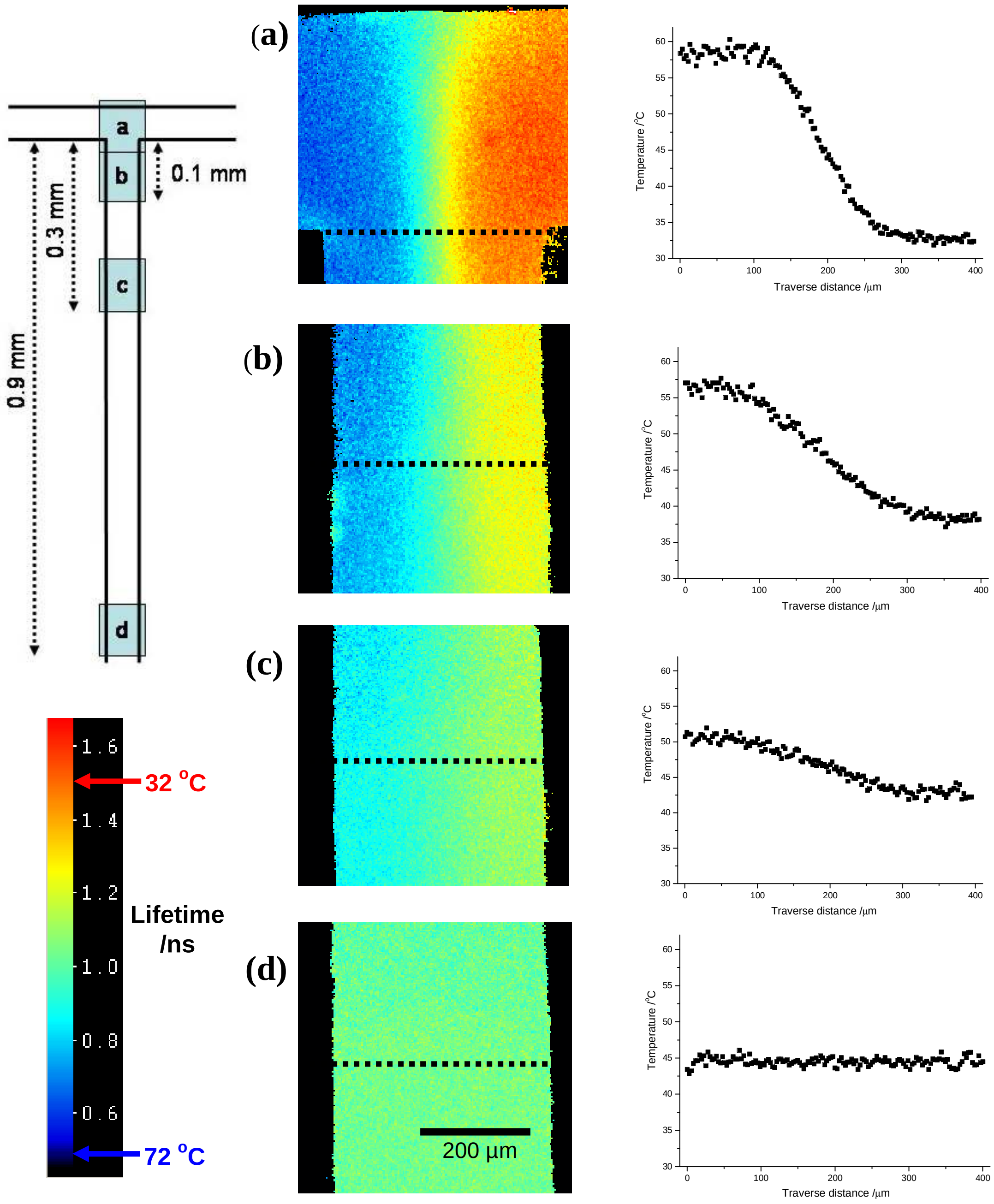

Figure 6.16: FLIM images recorded at positions **(a)** when the inlet flows meet, **(b)** 0.1 mm, **(c)** 0.3 mm, **(d)** 0.9 mm down the mixing channel as shown in the diagram of the T-shaped mixer. The corresponding temperature profiles along the dashed cross-sections indicated in the FLIM images are displayed.

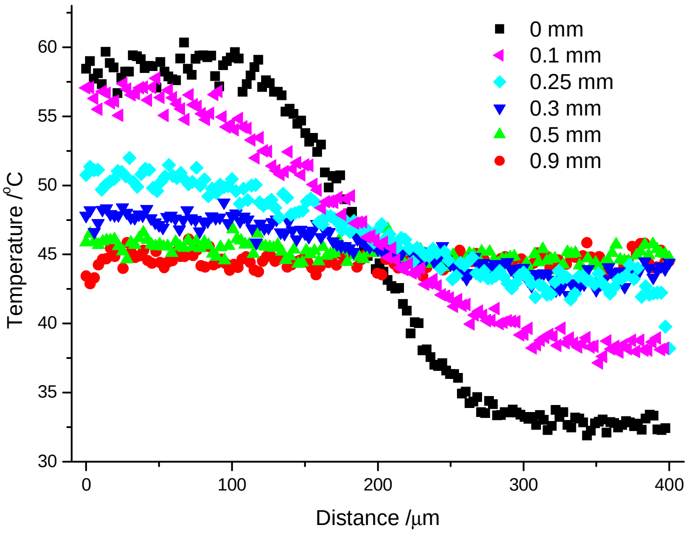

Figure 6.17: Temperature profiles across the mixing channel at various positions along the mixing channel as indicated in the key.

Comparison between intensity and lifetime data

Figure 6.18 shows a comparison between cross-sections of fluorescence intensity and lifetime images at the same distance along the mixing channel. This demonstrates the superiority of the time-resolved technique. The intensity profile displays large irregular variations across the channel with a clear drop-off in intensity at the channel walls, whereas, the FLIM measurement provides a well-defined profile of the lifetime change and is unaffected by the intensity drop at the channel walls. It is evident that intensity-based techniques are particularly unsuitable to measure temperatures close to surfaces due to problems such as light scattering, whereas, lifetime-based techniques are totally unaffected by such problems. The lifetime profile can easily be converted quantitatively to give the temperature profile across the channel using the calibration curve (Figure 6.13).

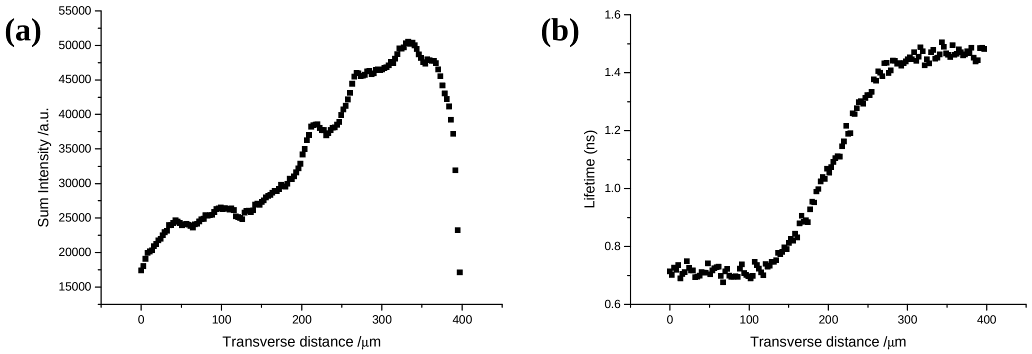

Figure 6.18: Comparison of fluorescence intensity **(a)** and lifetime **(b)** profiles across the mixing channels when the fluid streams meet head-on along the mixing channel. The intensity values were the sum of the time-gated intensity images to allow a direct comparison between the time-resolved and intensity based methods.

6.3.4.5 Conclusion

Kiton Red is an effective fluorescent molecular thermometer in aqueous microfluidic systems over a wide temperature range without the problems reported for RhB. The broad temperature range over which Kiton Red displays a lifetime change is particularly useful as it covers many biological and chemical applications, including PCR, that can be perform in lab-on-a-chip devices. It is beneficial to use aqueous solutions of temperature-sensitive fluorophores as the temperature range over which it can be used covers the range required by many biological and chemical processes. This overcomes reflux problems resulting from using solvents to solubilise fluorophores to probe temperature above the solvent boiling point.

Aqueous solutions of Kiton Red can be used to probe heat transfer effects at surfaces due to the lack of adsorption and the associated problems with temperature calibration discussed above.

The use of Kiton Red as an aqueous temperature probe does not limit the choice of material for the manufacture of microfluidic devices in which temperature mapping would be desirable, as has been observed with RhB. Kiton Red can be used at increased concentrations in aqueous solutions due to its higher solubility, which results in decreased acquisition times for temperature mapping compared to RhB.

6.3.5 Temperature calibration of a micro-PCR chamber

In many microfluidic applications high spatial resolution of temperature is crucial for reactions that exhibit extreme temperature sensitivity. Even slight temperature fluctuations within a device/region can potentially affect the selectivity and yield of product. An obvious example where precise temperature control is fundamental is illustrated by lab-on-a-chip PCR reactions, the production of which has rapidly increased over recent years. One of the major advantages to performing PCR in devices with significantly reduced dimensions has been the ability to promptly change the temperature within the device i.e. for rapidly heating and cooling for PCR temperature cycling. Efficient PCR reactions reply on achieving temperatures within very narrow temperature ranges and temperature fluctuations as small as ±1 ^{o}C within devices can detrimentally affect the quality of the yield by amplifying undesirable products.[84]

Kiton Red and poly(DBD-AE-*co*-NIPAM) solutions have been use to measure the temperature within a prototype micro-PCR chamber, where the temperature is controlled by a thermocouple attached to the heating device (both chamber and heating device were provided by Lab901 Ltd). The equipment allows the heating and temperature control of eight parallel PCR reactions in separate chambers. The temperature within each chamber should be identical to ensure consistent PCR product and yield from each chamber. Figure 6.19 shows diagrams of the PCR system. Table 6.5 displays the results from measuring the actual temperature inside the PCR chambers using Kiton Red, compared with the temperature indicated by the external thermocouple attached to the heating element. The temperature within the eight chambers show deviations of 1-2 ^{o}C, 2-5 ^{o}C and 2-7 ^{o}C for set temperatures of 55 ^{o}C, 72 ^{o}C and 95 ^{o}C, respectively. It is evident that the external temperature measured by the thermocouple provides an inaccurate indication of temperature within the chambers.

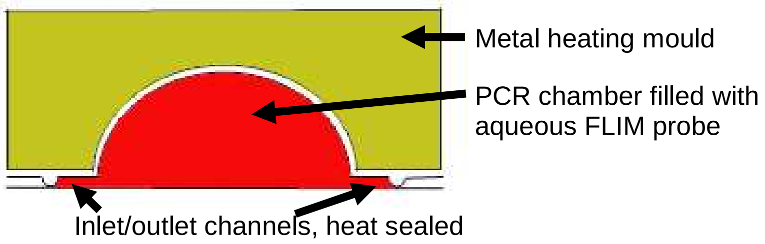

(a)

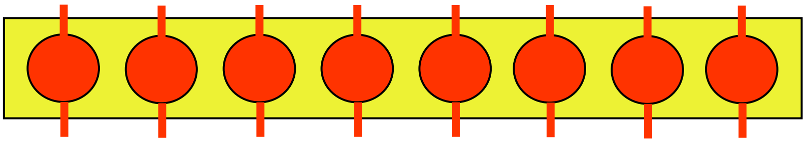

(b)

Figure 6.19: Diagrams of the PCR device; **(a)** side view of a single hemisphere chamber heated by a metal mould surrounding the chamber, **(b)** bottom view of eight PCR chambers held within the heating device.

Chamber	Set T = 55 ^oC	Set T = 72 ^oC	Set T = 95 ^oC
1	53	67	87
2	54	67	88
3	54	68	88
4	54	69	88
5	54	69	88
6	54	69	89
7	54	69	87
8	55	70	93

Table 6.5: Temperatures measured within the eight PCR chambers by recording the FLIM image of Kiton Red solution inside each chamber, for externally set temperatures of 55, 72 and 95 ^oC.

An advantage of using FLIM to image and map the temperature within heating devices is the ability to detect air bubbles and probe the temperature effects resulting from their formation and expansion. This is especially advantageous for PCR chambers as excessive air bubble formation can inhibit PCR reactions.[101] Figure 6.20 displays a FLIM image of a PCR chamber with two air bubble formed at the chamber edge.

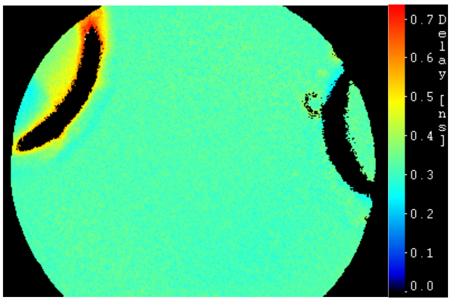

Figure 6.20: FLIM image of a PCR chamber showing two air bubbles formed at the chamber edge.

The temperature uniformity within the PCR chamber can be investigated using poly(DBD-AE-*co*-NIPAM), with high temperature resolution. Figure 6.21 shows the FLIM images recorded at the chamber edge. The images clearly show the absence of temperature distortions or fluctuations and demonstrate temperature uniformity across the chamber. Temperature fluctuations, as small as 0.1 ^{o}C would be detected using this FLIM probe. Regions of interest within the FLIM image were selected and fitted to three lifetimes to calculate the precise temperature. The actual temperatures within the chamber were thus determined to be 30.8, 32.0 and 33.6 ^{o}C for the thermocouple temperatures of 30, 32 and 34 ^{o}C, respectively.

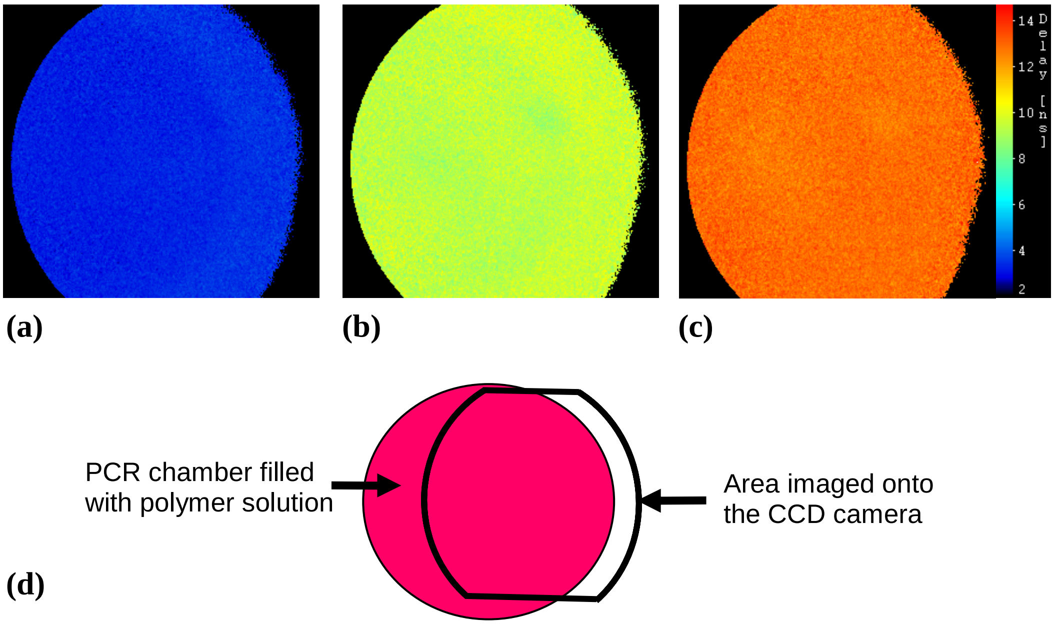

Figure 6.21: FLIM images of the micro-PCR chamber with poly(DBD-AE-*co*-NIPAM) solution. The heating element thermocouple was preset for temperatures of 30, 32 and 34 ^{o}C for images **a, b** and **c**, respectively. **(d)** Diagram showing the area of the chamber imaged onto the CCD camera. Images were recorded using a 10x objective.

6.3.5.1 Conclusion

The FLIM technique using aqueous solutions of Kiton Red is effective to probe and map temperature over a wide temperature range within microfluidic devices. The technique has been demonstrated to be valuable to verify the true temperature within prototype commercial microfluidic devices and to correct for offsets or lags from external temperature sensors when the device is in a real working mode. As discussed in the introduction, poor thermal contact between sensors, heating devices and the fluids within microfluidic devices can create large temperature differences between the actual temperature of the fluid and the perceived temperature of the fluid. The applicability of this technique for use in real commercial devices rather than lab-based prototype devices which have been fully optimised for optical interrogation has been demonstrated.

The use of aqueous poly(DBD-AE-*co*-NIPAM) solution, which is ultra sensitive to slight temperature variations, can provide valuable information on the temperature uniformity within a device right up to the walls. This is particularly relevant to biological systems such as cell cultures, where it has been shown that even slight temperature variations can be detrimental.[110]

6.4 Overall Temperature Conclusions

Microfluidic reactors continue to be increasingly used to perform a variety of biological and chemical reactions at the microscale due to the advantages offered as a consequence of the high-surface-to-volume ratio. To enable the continued uptake of this technology into new applications and the commercialisation of products, techniques readily available to enable the thermal management/efficiency of such devices is essential. Precise temperature control and measurement within microfluidic devices is fundamental to the performance of these devices to insure consistent and repeatable output yields. Given that temperature is considered such an important parameter in this field it has been extremely problematic to accurately measure temperature in the ultra small volumes of fluids used in these devices. There have been significant developments in the fabrication of microfluidic devices but little development on the thermal management and the accurate validation thereof.

The common methods of temperature measurement within microfluidic device using micro-thermocouples and sensors only provide a single point measurement and no spatial resolution of temperature within a device. Non-invasive spatial mapping of temperature within such small volumes of liquids is advantageous to ensure temperature uniformity and distribution within devices.

The FLIM technique reported in this chapter provides an effective, non-invasive method to extract accurate temperature information with high spatial resolution. FLIM is a superior imaging technique to spatially map the temperature within microfluidic devices because the technique overcomes the problems encountered in commonly used intensity imaging methods. The technique is highly repeatable due to the elimination of the dependency on the excitation intensity, collection efficiency, optical path, light scattering problems and concentration effects.

Temperature fluctuations as small as ± 1 ^{o}C with microfluidic devices can have a detrimental effect on yields. It is for these reasons that new highly temperature sensitive FLIM probes are sought. It has been demonstrated that the average fluorescence lifetime of aqueous poly(DBD-AE-*co*-NIPAM) is extremely sensitive to temperature within the range of ~31 ^{o}C to ~33 ^{o}C. FLIM images of aqueous poly(DBD-AE-*co*-NIPAM) can be used to spatially map temperature changes within microfluidic devices with a resolution of less than 0.1 degree. *N*-alkylacrylamide polymer labelled with benzofurans can be tuned to respond in a particular temperature range desired by adapting their chemical properties. These polymers can be used very effectively in combination with Kiton Red to achieve temperature measurements with both wide dynamic range and high resolution within aqueous microfluidic systems.

Kiton Red is an effective temperature sensitive FLIM probe for mapping temperature within aqueous microfluidic systems over a broad temperature range and has been used to measure the fluid temperature within a prototype micro-PCR system for commercial development. FLIM of Kiton Red provides an ideal technique to validate prototype devices and to optimise the thermal design of microfluidic devices to ensure desirable temperature conditions are achieved and maintained.

Quantitative measurement techniques, such as the FLIM technique reported in this chapter, are essential to validate mathematical modelling of heat transfer and mixing within microfluidic devices, both of which are extremely important parameters for reaction efficiency, yields and reduction of unwanted side products.

The results of the mixing of Kiton Red streams at different temperatures presented within this chapter have been used by the National Physical Laboratory to evaluate commercial CFD codes. This manuscript, submitted to the journal *Microfluidics and Nanofluidics,* can be viewed in the Appendix. The paper illustrates the excellent agreement between the modelling and experimental results.

Chapter 7

Conclusions

The aim of the work described in this thesis was to exploit the benefits offered by Fluorescence Lifetime Imaging Microscopy (FLIM) in application to spatially mapping fluid composition and temperature within microfluidic systems.

It has been demonstrated that FLIM is a significantly superior technique due to its inherent insensitivity to problems which have hampered other imaging methods commonly applied to microfluidic systems, such as those based on fluorescence intensity and colourimetric approaches.

Prior to the publication of work presented in this thesis, FLIM was limited to the imaging of biological systems. However, the uptake of FLIM techniques to probe important fluid interaction and parameters, such as mixing and temperature, within microfluidic systems has steadily increased. FLIM approaches are now actively employed by several research groups to explore microfluidics.

It has been established, that widefield FLIM can directly assess the two-dimensional mixing of fluids within microfluidic channels and provide a high level of quantification. The solvent-sensitive fluorescence lifetime of 1,8-anilinonaphthalene sulfonate (ANS) was exploited to map the diffusional mixing between fluid streams of pure methanol and a water-methanol mixture. The system faithfully reported the fluid composition, as the lifetime is governed solely by the solvent environment of the ANS probe, and was proved to be immune to other undesirable optical effects. The FLIM technique is not limited to the use of this solvent system or fluorophore, but this study exemplifies the level of quantification offered and highlights FLIM as a measurement tool of choice in exploring microscale environments. An additional advantage of this methodology is the ability to monitor the mass transport of fluids, rather than the diffusion of tracer probes as is commonly used in fluorescence intensity and colourimetric imaging techniques. Because of the importance of achieving rapid mixing in microfluidic devices, the number of microfluidic mixers designed and fabricated has swiftly increased. Hence there is an urgent need for characterisation tools to evaluate these mixing devices. Therefore it is expected that FLIM will become an essential tool for quantitatively mapping the fluid composition and mixing within microfluidic systems.

The FLIM technique, using solutions of ANS, has been successfully employed to evaluate a range of commercial microfluidic mixers. Various micromixer design parameters were investigated using the FLIM technique, including the confluence angle, channel dimensions, chambers, serpentine channel design, the effect of asymmetric curves in the vertical channel walls and obstacles fabricated in the mixing channel.

The relationship between the temperature and fluorescence lifetime of an aqueous solution of an *N*-alkylacrylamide polymer labelled with a benzofuran fluorophore, [poly(DBD-AE-*co*-NIPAM], has been investigated for the first time using Time Correlated Single Photon Counting (TCSPC) techniques. The polymer displayed a dramatic change in its average fluorescence lifetime of over 10 ns, over a temperature range of a few degrees. This polymer system was used with FLIM to quantitatively map temperatures within microfluidic environments with sub-degree resolution. Analogous polymers with adapted chemical properties can extend the range of temperature sensitivities to suit the intended application. Therefore, this type of fluorescent polymer can potentially be employed as a new sensitive molecular thermometer to map temperatures with high spatial resolution within a range of fluidic systems where precise temperature measurements are essential. The sensitivity of aqueous poly(DBD-AE-*co*-NIPAM) was exploited to rigorously test the performance of a prototype microfluidic heating device.

The fluorescence lifetime sensitivity of a water-soluble rhodamine B derivative, Kiton Red, was used with FLIM to quantitatively map temperatures over an extensive dynamic range of 25 ^{o}C to over 90 ^{o}C, thereby covering the temperature range necessary for numerous biological and chemical interactions. Aqueous solutions of Kiton Red were employed to map the temperature distributions resulting from the mixing of fluid streams of different temperatures within a microfluidic system. Thus, mixing and temperature, control of both of which is crucial to ensure high yields in biological and chemical processes within microfluidic devices, are quantifiable with high spatial resolution using FLIM. In addition, the fluid temperature within a prototype microfluidic PCR device, used to amplify DNA, was quantified to calibrate the device. Kiton Red overcomes problems encountered by other researchers using the related fluorophore, rhodamine B, such as poor aqueous solubility and surface adsorption, which compromised the ability to map temperature in microfluidic devices.

Techniques capable of mapping mixing and temperature within microfluidic devices with high quantification and spatial resolution are essential to validate mathematical modelling of heat transfer and mixing within microfluidic devices and to evaluate prototype designs of microfluidic systems. The ability of FLIM to satisfy this need is demonstrated by the very effective use of experimental data presented in this thesis, in combination with computational fluidic dynamic modelling, to analyse solute and thermal transport in a microfluidic system with unprecedented quantitative detail, as described in the Appendix.

References

1. Vilkner, T.; Janasek, D.; Manz, A. *Anal.Chem.* **2004,** *76*, 3373.-3386.

2. Hibara, A.; Nonaka, M.; Tokeshi, M.; Kitamori, T. *J.Am.Chem.Soc.* **2003,** *125*, 14954-55.

3. Xu, S.; Nie, Z.; Seo, M.; Lewis, P.; Kumacheva, E.; Stone, H. A.; Garstecki, P.; Weibel, D. B.; Gitlin, I.; Whitesides, G. M. *Angew.Chem.Int.Ed.* **2005,** *44*, 724-28.

4. Song, H.; Tice, J. D.; Ismagilov, R. F. *Angew.Chem.Int.Ed.* **2003,** *42*, 768-72.

5. Fletcher, P. D. I.; Haswell, S. J.; Pombo-Villar, E.; Warrington B.H.; Watts, P.; Wong, S. Y. F.; Zhang, X. *Tetrahedron* **2002,** *58*, 4735-57.

6. Kopp, M. U.; de Mello, A. J.; Manz, A *Science* **1998,** *280*, 1046-48.

7. Reyes, D. R.; Iossifidis, D.; Auroux, P.-A.; Manz, A. *Anal.Chem.* **2002,** *74*, 2623-36.

8. Nguyen, N-T.; Wu, Z. *J.Micromech.Microeng.* **2005,** *15*, R1-R16.

9. Ottino, J. M.; Wiggins, S. *Science* **2004,** *305*, 485-86.

10. Zhao, B.; Moore, J. S.; Beebe, D. J. *Science* **2001,** *291*, 1023-26.

11. Kitamura, N.; Hosoda, Y.; Iwasaki, C.; Ueno, K.; Kim, H-B. *Langmuir* **2003,** *19*, 8484-89.

12. Allen, R. W. K. *Ingenia, The Royal Academy of Engineering* **2001,** *April*.

13. Schönfeld, F; Hessel, V.; Hofmann, C *Lab on a Chip* **2004,** *4*, 65-69.

14. Lakowicz, J. R. *Principles of Fluorescence Spectroscopy,* 2nd ed.; Kluwer Academic/ Plenum Publishers: 1999.

15. Skoog, D. A.; Leary, J. J. *Principles of Instrumental Analysis,* 4th ed.; Saunders College Pub: 1992.

16. O'Connor, D. V.; Phillips, D. *Time-correlated Single Photon Counting,* Academic Press: 1984.

17. Valeur, B. *Molecular Fluorescence: Principles and Applications*, Wiley-VCH: 2001.

18. Clegg, R. M.; Holub, O.; Gohlke, C. *Methods Enzymol.* **2003,** *360*, 509-42.

19. Sud, D.; Mehta, G.; Mehta, K.; Linderman, J.; Takayama, S.; Mycek, M-A. *Journal of Biomedical Optics* **2006,** *11*, 050504-1-050504-3.

20. Tabeling, P. *Introduction to Microfluidics*, Oxford University Press: 2005.

21. Glen, N., *'State of the art review of microfluidics'*, 2006, report produced by TUV NEL, East Kilbride, Glasgow, G75 0QU, UK. Report produced for the Measurement for Emerging Technologies Programme, National Measurement System Programme, Department of Trade and Industry, UK.

22. Squires, T. M.; Quake, S. R. *Reviews of Modern Physics* **2005,** *77*, 977-1026.

23. Stroock, A. D.; Dertinger, S. K. W.; Ajdari, A.; Meziæ, I.; Stone, H. A.; Whitesides, G. M. *Science* **2002,** *295*, 647-51.

24. Redford, G, I; Majumdar, Z K; Sutin, J D B; Clegg, R M *The Journal of Chemical Physics* **2005,** *123*, 224504-1-224504-6.

25. Einstein, A., *'Investigations on the theory of the Brownian movement'*, 1956. Dover Publications.

26. Tretheway, D.; Meinhart, C. *Physics of Fluids* **2002,** *14*, L9-L12.

27. Yamaguchi, Y.; Takagi, F.; Wateri, T.; Yamashita, K.; Nakamura, H.; Shimizu, H.; Maeda, H. *Chemical Engineering Journal* **2004,** *101*, 367-72.

28. Kamholz, A. E.; Yagar, P. *Biophysical Journal* **2001,** *80*, 155-60.

29. Sharp, K. V.; Adrian, R. J.; Santiago, J. G.; Molho, J. I. *The MEMS Handbook*, 1st Ed, 2002, edited by Gal-el-Hak, M., CRC Press, Chapter 6.

30. '*Fundamentals of Intensified Charge Coupled Device (ICCD)'*, 2006, equipment operating instructions by manufacturers LaVision GmbH, Anna-Vandenhoeck-Ring 19, D-37081 Goettingen, Germany.

31. Millington, M.; Grindlay, G. I.; Altenbach, K.; Neely, R. K.; Kolch, W.; Bencina, M.; Read, N. D.; Jones, A. C.; Dryden, D. T. F.; Magennis, S. W. *Biophysical Chemistry* **2007,** *127*, 155-64.

32. Millington, M. J., *'Fluorescence lifetime imaging and spectroscopy of GFT mutants, and the characterisation of FRET pairs, using high sensitivity, time- and space- correlated single photon counting* detector', PhD Thesis, The University of Edinburgh, 2006.

33. Mengeaud, V; Josserand, J; Girault, H. H. *Anal Chem.* **2002,** *74*, 4279-86.

34. Weigl, B H; Yager, P *Science* **1999,** *283*, 346-47.

35. Chen, H.; Meiners, J.-C. *Appl.Phys.Lett* **2004,** *84*, 2193-95.

36. Munson, M. S.; Yager, P. *Anal.Chim.Acta* **2004,** *507*, 63-71.

37. Locascio, L. E. *Anal.Bioanal.Chem.* **2004,** *379*, 325-27.

38. Sritharan, K; Strobi, C J; Schneider, M F; Wixforth, A; Guttenberg, Z *Applied Physics Letters* **2006,** *88*, 054102-1-054102-3.

39. Masca, S. I.; Rodriguez-Mendieta, I. R.; Friel, C. T.; Radford, S. E.; Smith, D. A. *Review of Scientific Instruments* **2006,** *77*, 055105-1-055105-9.

40. Green, J.; Holdo, A. E.; Khan, A *International Journal of Multiphysics* **2007,** *1*, 1-32.

41. Hessel, V.; Lowe, H.; Schonfeld, F *Chemical Engineering Science* **2005,** *60*, 2479-501.

42. Johnson, T. J.; Ross, D.; Locascio, L. E. *Anal.Chem.* **2002,** *74*, 45-51.

43. Sasaki, N; Kitamori, T; Kim, H-B *Lab on a Chip* **2006,** *6*, 550-54.

44. Weigl, B. H.; Yager, P. *Science* **1999,** *283*, 346-47.

45. Chen, J. M.; Horng, T-L.; Tan, W. Y. *Microfluid.Nanofluid.* **2006,** *2*, 455-69.

46. Seong, G. H.; Crooks, R. M. *J.Am.Chem.Soc.* **2002,** *124*, 13360-61.

47. Gunther, A.; Jhunjhunwala, M.; Thalmann, M.; Schmidt, M. A.; Jensen, K. F. *Langmuir* **2005,** *21*, 1547-55.

48. Vallejos, J. R.; Kostov, Y.; Marten, M. R.; Rao, G. *Biotechnology Progress* **2005,** *21*, 1531-36.

49. Bothe, D.; Stemich, C.; Warnecke, H-J., *Chemical Engineering Science* **2006,** *61*, 2950-58.

50. Matsumoto, R.; Farangis Zadeh, H.; Ehrhard, P. *Experiments in Fluids* **2005,** *39*, 722-29.

51. Burghelea, T; Segre, E; Bar-Joseph, I; Groisman, A; Steinberg, V *Physical Journal Review E* **2004,** *69*, 066305-1-066305-8.

52. Karstens, T.; Kobs, K. *Journal of Physical Chemistry* **1980,** *84*, 1871-72.

53. Bessoth, F. G.; deMello, A. J.; Manz, A. *Analytical Communications* **1999,** *36*, 213-15.

54. Meinhart, C. D.; Wereley; S.T.; Santiago, J. G. *Experiments in Fluids* **1999,** *27*, 414-19.

55. Schonfeld, F.; Hessel, V.; Hofmann, C. *Lab on a Chip* **2004,** *4*, 65-69.

56. Kenis, P. J. A.; Ismagilov, R. F.; Whitesides, G. M. *Science* **1999,** *285*, 83-85.

57. Wong, S. H.; Ward, M. C. L.; Wharton, C. W. *Sensors and Actuators B* **2004,** *100*, 359-79.

58. Kim, D. S.; Lee, S. H.; Kwon, T. H.; Ahn, C. H. *Lab on a Chip* **2005,** *5*, 739-47.

59. Knockmann, N; Kiefer, T; Engler, M; Woias, P *Sensors and Actuators B* **2006,** *117*, 495-508.

60. Aref, H. *Physics of Fluids* **2002,** *14*, 1315-25.

61. Yaralioglu, G; Wygant, I O.; Marentis, T C; Khuri-Yakub, B T *Anal.Chem.* **2004,** *76*, 3694-98.

62. Ehrfeld, W; Golbig, K; Hessel, V; Lowe, H; Richter, T *Ind.Eng.Chem, Res* **1999,** *38*, 1075-82.

63. Aoki, N.; Mae, K *Chemical Engineering Journal* **2006,** *118*, 189-97.

64. Guichardon, P.; Falk, L. *Chemical Engineering Science* **2000,** *55*, 4233-43.

65. Haj, F. G.; Verveer, P. J.; Squire, A.; Neel, B. G.; Bastiaens P.I.H. *Science* **2002,** *295*, 1708-11.

66. Gadella Jr., T. W. J.; Jovin, T. M. *The Journal of Cell Biology* **1995,** *129*, 1543-58.

67. Lakowicz, J. R.; Szmacinski, H; Nowaczyk, K.; Johnson, M. L. *Natl.Acad.Sci.USA* **1992,** *89*, 1271-75.

68. Benninger, R K P; Hofmann, O; McGinty, J; Requejo-Isidro, J; Munro, I; Neil, M A A; de Mello, A; French, P M W *Optics Express* **2005,** *13*, 6275-85.

69. Elder, A D; Frank, J H; Swartling, J; Dai, X; Kaminski, C F *Journal of Microscopy* **2006,** *224*, 166-80.

70. Elder, A. D.; Matthews, S. M.; Swartling, J; Yunus, K.; Frank, J H; Brennan, C. M.; Fisher, A. C.; Kaminski, C F *Optics Express* **2006,** *14*, 5456-67.

71. Dougan, L.; Crain, J.; Vass, H.; Magennis, S. W. *Journal of Fluorescence* **2004,** *14*, 91-97.

72. Stone, H. A.; Kim, D. *AIChE Journal* **2001,** *47*, 1250-54.

73. Glasgow, I.; Lieber, S.; Aubry, N. *Anal.Chem.* **2004,** *76*, 4825-32.

74. Glasgow, I.; Aubry, N. *Lab Chip* **2003,** *3*, 114-20.

75. Xi, C.; Marks, D. M.; Parikh, D. S.; Raskin, L.; Boppart, S. A. *Proceedings of the National Academy of Science* **2004,** *101*, 7516-21.

76. Wang, H.; Iovenitti, P.; Harvey, E.; Masood, S. *Smart Materials and Structures* **2002,** *11*, 662-67.

77. Noblitt, S. D.; Kraly, J. R.; VanBuren, J. M.; Hering, S. V.; Collett, J. L.; Henry, C. S. *Anal.Chem.* **2007,** *79*, 6249-54.

78. Slavik, J. *Biochimica et Biophysica Acta* **1982,** *694*, 1-25.

79. Shukla, S. K. *Chromatographia* **1975,** *8*, 27-32.

80. Yilmaz, H. *Turkish Journal of Physics* **2002,** *26*, 243-46.

81. Nath, P.; Roy, S.; Conlisk, T.; Fleischman, J. *Biomedical Microdevices* **2005,** *7*, 169-77.

82. Stroock, A. D.; McGraw, G. J. *Phil.Trans.R.Soc.Lond.A* **2004,** *362*, 971-86.

83. Jahnisch, K.; Hessel, V.; Lowe, H.; Baerns, M. *Angew.Chem.Int.Ed.* **2004,** *43*, 406-46.

84. Sadler, D. J.; Changrani, R.; Robert, P.; Chou, C-F.; Zenhausern, F. *IEEE Transactions on Components and Packing Technologies* **2003,** *26*, 309-16.

85. Fujisawa, N; Hashizume, Y. *Meas.Sci.Technol.* **2001,** *12*, 1235-42.

86. Iles, A.; Fortt, R.; de Mello, A. J. *Lab Chip* **2005,** *5*, 540-44.

87. Guijt, R. M.; van Dedem, G. W. K.; de Rooij, N. F.; Verpoorte, E. *Lab Chip* **2003,** *3*, 1-4.

88. El-Ali, J.; Sorger, P. K.; Jensen, K. F. *Nature* **2006,** *442*, 403-11.

89. Roman, G. T.; Chen, Y.; Viberg, P.; Culbertson, A. H.; Culbertson, C. T. *Analytical and Bioanalytical Chemistry* **2007,** *387*, 9-12.

90. Seger-Sauli, U.; Panayiotou, M.; Schnydrig, S.; Jordan, M.; Renaud, P *Electrophoresis* **2005,** *26*, 2239-46.

91. De Mello, A. J.; Habgood, M.; Lancaster, N. L.; Welton, T.; Wootton, R. C. R. *Lab Chip* **2004,** *4*, 417-19.

92. Tang, G. Y.; Yang, C.; Gong, H. Q.; Chai, C. J.; Lam, Y. C. *Journal of Physics: Conference Series International MEMS Conference 2006* **2006,** *34*, 925-30.

93. Dodge, A.; Turcatti, G.; Lawrence, I; de Rooij, N. F.; Verpoorte, E *Anal.Chem.* **2004,** *76*, 1778-87.

94. Ross, D.; Gaitan, M.; Locascio, L. E. *Anal.Chem.* **2001,** *73*, 4117-23.

95. Davis, L. K.; Liu, K-L. K.; Lanan, M.; Morris, M. D. *Anal.Chem.* **1993,** *65*, 293-98.

96. Duhr, S.; Arduini, S.; Braun, D. *Eur.Phys.J.E* **2004,** *15*, 277-86.

97. Ross, D.; Locascio, L. E. *Anal.Chem.* **2002,** *74*, 2556-64.

98. Gui, L.; Ren, C. L. *Anal.Chem.* **2006,** *76*, 6215-22.

99. Rychlik, W.; Spencer, W. J.; Rhoads, R. E *Nucleic Acids Research* **1990,** *18*, 6409-12.

100. Chaudhari, A. M.; Woudenberg, T. M.; Albin, M.; Goodson, K. E. *Journal of Microelectromechanical Systems* **1998,** *7*, 345-55.

101. Yoon, D. S.; Lee, Y-S.; Lee, Y.; CHo, H. J.; SPNG, S. W.; Oh, K. W.; Cha, J.; Lim, G. J *Journal of Micromechanics and Microengineering* **2002,** *12,* 813-23.

102. Noh, J.; Sung, S. W.; Jeon, M. K.; Kim, S. H.; Lee, L. P.; Woo, S. W. *Sensors and Actuators A* **2005,** *122*, 196-202.

103. Kim, S. H.; Noh, J.; Jeon, M. K.; Kim, K. W.; Lee, L. P.; Woo, S. I. *Journal of Micromechanics and Microengineering* **2006,** *16*, 526-30.

104. Benninger, R. K. P.; Koc, Y.; Hofmann, O.; Requejo-Isidro, J.; Neil, M. A. A.; French, P. M. W.; deMello, A. J. *Anal.Chem.* **2006,** *78*, 2272-78.

105. Lacey, M. E.; Webb, A. G.; Sweedler, J. V. *Anal Chem.* **2000,** *72*, 4991-98.

106. Lacey, M. E.; Webb, A. G.; Sweedler, J. V. *Anal.Chem.* **2002,** *74*, 4583-87.

107. Liu, K-L. K.; Davis, L. K.; Morris, M. D. *Anal.Chem.* **1994,** *66*, 3744-50.

108. Easley, C. J.; Legendre, L. A.; Roper, M. G.; Wavering, T. A.; Ferrance, J. P.; Landers, J. P. *Anal.Chem.* **2005,** *77*, 1038-45.

109. Sato, Y; Irisawa, G; Ishizuka, M; Ishizuka, M; Hishida, K; Maeda, M *Meas.Sci.Technol.* **2003,** *14*, 114-21.

110. Filevich, O; Etchenique, R *Anal.Chem.* **2006,** *78*, 7499-503.

111. Mao, H.; Holden, M. A.; You, M.; Cremer, P. S. *Anal.Chem.* **2006,** *74*, 5071-75.

112. Jeon, S.; Turner, J.; Granick, S. *J.Am.Chem.Soc.* **2003,** *125*, 9908-09.

113. Casey, K. G.; Quitevis, E. L. *Journal of Physical Chemistry* **1988,** *92*, 6590-94.

114. Sakakibara, J.; Hishida, K.; Maeda, M. *Experiments in Fluids* **1993,** *16*, 82-96.

115. Kitamura, N.; Hosoda, Y.; Iwasaki, C.; Ueno, K.; Kim, H-B. *Langmuir* **2003,** *19*, 8484-89.

116. Kitamura, N.; Hosoda, Y.; Ueno, K.; Iwata, S. *Analytical Science* **2004,** *20*, 783-86.

117. *CRC Handbook of Chemical and Physics*, 52nd ed.; The Chemical Rubber Co.: 1971.

118. Uchiyama, S.; Matsumara, Y.; de Silva, A. P; Iwai, K. *Anal.Chem.* **2003,** *75*, 5926-35.

119. Uchiyama, S.; Matsumara, Y.; de Silva, A. P; Iwai, K *Anal.Chem.* **2004,** *76*, 1793-98.

120. Uchiyama, S.; Kawai, N.; de Silva, A. P; Iwai, K. *J.Am.Chem.Soc.* **2004,** *126*, 3032-33.

121. Uchiyama, S.; Santa T.; Iwai, K. *J.Chem.Soc., Perkin Trans.2* **1999,** 2525-32.

122. Iwai, K.; Matsumara, Y.; Uchiyama, S.; de Silva, A. P *J.Mater.Chem.* **2005,** *15*, 2796-800.

123. Schild, H. G. *Progress in Polymer Science* **1992,** *17*, 163-249.

124. Lee, K C B; Siegel, J; Webb, S E D; Leveque-Fort, S; Cole, M J; Jones, R; Dowling, K; Lever, M J; French, P M W *Biophysical Journal* **2001,** *81*, 1265-74.

125. Malaisamy, R.; Ulbricht, M. *Separation and Purification Technology* **2004,** *39*, 211-19.

126. Lee, K.; Lawandy, N. M. *Optics Communications* **2002,** *203*, 169-74.

Appendix

Quantitative comparison of thermal and solutal transport in a T-mixer by FLIM and CFD. D-. A. Mendels, E. M. Graham, S. W. Magennis, A. C. Jones, François Mendels. Manuscript accepted for publication in *Microfluidics and Nanofluidics*.

Lectures and Conferences

Postgraduate Lectures and Courses

Physical Chemistry Section Seminars
COSMIC Seminars
GRAD Schools Management Training Course
Fluid Mechanics
Laser Physics

Conferences and Meetings

RSC Conference, *High Throughput Medicinal Chemistry*, 10th May 2005, Institute of Physics, London

Meeting on Optics and Microfluidics, 2nd June 2005, The University of Edinburgh

RSC Conference, *BioNanotechnology 3*, 19-21st September 2005, The University of Sussex

NSTI Nanotech 2006, Nanotechnology Conference, *Micro & Nano Fluidics*, 8-11th May 2006, Boston, USA

The Fourth International Conference on Nanochannels, Microchannels and Minichannels, ASME, 19-21st June 2006, University of Limerick, Ireland

Microfluidics Seminar, TUV NEL, June 2006, Thistle East Midlands Airport Hotel, Derby, UK

Physical Chemistry Section Meetings, Firbush Point

Reprints of Publications

Quantitative spatial mapping of mixing in microfluidic systems, S. W. Magennis, E. M. Graham, A. C. Jones. *Angewandte Chemie International Edition*, 2005, **44**, 6512-6516